The Dissertation Committee for Daniel William Redman Certifies that this is the approved version of the following dissertation:

Electrodeposition of Metals, Chalcogenides, and Metal Chalcogenides from Ionic Liquids

Committee:

Michael Rose, Supervisor

Keith Stevenson, Co-Supervisor

Richard Crooks

Lauren Webb

Keith Johnston

Electrodeposition of Metals, Chalcogenides, and Metal Chalcogenides from Ionic Liquids

by

Daniel William Redman, B.S.

Dissertation

Presented to the Faculty of the Graduate School of

The University of Texas at Austin

in Partial Fulfillment

of the Requirements

for the Degree of

Doctor of Philosophy

The University of Texas at Austin

August 2016

Dedication

To my Family, Nancy (Mom), Jim (Dad), Amy, and Peter who with their love and support made this possible.

Acknowledgements

I would like to acknowledge my mentor Keith Stevenson for taking a chance on me and giving me this wonderful opportunity to pursue the research I wanted to pursue. Without Keith's support I likely would not be here today. I would also like to thank my current supervisor Michael Rose for graciously taking over the role of supervisor during a tumultuous time in my graduate career. I would also like the thank my defense committee for their time in evaluating my dissertation. Next I would like to thank the entire Stevenson group past and present. Special thanks go to Donny Robinson, my birthday month brethren, who introduced me to the Stevenson group, whose hard work and dedication to the science motivated me, and for making my time in lab a fun experience. I would like to thank Sankaran Murugesan for helping me get started with my project. I would also like to thank Jake Goran for helping me understand the importance of the fundamental aspects of electrochemistry, in addition to his attitude brightening up the lab atmosphere. I would like to thank Nellymar Membreno for all of her advice that she has given me over the years and our mutual love of Seinfeld. I would like to thank Kjell Schroder for his continued enthusiasm in my work. I would like to thank Tyler Mefford for all of his suggestions and insight into my work and giving me a reason to strive to be better. I would like to thank Janine Elliot for her positive attitude and enthusiasm in lab and her straight forwardness. In addition, I thank the friends in and outside the chemistry department (Caroline Robinson, Morgan Anderson, Barret Worley, Abby Campsey, Liz Gratton, Shannon Stauffer, Brian Birdsong, Michael Cammarata, Dustin Holden) because they made this experience more than just getting a degree. I would also like the thank Penny Kline and Betsy Hamblin for being invaluable resources and helping guide me through the graduate school process.

Electrodeposition of Metals, Chalcogenides, and Metal Chalcogenides from Ionic Liquids

Daniel William Redman, PhD.

The University of Texas at Austin, 2016

Supervisor: Michael Rose

Co-Supervisor: Keith Stevenson

In this work we describe the electrodeposition of metals, chalcogenides, and metal chalcogenides from ionic liquids and investigate the fundamental electrochemical processes occurring during electrodeposition. This work covers two main projects: the electrodeposition of elemental selenium and the general electrodeposition of amorphous transition metal chalcogenides. Selenium was electrodeposited from diethyl selenite in N, N – propylmethylpiperidinium bis(trifluoromethanesulfon)imide. The electrochemical processes were investigated using *in-situ* UV-VIS spectroscopy and diethyl selenite was found to proceed through a step-wise reduction from $Se^{4+} \rightarrow Se^{0} \rightarrow Se^{2-}$. A conformal film of amorphous elemental selenium was formed upon applying a potential of E = -1.0 V vs. Pt QRE. In addition a general procedure for the electrodeposition of group 6 transition metal chalcogenides was devised using the tetrachalcogenometallate as a single precursor for electrodeposition. Molybdenum sulfide and molybdenum selenide were electrodeposited from tetraphenylphosphonium tetrathiomolybdate and tetraselenomolybdate, respectively. *In-situ* UV-VIS spectroelectrochemistry revealed that these both undergo an anodic deposition of the MoE_3 (E = S, Se) and a cathodic corrosion mechanism yielding MoE_{3-x} ($0 < x < 1$). The oxidation states of the resulting films were

confirmed using XPS and found to range from 4+ to 6+. These films showed exceptional activity for the hydrogen evolution reaction. The MoS_x catalyst was coupled with an organic layer protected *p*-Si(111) substrate and was shown to exhibt high activity for the photoelectrocatalytic hydrogen evolution reaction. The deposition had to be altered due to the limitations of *p*-type silicon, this involved the addition of a proton source to induce cathodic deposition of the MoS_x catalyst. The resulting films showed onset potential of +140 mV vs. RHE, which was comparable to Pt (+200 mV vs. RHE) in the same system.

Table of Contents

List of Tables

List of Figures

List of Illustrations

Chapter 1: Introduction

1.1 ELECTRODEPOSITION

Electrodeposition began with Alessandro Volta's invention of the Voltaic pile in 1799, a galvanic cell where the anode was a piece of zinc and the cathode was either copper or silver with a copper salt in the electrolyte; the half reactions that took place were:[1]

$$Zn_{(s)} \rightarrow Zn^{2+} + 2e^{-} \quad (1)$$

$$Cu^{2+} + 2e^{-} \rightarrow Cu_{(s)} \quad (2)$$

resulting in the electrodeposition of copper at the cathode. This generated considerable interest in this process of electroforming at the time that led to what some refered to as "electrotyping mania".[1] What would be considered modern electrodeposition started in 1840 with John Wright's discovery that metal cyanides in a cyanide solution could be used to electrodeposit silver.[1] This inspired the work of G.R. Elkington, H. Elkington, and H. de Ruolz who took out patents on the electrodeposition of gold, copper, zinc, and others from a cyanide bath.[1] This work and countless others were responsible for taking electrodeposition from an art form to a scientific process.

Electrodeposition is an inner-sphere electron process that involves (*i*) the adsorption of the metal ion to the electrode surface and (*ii*) the transfer of electrons to reduce the metal ion (although there are examples of oxidative deposition). A typical electrodeposition reaction occurs as follows:

$$M^{z+} + M_{electrode} \rightarrow M^{z+} - M_{electrode} \quad (3)$$

$$M^{z+} + ze^{-} \rightarrow M_{lattice} \quad (4)$$

where M^{z+} is the metal ion with charge z and $M_{electrode}$ is the electrode surface. This process is therefore controlled by the diffusion of metal ions to the surface of the

electrode, the identity of the electrode, the electrode-electrolyte interface, the charge transfer kinetics, and the electrodeposition mechanism. The diffusion of metal ions to the surface of the electrode is dependent on the size of the metal ions and the viscosity of the electrolyte. The role of the electrode material is an important as favorable interactions between the metal ions and the electrode can lead to deposition prior to the Nernst potential, known as underpotential deposition.[2] Unfavorable reactions between the metal ion and the electrode can lead to an overpotential or a lack of deposition altogether. The electrode-electrolyte interface is influenced heavily by the electronic structure of the electrode and the chemical structure of the electrolyte at this interface. Additives exemplify this greatly, as an example Damjanovic et al. observed for the growth of copper on Cu(100) that for surface concentrations of n-decylamine $< 10^{-2}$ the crystal grew as layers. When the surface concentration of n-decylamine $> 10^{-2}$ the crystal grew as ridges.[3] The kinetics of charge transfer is dependent on the electronic structure of the electrode, the electronic structure of the metal ion, the applied potential, and the thermal energy available. The mechanism of electrodeposition is dependent on all of these factors. Understanding how each of these contributes to the electrodeposition process is essential to further development of the electrodeposition process.

Deposition of films and coatings is a heavily researched area and many methods have been developed, so one may ask “why choose electrodeposition over other methods?” The first is the efficient use of reactants in the electrodeposition bath. The quantity of charge passed is directly proportional to the amount of material deposited. While in other techniques like chemical vapor deposition and physical deposition only a small amount of the material ends up deposited on the actual substrate and often the apparatus is coated in the unused material. These techniques also require high temperatures (large energy inputs) compared to electrodeposition, which is usually done

below 100 °C in aqueous deposition and below 200 °C in ionic liquid deposition. Another advantage of electrodeposition is the ability to control both temperature and the potential of the reaction, which allows for a deeper level of control. Lastly, this technique is inherently scalable as many of the other techniques struggle with producing large area deposits. These reasons are why electrodeposition has found use in the electrodeposition of copper for integrated circuits (Damascene process),[4] electrodeposition for magnetic recording devices,[5] and electrodeposition of multilayer structures for sensors and nanometer-scale electronic circuitry.[6]

Traditionally, electrodeposition has taken place in aqueous electrolyte solutions. These solutions offer versatility in that they can control the pH and therefore the chemistry of metal ions in solution. One of the major limitations of aqueous electrolytes is the limited electrochemical window (~ 2V). Alternatives, such as organic electrolytes, molten salts, and ionic liquids have arisen as promising alternatives to traditional aqueous electrolytes. Organic solvents have been shown to be effective for the deposition many metals and compounds. For instance, an amorphous Lu–Co alloy was electrodeposited from dimethyl sulfoxide (DMSO) using LiCl, $LuCl_3$, and $CoCl_3$ at room temperature.[7] Crystalline ZnTe was prepared from propylene carbonate using $TeCl_4$, $ZnCl_2$, and $NaClO_4$ at 150 °C.[8] Issues arise when considering the toxicity and volatility of some of these solvents, as well as, safety concerns regarding the flammability of the solvents. Molten salts have also been shown to be effective electrolyte systems for the deposition of a variety of metals. As an example, molybdenum metal was electrodeposited from a $ZnCl_2$–NaCl–KCl melt using $MoCl_3$ at 250 °C.[9] Aluminum was electrodeposited from $AlCl_3$–NaCl–KCl melt at 140 °C.[10] Both examples of metals that cannot be electrodeposited from aqueous electrolytes. Molten salts are corrosive and in the case of $AlCl_3$–NaCl–KCl not stable outside of an inert atmosphere. Ionic liquids have generated

interest as they mitigate many of the problems faced by organic and molten salt electrolytes.

1.2 IONIC LIQUIDS

Ionic liquids are compounds composed solely of organic cations and anions with a melting point below 100 °C. They are commonly composed of a nitrogen or phosphorus containing cation and a fluorinated anion. They have gained significant interest as green solvents due to their low volatility and inflammability.[11,12] Ionic liquids are also gaining traction in the electrochemical community due to their large electrochemical windows and high electronic conductivity.[13–15] One particular area of interest in the electrochemical community is on the electrodeposition of metals and metalloids from ionic liquids.[16] Researchers have been able to deposit unique and interesting materials such as Al,[17,18] Ta,[19,20] Si,[21,22] Ge,[23,24], GeS_x,[25] MoS_x,[26] CdTe,[27] and many others. Understanding the synthetic procedures and physical and chemical properties of ionic liquids is essential to their utility as electrodeposition electrolytes.

The synthesis of ionic liquids is a relatively straightforward process and three methods have emerged to reliably synthesize all ionic liquids, the salt metathesis reaction, the acid-base reaction, the silver precipitation reaction, and the alkylation reaction. The salt metathesis reaction involves the exchange of cations and anions from the ionic liquids precursors as follows:[28]

$$[Cation][Br] + [Li][Anion] \rightarrow [Cation][Anion] + LiBr \quad (5)$$

where $[Cation]$ and $[Anion]$ are the cation and anion of the ionic liquid. This reaction is commonly used to synthesize hydrophobic ionic liquids as the ionic liquid is generally insoluble in water. The silver precipitation reaction involves the reaction of bromide cation salt reacting with the silver anion salt in water:[28]

$$[Cation][Br] + [Ag][Anion] \rightarrow [Cation][Anion] + AgBr \downarrow \qquad (6)$$

silver bromide precipitates readily from water making the separation simple. This synthesis is commonly used to prepare hydrophilic ionic liquids. The alkylation reaction involves the reaction between the alkylated anion and cation precursor, e.g.:[29]

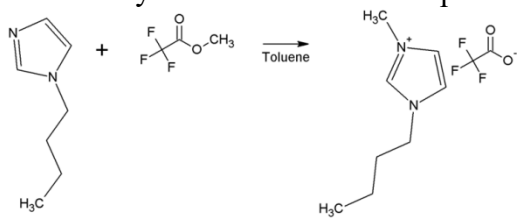

(7)

This synthesis is very useful in preparing hydrophilic ionic liquids.

The physical properties of ionic liquids that govern there applicability as electrodeposition electrolytes are the electrochemical window, conductivity, and viscosity. All of these properties are dictated by the identity of the cation and anion. Electrochemical windows of ionic liquids can range from ~3.0 V all the way to ~7 V for [EMIM][$N(CN)_2$] and [PP_{13}][PF_6], respectively , but usually fall in the area of 4 – 5 V.[15,30,31] At extreme potentials the cation or anion can undergo reduction or oxidation, respectively, similar to how water will evolve hydrogen at highly reducing potentials and evolve oxygen at highly oxidizing potentials. Ionic liquids contain high concentrations of charge carriers and when these charge carriers are highly mobile high conductivities can be observed. Typically, conductivities range from 0.1 – 20 mS cm^{-1}.[14,29,32] These values are low when compared to concentrated aqueous solutions, e.g. 29.4 wt% KOH used in alkaline batteries, which has a conductivity of 540 mS cm^{-1}.[15] Part of the reason for the relatively lower conductivities observed in ionic liquids is the viscosity, which is inversely proportional to the conductivity. The viscosity of ionic liquids is one of the major drawbacks of practical implementation in electrochemical systems. Higher viscosity leads to slower diffusion rates, which contributes to concentration polarization

at the electrode surface. Viscosity has been found to be highly determined on the nature of the anion. [29,33–36] Many factors contribute to the viscosity including size, shape, and molar mass of the anion as well as its ability to form hydrogen bonds or van der Waals attractions.[15] Cations can also influence the viscosity due to stronger van der Waals interactions between larger cations.[29,37,38] Typical viscosities range from ~30 – 300 cP.[39] Understanding how cations and anions affect each of these characteristics allow the choice of the one best suited for the intended purposes.

1.3 Chalcogenides and Metal chalcogenides

Chalcogenides (S, Se, Te) and transition metal chalcogenides are an interesting class of materials due to their unique physical, chemical, and electronic properties. They have found use in diverse fields such as X-ray imaging, photovoltaics, non-voltatile memory devices, electrocatalysis, energy storage, and microelectronics.[40–43] Understanding more about the properties of these materials gives insight into why they should be studied.

Selenium has several allotropes that can interconvert with temperature changes; these allotropes all have unique properties. Monoclinic selenium is a crystalline form of selenium that is red in color and consists of puckered Se_8 rings, similar to what is observed in sulfur.[44] Like sulfur this material is insulating in nature.[45] Trigonal selenium is a crystalline form of selenium that is grey in color and consisting of helical polymeric chains.[44] This material is electronically conductive as well as photoconductive, i.e. electrical conductivity increases with increased illumination.[45] Amorphous selenium is also red and thought to be composed of a disordered array of Se_8 rings and helical polymeric chains.[45] This materials is known to be photoconductive as well as photovoltaic, i.e. it becomes an electrical conductor when exposed to light.[45,46]

Transition metal chalcogenides, and more specifically molybdenum chalcogenides interesting due to their structural and chemical properties. Crystalline MoS_2 and $MoSe_2$ form a graphite-like layered structure composed of a hexagonally packed layer of molybdenum atoms sandwiched two layers of chalcogens between that is held together by van der Waals interactions.[42] There are three common polytypes 1T, 2H, and 3R, where the number refers to the number of layers in the unit cell and the letter refers to trigonal, hexagonal, and rhombohedral, respectively.[42] 1T MoS_2 is known to exhibit metallic conductivity while 2H MoS_2 exhibits semiconducting properties.[42] The edges of the MoE_2 (E = S, Se) have shown to be sites of high activity.[43,47,48] These active edge sites are thought to be the reason behind MoS_2 and $MoSe_2$ high activity for reactions like the hydrogen evolution reaction. In addition to the crystalline forms molybdenum sulfide and molybdenum selenide can exist in an amorphous state of MoE_3. There is considerable debate about the structure, with some believing that amorphous molybdenum sulfide exist as a disordered array of trigonal chain structures others believe they exist as molybdenum-sulfur cluster compounds.[49–51] Amorphous molybdenum sulfide (and selenide) contain two types of sulfur ion, S^{2-} and S_2^{2-} (Se^{2-} and Se_2^{2-}).[50] These materials also exhibit high activity for the hydrogen evolution reaction, although the reason for this activity is not well understood.

1.4 OBJECTIVES

The primary objective of this work is to develop methods for the electrodeposition of chalcogenides and metal chalcogenides from ionic liquids using single-site precursors. This began with the identification of diethyl selenite as a suitable precursor for the electrodeposition of selenium from 1-propyl-1-methylpiperidinium bis(trifluoromethanesulfonyl)imide (PP_{13}–TFSI). In addition $[MoS_4]^{2-}$ and $[MoSe_4]^{2-}$

were investigated for the electrodeposition from 1-ethyl-1-methylimidazolium bis(trifluoromethanesulfonyl)imide (EMIM-TFSI) of MoS_x and $MoSe_x$ films. The electrochemistry and mechanism of deposition were investigated using *in-situ* UV-Vis spectroelectrochemical techniques. These films were characterized using a variety of techniques X-ray diffraction, Raman spectroscopy, X-ray photoelectron spectroscopy, scanning electron microscopy, and electrochemical techniques. In the case of the MoS_x and $MoSe_x$ the films were tested for their hydrogen evolution reaction activity.

The secondary objective of this work was to combine the more active MoS_x catalyst with an organic-modified *p*-Si(111) photocathode and to test its reactivity for the photoelectrochemical hydrogen evolution reaction. This required a further investigation into the electrodeposition method using a proton source to catalyze the deposition onto the *p*-Si(111)|Org substrates. The organic-modified *p*-Si(111) substrates were characterized by XPS, water contact angle measurements, and electrochemical impedance spectroscopy. The MoS_x films deposited on the organic-modified *p*-Si(111) surfaces were characterized by AFM, XPS, Raman spectroscopy, and scanning electron microscopy. Linear sweep voltammetry under exposure to light was used to evaluate the electrocatalytic acitivity for the hydrogen evolution reaction. The *p*-Si(111)|diOMe|MoS_x showed high activity for the hydrogen evolution reaction.

1.5 OUTLINE

Chapter 2 discusses the electrodeposition of selenium from diethyl selenite from PP_{13}-TFSI. The mechanism of deposition as elucidated by UV-Vis spectroelectrochemistry is discussed as well as the characterization of the thin film. Chapter 3 discusses the general electrodeposition method of MoS_x and $MoSe_x$ from EMIM-TFSI. The mechanism of deposition as investigated by UV-Vis

spectroelectrochemistry was discussed. The activity of MoS_x and $MoSe_x$ for the hydrogen evolution reaction in acidic conditions is discussed. Chapter 4 discusses the photo-assisted electrodeposition of MoS_x on organic-modified *p*-Si(111) and showcases its high activity for the hydrogen evolution reaction.

1.6 REFERENCES

(1) Brenner, A. *Electrodeposition of Alloys: PRINCIPLES and PRACTICE*; Academic Press, 1963.

(2) Bard, A. J.; Faulkner, L. R.; Leddy, J.; Zoski, C. G. *Electrochemical methods: fundamentals and applications*; Wiley New York, 1980; Vol. 2.

(3) Damjanovic, A.; Paunovic, M.; Bockris, J. O. *J. Electroanal. Chem.* **1965**, *9*, 93–111.

(4) Hu, C.-K.; Harper, J. M. E. *Mater. Chem. Phys.* **1998**, *52*, 5–16.

(5) Anderson, P,C.; Romankiw, L.T. *Advances in Electrochemical Science and Engineering*, VCH New York, **1994**, Vol. 3.

(6) Schwarzacher, W.; Lashmore, D. S. *IEEE Trans. Magn.* **1996**, *32*, 3133–3153.

(7) Li, G.; Tong, Y.; Liu, G. *J. Electroanal. Chem.* **2004**, *562*, 223–229.

(8) Heo, P.; Ichino, R.; Okido, M. *Electrochimica Acta* **2006**, *51*, 6325–6330.

(9) Nakajima, H.; Nohira, T.; Hagiwara, R. *Electrochimica Acta* **2006**, *51*, 3776–3780.

(10) Jafarian, M.; Mahjani, M. G.; Gobal, F.; Danaee, I. *J Appl Electrochem.* **2006**, *36*, 1169–1173.

(11) Thomas, P. A.; Marvey, B. B. *Molecules* **2016**, *21*, 184.

(12) Bubalo, M. C.; Vidović, S.; Redovniković, I. R.; Jokić, S. *J. Chem. Technol. Biotechnol.* **2015**, *90*, 1631–1639.

(13) Abo-Hamad, A.; AlSaadi, M. A.; Hayyan, M.; Juneidi, I.; Hashim, M. A. *Electrochimica Acta* **2016**, *193*, 321–343.

(14) Gali´nski, M.; Lewandowski, A.; St\kepniak, I. *Electrochimica Acta* **2006**, *51*, 5567–5580.

(15) Hapiot, P.; Lagrost, C. *Chem. Rev.* **2008**, *108*, 2238–2264.

(16) Endres, F.; MacFarlane, D.; Abbott, A. *Electrodeposition from ionic liquids*; John Wiley & Sons, 2008.

(17) Abedin, S. Z. E.; Moustafa, E. M.; Hempelmann, R.; Natter, H.; Endres, F. *ChemPhysChem* **2006**, *7*, 1535–1543.

(18) Bakkar, A.; Neubert, V. *Electrochimica Acta* **2013**, *103*, 211–218.

(19) Ispas, A.; Adolphi, B.; Bund, A.; Endres, F. *Phys. Chem. Chem. Phys.* **2010**, *12*, 1793.

(20) Borisenko, N.; Ispas, A.; Zschippang, E.; Liu, Q.; Abedin, S. Z. E.; Bund, A.; Endres, F. *Electrochimica Acta* **2009**, *54*, 1519–1528.

(21) Pulletikurthi, G.; Lahiri, A.; Carstens, T.; Borisenko, N.; Abedin, S. Z. E.; Endres, F. *J Solid State Electrochem.* **2013**, *17*, 2823–2832.

(22) Komadina, J.; Akiyoshi, T.; Ishibashi, Y.; Fukunaka, Y.; Homma, T. *Electrochimica Acta* **2013**, *100*, 236–241.

(23) Endres, F. *Phys. Chem. Chem. Phys.* **2001**, *3*, 3165–3174.

(24) Wu, M.; Vanhoutte, G.; Brooks, N. R.; Binnemans, K.; Fransaer, J. *Phys. Chem. Chem. Phys.* **2015**, *17*, 12080–12089.

(25) Murugesan, S.; Kearns, P.; Stevenson, K. J. *Langmuir* **2012**, *28*, 5513–5517.

(26) Murugesan, S.; Akkineni, A.; Chou, B. P.; Glaz, M. S.; Vanden Bout, D. A.; Stevenson, K. J. *ACS nano* **2013**, *7*, 8199–8205.

(27) Hsiu, S.-I.; Sun, I.-W. *J. Appl. Electrochem.* **2004**, *34*, 1057–1063.

(28) Wilkes, J. S.; Zaworotko, M. J. *J. Chem. Soc. Chem. Commun.* **1992**, 965.

(29) Bonhôte, P.; Dias, A.-P.; Papageorgiou, N.; Kalyanasundaram, K.; Grätzel, M. *Inorg. Chem.* **1996**, *35*, 1168–1178.

(30) Barisci, J. *Electrochem. Commun.* **2004**, *6*, 22–27.

(31) Murugesan, S.; Quintero, O. A.; Chou, B. P.; Xiao, P.; Park, K.; Hall, J. W.; Jones, R. A.; Henkelman, G.; Goodenough, J. B.; Stevenson, K. J. *J. Mater. Chem.* **2014**, *2*, 2194–2201.

(32) McFarlane, D. R.; Sun, J.; Golding, J.; Meakin, P.; Forsyth, M. *Electrochimica Acta* **2000**, *45*, 1271–1278.

(33) Fitchett, B. D.; Knepp, T. N.; Conboy, J. C. *J. Electrochem. Soc.* **2004**, *151*, 219.

(34) Jiqin, Z.; Jian, C.; Chengyue, L.; Weiyang, F. *J. Chem. & Eng. Data* **2007**, *52*, 812–816.

(35) Tokuda, H.; Hayamizu, K.; Ishii, K.; Susan, M. A. B. H.; Watanabe, M. *J. Phys. Chem. B* **2004**, *108*, 16593–16600.

(36) Ong, S. P.; Andreussi, O.; Wu, Y.; Marzari, N.; Ceder, G. *Chem. Mater.* **2011**, *23*, 2979–2986.

(37) Tokuda, H.; Hayamizu, K.; Ishii, K.; Susan, M. A. B. H.; Watanabe, M. *J. Phys. Chem. B* **2005**, *109*, 6103–6110.

(38) Huddleston, J. G.; Visser, A. E.; Reichert, W. M.; Willauer, H. D.; Broker, G. A.; Rogers, R. D. *Green Chem.* **2001**, *3*, 156–164.

(39) Zhang, S.; Sun, N.; He, X.; Lu, X.; Zhang, X. *J. Phys. Chem. Ref. Data* **2006**, *35*, 1475.

(40) Kasap, S.; Frey, J. B.; Belev, G.; Tousignant, O.; Mani, H.; Laperriere, L.; Reznik, A.; Rowlands, J. A. *Phys. Status solidi* **2009**, *246*, 1794–1805.

(41) Tanaka, K.; Shimakawa, K. *Amorphous chalcogenide semiconductors and related materials*; Springer Science & Business Media, 2011.

(42) Chhowalla, M.; Shin, H. S.; Eda, G.; Li, L.-J.; Loh, K. P.; Zhang, H. *Nat. Chem.* **2013**, *5*, 263–275.

(43) Jaramillo, T. F.; Jorgensen, K. P.; Bonde, J.; Nielsen, J. H.; Horch, S.; Chorkendorff, I. *Science* **2007**, *317*, 100–102.

(44) Cooper, W. C.; Zingaro, R. A. *Selenium*; Van Nostrand Reinhold, 1974.

(45) Mooradian, A.; Wright, G. B.; Cooper, W. C. *Pergamon Press. Oxf.* **1969**.

(46) Gilleo, M. A. *J. Chem. Phys.* **1951**, *19*, 1291.

(47) Wang, H.; Zhang, Q.; Yao, H.; Liang, Z.; Lee, H.-W.; Hsu, P.-C.; Zheng, G.; Cui, Y. *Nano Lett.* **2014**, *14*, 7138–7144.

(48) Tsai, C.; Chan, K.; Abild-Pedersen, F.; Nørskov, J. K. *Phys. Chem. Chem. Phys.* **2014**, *16*, 13156.

(49) Hibble, S. J.; Wood, G. B. *J. Am. Chem. Soc.* **2004**, *126*, 959–965.

(50) Weber, T.; Muijsers, J. C.; Niemantsverdriet, J. W. *J. Phys. Chem.* **1995**, *99*, 9194–9200.

(51) Liang, K. S.; Cramer, S. P.; Johnston, D. C.; Chang, C. H.; Jacobson, A. J.; Chianelli, R. R. *J. Non-Crystalline Solids* **1980**, *42*, 345–356.

Chapter 2: Cathodic Electrodeposition of Amorphous Elemental Selenium from an Air- and Water-Stable [1]

The electronic, optoelectronic, and chemical properties of thin films of selenium and selenium-containing compounds have led to a variety of applications, e.g. X-ray imaging, photovoltaics, non-volatile memory devices, and electrocatalysts.[1–3] Thin films of selenium and selenium compounds are commonly produced using a variety of methods including vacuum deposition techniques, chemical bath deposition, and chemical vapor deposition.[4–8] Electrodeposition is an alternative deposition technique that provides advantages over other techniques, including lower cost of production. Efforts have been made to electrodeposit amorphous and metallic Se in aqueous conditions, but they often require extreme pH conditions and can lead to the formation of other products, such as H_2Se.[9–13]

In the past decade ionic liquids have gained attention as an alternative electrolyte media for the electrodeposition of various semiconductors and reactive metals, such as Ge, Si, Ta, and Al, due to their large electrochemical windows and low volatility.[14] Several groups have developed methods to deposit both amorphous and metallic selenium using several ionic liquids and Se precursors.[15–19] In 1-butyl-1-methylpyrrolidinium bis(trifluoromethylsulfonyl)imide at temperatures >100 °C a trigonal Se (t-Se) deposit was obtained from $SeCl_4$.[15] Deposition using $SeCl_4$ or SeO_2 in 1-ethyl-3-methylimdazolium tetrafluoroborate/chloride at temperatures >100 °C produced single crystal nanowires of t-Se from SeO_2 and an amorphous selenium (a-Se) deposit from $SeCl_4$.[17] Recently, selenium has been deposited from H_2SeO_3 in 1-butyl-1-

[1]Large parts of this chapter have been published as D.W. Redman, S. Murugesan, K.J. Stevenson. *Langmuir* **2013**, *30*, 418. Reprinted with permissions from the American Chemical Society (ACS).

methylpyrrolidinium trifluoromethylsulfonate and 1-ethyl-3-methylimdazolium trifluoromethylsulfonate with H_2O as a co-solvent (5 vol %) in open air conditions at various temperatures. The morphology and phase of these deposits were found to differ for nearly identical electrodeposition conditions.[18,19] Clearly, the morphology, phase, and crystallinity of Se electrodeposited from ionic liquids are dependent on the choice of selenium precursor, ionic liquid, and temperature. A deeper understanding of the deposition mechanism is essential to controlling the properties of electrodeposited films.

Coupling spectroscopic techniques with electrochemistry has been particularly useful in the study of intermediates of electrochemical reactions, formation of inorganic complexes, and charge states of conducting polymers.[20,21] Lahiri et al. recently used *in-situ* UV-Vis spectroelectrochemistry to study the electrodeposition of Ge, Si, and Si_xGe_{1-x} from ionic liquids. For the electrodeposition of Si_xGe_{1-x} they found evidence to support the codeposition of Ge and Si nanoparticles, which lead to the inclusion of Si into the Ge matrix.[22] Selenium is an interesting species because it has several allotropes that absorb light strongly in the ultraviolet and visible region making it possible to study the electrodeposition processes with *in-situ* UV-Vis spectroelectrochemistry.[23,24]

In this work, we present a method for preparing amorphous selenium films at room temperature from the air- and water-stable ionic liquid 1-propyl-1-methylpiperidinium bis(trifluoromethylsulfonyl)imide ($[PP_{13}][TFSI]$) using diethyl selenite ($(CH_3CH_2O)_2Se=O$). Cyclic voltabsorptometry and *in-situ* UV-Vis spectroelectrochemistry were employed to investigate the electrochemistry of diethyl selenite and the electrodeposition mechanism. Electrochemical experiments were carried out on fluorine-doped tin oxide (FTO) electrodes in an ionic liquid containing acetonitrile in open air conditions. Addition of acetonitrile as a co-solvent plays an important role in

forming strongly adherent films as well as increasing the solubility of diethyl selenite in the ionic liquid.

CHAPTER 2.2 EXPERIMENTAL

Diethyl selenite was synthesized using a published procedure.[25] Briefly, diethyl selenite was prepared by dissolving selenous acid (Strem, 99.999 % - Se) in excess ethanol (5:1) and stirring at 80 °C for 4 hours. Water was azeotropically distilled with ethanol and benzene using a Dean-Stark apparatus. The product was purified by distillation at 80 °C under reduced pressure, resulting in a colorless liquid, which was stored in a dessicator. Chemical ionization mass spectrometry revealed several peaks, the most intense was m/z = 187 corresponding to $(CH_3CH_2O)_2Se{=}OH^+$. Other peaks observed in order of decreasing intensity were m/z = 113 (SeO_2H^+), 141 ($(CH_3CH_2O)Se{=}OH^+$), and 159 ($(CH_3CH_2O)Se\text{-}O_2H^+$). $[PP_{13}][TFSI]$ (IoLiTec, 99 %) was used as the electrolyte. Before use $[PP_{13}][TFSI]$ was dried in a vacuum oven at 90 °C for 24 hours. Acetonitrile (CH_3CN, Fisher, >99.5 %) was used as supplied. The solubility of diethyl selenite in $[PP_{13}][TFSI]$ is moderate and was found to improve with the addition 1 – 6 mol eq. (0.6 – 3 vol %) of CH_3CN. We found that 6 mol eq. of CH_3CN produced the best results. Upon addition of CH_3CN to the electrolyte the solution was sonicated briefly.

2.2.1 Electrochemical and Spectrolectrochemical Measurements

The cyclic voltammetry and electrodeposition experiments were carried out in a standard three electrode cell under open air conditions at room temperature. Transparent fluorine-doped tin oxide (FTO, Pilkington) deposited on glass was used as the working electrode. FTO was cleaned by subsequent sonicating with acetone, ethanol, isopropanol, 30 vol% aqueous ethanolamine at 80 °C for 10 minutes, and nanopure water (18 MΩ-cm)

for 1 hour. The FTO electrodes were dried under N_2 followed by heating in an oven at ~100 °C for 24 hours. Pt wire was used as the counter electrode and as the quasi-reference electrode (QRE). The counter electrode and QRE were immersed directly into the solution. Pt wire was chosen as the QRE because it does not readily react with Se. A drawback to using Pt is that it can undergo shifts in potential up to 200 mV. All electrochemical experiments were performed on a CH440 Potentiostat/Galvanostat (CH Instruments). Spectroelectrochemistry experiments were carried out on a diode array UV-Vis spectrometer (Agilent 8453) and a homemade Teflon spectroelectrochemical cell with a path length of 1 cm. Absorbance spectra were collected for wavelengths between 190 – 1100 nm. UV-Vis measurements were made in five second intervals for the cyclic voltabsorptometry experiments and in one minute intervals for the *in-situ* measurements of the electrodeposition. After electrodeposition experiments the working electrode was washed with ethanol and acetone, dried under N_2, and vacuum dried at room temperature for at least 1 hr.

2.2.2 Thin Film Characterization

The electrodeposited Se films were analyzed using several techniques. The surface morphology of the deposits was investigated with a high resolution field emission scanning electron microscope. Scanning electron microscopy (SEM) was carried out on a FEI Quanta 650 FEG ESEM operating at 15 kV. Energy dispersive X-ray spectroscopy was used to analyze the elemental composition of the films.

The crystallinity and phase of the films were analyzed using glancing angle X-ray diffraction. A Bruker AXS D8 Advance X-ray diffractometer using a Cu-Kα source was used. The incident angle of the radiation was 0.5°. The measurements were carried out at

40 kV and 40 mV for 3 hours with a rotation rate of 6° per minute. The data was obtained between 10-60° 2θ and processed using the EVA Software.

The phase of the deposited films was further analyzed using Raman spectroscopy. Raman analysis was performed on a Renishaw inVia microscope utilizing 514.5 nm Ar laser in the backscattering configuration. A 50x aperture was used to focus the beam resulting in a beam spot of approximately 2 μm in diameter. The instrument was calibrated using the Stokes Raman signal at 521 cm^{-1} of a bulk Si single crystal with the [110] direction oriented normal to the laser. The spot size was calculated to have a diameter of 1.3 μm. The laser was operated at a low power (5%, <0.5 mW) for short times (5s) to prevent photocrystallization of the selenium films.

Analysis of the Raman spectra was performed in OriginPro 8 software (version 8.0724, OriginLab Corporation). A linear background subtraction was used to remove a rising baseline from the spectra. All peaks were fit with Gaussian profiles.

X-Ray Photoelectron Spectroscopy (XPS) was used to investigate the chemical environment and purity of the selenium films. XPS was carried on a Kratos AXIS Ultra DLD system with a monochromated Al Kα source (1,486.7 eV) positioned at 45° to the sample. Electrons were collected on a hemispherical mirror analyzer aligned normal to the sample with a resolution of 1 eV for survey scans and 0.1 eV for high resolution scans.

Semi-quantitative analysis of the XPS spectra was performed with the CasaXPS software (version 2.3.16, Casa Software Ltd.). High resolution scans were used to compare the relative concentrations of the different species comprising the film. Non-metals, F and O, were fit with linear backgrounds and Se was fit with a Shirley background. All fitted curves were the result of the summation of multiple Voigt functions with 30% Lorentzian and 70% Gaussian character.

CHAPTER 2.3 RESULTS AND DISCUSSION

2.3.1 Electrochemistry of Diethyl Selenite

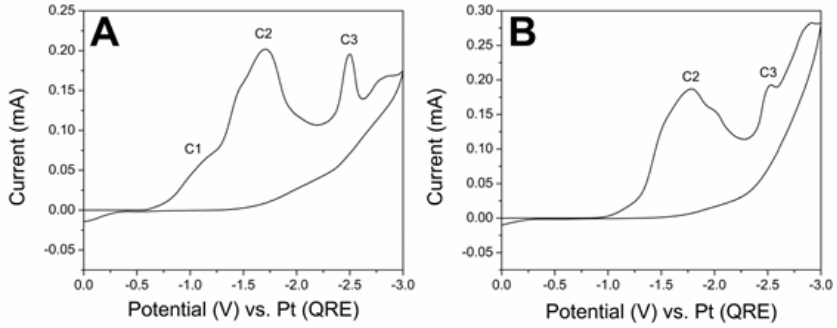

Figure 2.1: (A) Scan 1 and (B) Scan 2 of cyclic voltammogram of a FTO electrode immersed in 0.1 M $(CH_3CH_2O)_2Se{=}O$ in $[PP_{13}][TFSI]$/6 mol eq. CH_3CN. Scan rate = 10 mV/s.

Cyclic voltammetry was used to investigate the electrochemistry of $(CH_3CH_2O)_2Se{=}O$. Figure 2.1A shows the first scan of the cyclic voltammogram (CV) obtained at an FTO electrode immersed in 0.1 M $(CH_3CH_2O)_2Se{=}O$ in $[PP_{13}][TFSI]$/6 mol eq. CH_3CN at room temperature. A minor reduction peak is observed at C1. This peak disappears in the second scan, Fig. 2.1B, and all subsequent scans, which suggests that it is the reduction of a species adsorbed on the electrode at open circuit. To investigate this we immersed FTO electrodes in the electrolyte, then washed, dried, and analyzed them by XPS. No appreciable Se signal was observed. The washing procedure could remove weakly adsorbed selenium species leading to the observed results. The CV of 0.6 M CH_3CN in $[PP_{13}][TFSI]$ (Fig. S2.1A) has a feature at C1, although the integrated current (charge) is significantly smaller. This suggests some of the charge passed may be from the reduction of acetonitrile. Cyclic voltammetry of a 0.1 M $(CH_3CH_2O)_2Se{=}O$ in

[PP_{13}][TFSI]/12 mol eq. CH_3CN showed no difference in the CV (Fig. S2.1B) associated with the C1 feature. This suggests C1 may in fact be solely due to the reduction of an adsorbed selenium species. Adsorption of selenium species on various electrode materials, including SnO_2, at open circuit potential has been reported in aqueous solutions and it is reasonable to expect it to occur in ionic liquids as well.[11,26] From the CV two main reduction peaks are observed, C2 and C3. Potentiostatic deposition at C2 (-1.7 V) resulted in a red deposit on the electrode, thought to be amorphous selenium, suggesting that the peak at C2 is due to the 4-electron reduction of $(CH_3CH_2O)_2Se{=}O$ to Se^0. The peak at C3 is thought to be either the direct reduction of Se^{4+} to Se^{2-} or the reduction of deposited Se^0 to Se^{2-}. The reduction mechanism is highly dependent on the electrodeposition conditions as both reduction mechanisms have been reported in ionic liquids.[18,19,27] In the case of $(CH_3CH_2O)_2Se{=}O$ it is more likely that deposited Se^0 is being reduced to Se^{2-} since the integrated current at C3 is significantly smaller than the integrated current at C2. In the anodic scan two oxidation processes at -0.2 V and 0.2 V are observed. The absence of the oxidation process beginning at -0.2 V from the CV of FTO in [PP_{13}][TFSI] (Fig. S2.2A) and of FTO in 0.6 M CH_3CN in [PP_{13}][TFSI] suggests that this process is associated with the oxidation of adsorbed Se. The oxidation process at 0.2 V is associated with the FTO electrode as shown in Fig. S2.2A. A second minor peak appears on the second scan (Fig. 2.1B) at E = -2.0 V. Figure S2.2A shows a reduction process beginning at approx. -1.7 V, which is believed to be the reduction of SnO_2. This is a complex process that could include the formation of SnO_x electrode species, formation of oxygen or oxide ions, and the dissolution of tin. On the reverse scan a nucleation loop is observed, suggesting deposition of Sn^0 or SnO_x species on the electrode. The appearance of the peak at -2.0 V on the second scan could be due to reduction of $(CH_3CH_2O)_2Se{=}O$ on a Sn^0 or SnO_x species. Cyclic voltammetry on tin disk

electrode (Fig. S2.2B) showed the main reduction wave of $(CH_3CH_2O)_2Se{=}O$ occurred at approx. -2.1 V, which suggests that the peak at E = -2.0 V may be due to the reduction of Se^{4+} to Se^0 on Sn.

The purpose of adding acetonitrile to the deposition bath was to increase the solubility of $(CH_3CH_2O)_2Se{=}O$ in $[PP_{13}][TFSI]$, but it may have had other consequences. Diluting ionic liquids with molecular solvents can result in an increase in the diffusion coefficient caused by a decrease in the viscosity of the solution. To investigate this ferrocene was used as a redox probe. The diffusion coefficient of ferrocene in $[PP_{13}][TFSI]$ was estimated to be ~1.0×10^{-7} cm^2/s by chronoamperometry and cyclic voltammetry, which is in agreement with previously reported values.[28] For comparison, the diffusion coefficient of ferrocene in acetonitrile has been estimated to be between 2.0 – 2.6×10^{-5} cm^2/s.[29] In the presence of 0.6 M CH_3CN (3 vol %) the diffusion coefficient of ferrocene did not change significantly. In electrodeposition baths organic additives are often used for a variety of purposes, including complexation and leveling. Recently, the Miura group has shown that CH_3CN shifts the deposition potential for Ni electrodeposition to more positive values by the formation of a $[Ni(CH_3CN)_6]^{2+}$ complex.[30] It is likely that a Se – CH_3CN complex is forming, although further investigation is warranted. An increase in the concentration of CH_3CN from 0.4 to 0.6 M had little effect on the electrochemistry of diethyl selenite. It is also possible that adsorption of CH_3CN on the electrode occurs, leading to a leveling effect on the deposit.

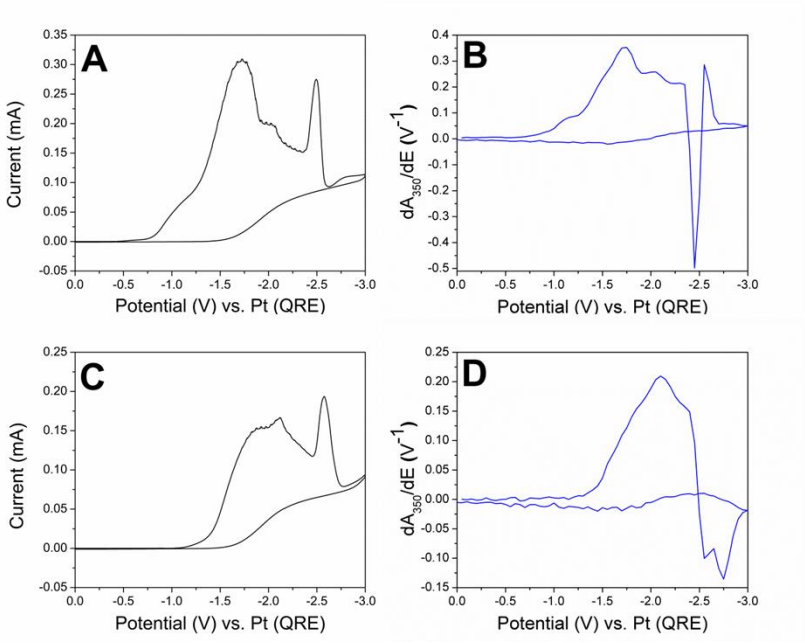

Figure 2.2: First scan of (A) cyclic voltammogram and (B) derivative cyclic voltabsorptogram for a FTO electrode immersed in 0.1 M $(CH_3CH_2O)_2Se{=}O$ in $[PP_{13}][TFSI]$/6 mol eq. CH_3CN. (C) CV and (D) DCVA of the second scan. Scan rate = 10 mV/s and λ = 350 nm.

In order to gain a deeper understanding of the electrochemistry of diethyl selenite cyclic voltammetry was coupled with *in-situ* UV-Vis spectroscopy. Derivative cyclic voltabsorptometry was used to monitor the change in absorbance at a particular wavelength with potential (dA_λ/dE), which is proportional to the current of the absorbing species.[31] Figure 2.2A and B shows the first scan of a CV of a FTO electrode immersed in 0.1 M $(CH_3CH_2O)_2Se{=}O$ in $[PP_{13}][TFSI]$/6 mol eq. CH_3CN and the corresponding derivative cyclic voltabsorptogram (DCVA) for λ=350 nm, respectively. This wavelength was chosen because it corresponds to strong absorption of an amorphous selenium film (Fig. A2.3).[24] In the DCVA we see the presence of peaks at C1 and C2 that are proportional to the CV, which confirms that these peaks are due to the reduction of

adsorbed Se and the bulk deposition of Se^0, respectively. The minor peak at E = -2.0 V is prominent in the first scan of the CV under periodic illumination. Visible light is known to enhance the electrodeposition of amorphous selenium and is most likely why the peak at -2.0 V is observed in the first scan.[10] From the DCVA it is clear that elemental Se^0 is being deposited at this potential. Furthermore, a photoreduction current appears in the CV when the cell is exposed to the light from the spectrometer (Fig. S2.4). Selenium is known to be a p-type photoconductor, which by definition produces a reducing photocurrent, while FTO is an n-type semiconductor that produces oxidizing photocurrent.[1,32] This provides further evidence that Se^0 is being deposited on the electrode and suggests that the electrodeposition is influenced by incident light during reduction of diethyl selenite.

Interpretation of the peak at C3 is not as straightforward as the other peaks. At C3 dA_{350}/dE decreases rapidly at the onset of the peak and then becomes negative, which indicates a decrease in the concentration of the Se^0 species being deposited followed by sequential reduction of Se^0 to form Se^{2-}. Similar behavior has been reported previously by our group for mixed molybdenum-selenium oxides.[33] Integrating the charge under the curve of the CV and using the Laviron equation the number of electrons transferred was determined to be 1.78 for both the first and second scans, which further supports that this is the two-electron reduction of adsorbed Se^0.[32] The sharp decrease followed by sharp increase in dA_{350}/dE at C3 in Fig. 2.2B has a physical reason that is explained further in the supplementary information with Fig. A2.5.

Monitoring the DCVA at longer wavelengths provides additional insight into the reduction of the diethyl selenite precursor. A plot of the first scan of the DCVA at λ=550 nm (Fig. S2.6B) shows a large increase in dA_{550}/dE associated with the C3 peak. Initially, we speculated that this could be due to formation of a SnSe or $SnSe_2$ from a reaction

between reduced Sn on the FTO electrode and Se^{2-} formed at the surface. Yet X-ray photoelectron spectroscopy (XPS) found no traces of either tin selenide species for potentiostatic deposition at -2.5 V, the C3 peak potential, although they may be below the instrumental limit of detection. The large change in absorbance with potential is not observed during the second scan (Fig. S2.6D). Rather, the absorbance actually drops by a factor of 10 and becomes negative near the peak maxima, suggesting that this spectroscopic feature is due to a change in the morphology of the adsorbed Se^0 during the first scan, which will be further discussed below. Upon reversal of potential during the second scan in the DCVA the change in absorbance with potential increases reaching a maximum at C3, likely due to a comproportionation reaction between Se^{2-} and $(CH_3CH_2O)_2Se{=}O$ to form Se^0, analogous to what is observed in aqueous media for H_2SeO_3.[11]

2.3.2 Electrodeposition Process

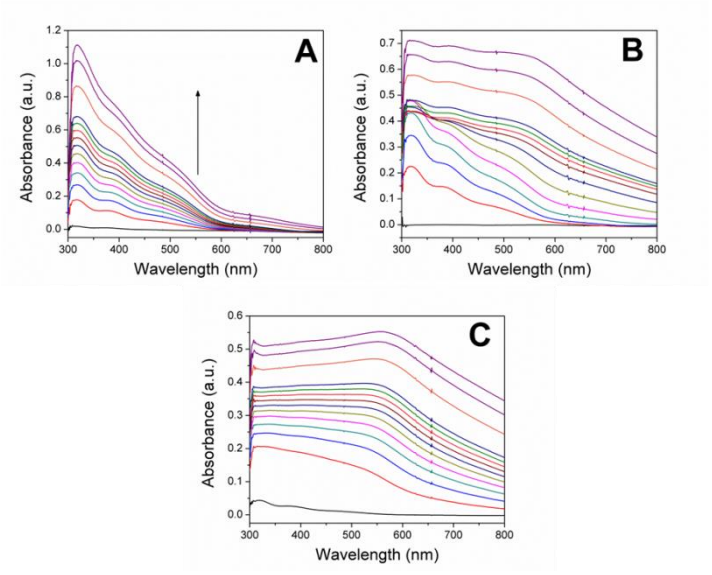

Figure 2.3: UV-Vis spectra recorded for potentiostatic deposition at (A) -1.7 V, (B) -2.0 V, and (C) -2.5 V for 30 minutes. Electrolyte solution: 0.1 M $(CH_3CH_2O)_2Se{=}O$ in $[PP_{13}][TFSI]$/6 mol eq. CH_3CN. Spectra are shown for every minute from 0-10 minutes and for every five minutes from 10-25 minutes. All spectra increase in absorbance with time as the arrow in (A) shows.

Figure 2.3A shows the *in-situ* UV-Vis spectra obtained at a FTO electrode immersed in 0.1 M $(CH_3CH_2O)_2Se{=}O$ in $[PP_{13}][TFSI]$/6 mol eq. CH_3CN held at -1.7 V (peak potential of C2 from Fig. 2.1) as a function of time. A broad absorption feature, characteristic of an amorphous selenium film, grows in over the course of the deposition.[24] In addition, the spectra appears to be composed of convoluted absorption bands with maxima at approx. 315, 375, and 500 nm, which indicate the presence of selenium nanoparticles smaller than ~150 nm in diameter.[34,35] No significant change in the absorbance of the deposit was observed after it was washed and dried (Fig S2.3.), indicating that adsorption spectrum is due to selenium deposited on the electrode. Over time the absorption bands undergo a small red shift in the absorption maxima. The red shift is likely due to increased particle size and the possible agglomeration of the Se particles.[34] Growth of selenium particles is quite rapid for the first 20 minutes, but slows down significantly as the film becomes more insulating.

Scanning electron microscopy (SEM) was employed to investigate the morphology of the deposits. Figure 2.4A, B, and C show representative SEM images for potentiostatic deposition at the C2 peak potential for 10, 30, and 120 minutes, respectively. After 10 min deposition, the coalescence of the particles is observed, although individual particles are still present. With longer deposition times the Se particles continue to coalesce creating a more uniform film, as can be seen in 4B and C,

which supports the conclusions drawn from the UV-Vis measurements. This data along with the *in-situ* UV-Vis results suggests the mechanism of film growth at -1.7 V is occurring by the nucleation of particles on the electrode surface followed by coalescence. The same morphology and phase were observed for depositions done at potentials more positive than -1.7 V, which suggests deposition mechanism is the same. After 120 minutes voids in the film appear. This is most likely due to the reduction of SnO_2, which as mentioned earlier can lead to several processes, such as release of oxygen or oxide ions from the FTO films, as evidenced by the significant decrease in the oxygen to tin ratio in the energy dispersive X-ray (EDX) spectrum. EDX also indicated the presence of residual carbon in the films, which could be from the adsorption of CH_3CN on the selenium deposits.

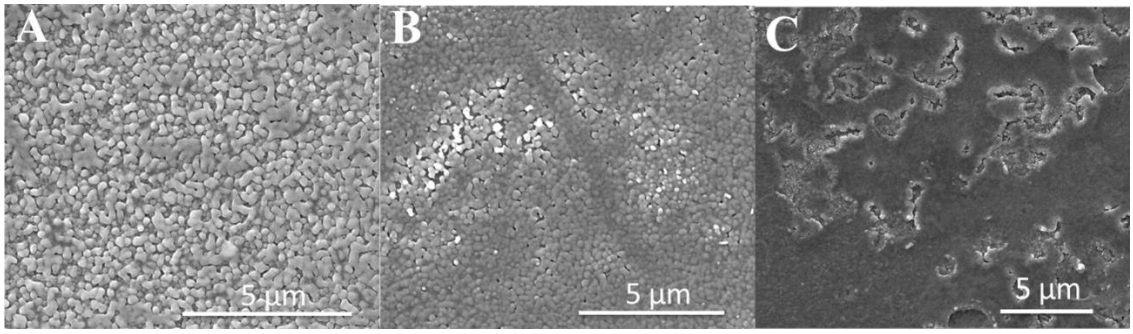

Figure 2.4: SEM images of selenium films deposited at a FTO electrode from 0.1 M $(CH_3CH_2O)_2Se{=}O$ in $[PP_{13}][TFSI]$/6 mol eq. CH_3CN at E = -1.7 V for (A) 10 min., (B) 30 min., and (C) 120 min.

Figures 2.3B and C show the UV-Vis spectra of a FTO electrode immersed in 0.1 M $(CH_3CH_2O)_2Se{=}O$ in $[PP_{13}][TFSI]$/6 mol eq. CH_3CN held at a deposition potential of -2.0 V and at the C3 peak potential (-2.5 V) shown in Fig 2.1, respectively. Initially, the absorbance spectrum for deposition at -2.0 V is nearly identical to the spectra for

deposition at -1.7 V, but after four minutes an absorption feature at ~550 nm starts to grow in, while the absorption feature at 315 nm decreases initially and then increases at the same rate as the other absorption features. As mentioned earlier, a red shift in the absorption spectra is likely the result of an increase in size of the selenium nanoparticles, but could also be due to structural or morphological changes in the deposit.[36] Figure S2.7A and B are SEM images of the deposit obtained by holding the potential at -2.0 V for 30 minutes. Se particles of various sizes form, some being several micrometers in diameter, in addition to worm-like structures. Endres and co-workers have found that the ionic liquid-electrode interface varies with choice of ionic liquid and the potential applied, which has been shown to affect electrodeposits.[37] No studies of the ionic liquid-FTO interface have been performed to date, so it is difficult to say how the solvation layers influence the electrode surface and the deposit. In addition, the reduction of SnO_2 is also occurring to a greater extent at this potential, which may influence the morphology. Electrodeposition at the C3 peak potential produces UV-Vis spectra that bear no resemblance to the spectra obtained during the deposition at the C2 peak potential. Instead, a broad absorbance feature grows in that resembles the growth of a-Se nanoparticles with ~120-180 nm diameter.[34] After 15 minutes a peak emerges at ~550 nm that resembles the absorbance of nanoparticles with diameters 150-200 nm.[34] During the electrodeposition an insoluble red species was observed to form near the electrode surface. This is speculated to be colloidal selenium nanoparticles, which has been observed in aqueous media.[9] Absorption by colloidal selenium formed near the surface of the FTO electrode would complicate the correlation between the electrodeposition of elemental selenium and the UV-Vis measurements. The formation of colloidal selenium is likely the reason for the large increase in dA_{550}/dE seen at -2.5 V in the first scan of the DCVA at 550 nm. Colloidal selenium nanoparticles are likely the result of a

comproportionation reaction involving $(CH_3CH_2O)_2Se{=}O$ and Se^{2-} as mentioned earlier. At this potential Se was observed to form non-continuous deposits, containing aggregates of various shapes and sizes on the electrode (Fig. S2.7C and D).

It should be noted that amorphous and vitreous selenium films have been observed to crystallize upon irradiation with visible light.[38,39] After each electrodeposition measurement the film was analyzed by SEM to confirm that the morphology of the deposit in the presence and absence of light from the UV-Vis spectrometer were the same. We found that limiting the UV-Vis measurements to once a minute resulted in films that were identical to the films deposited in the absence of light from the spectrometer. To further confirm the phase and composition of the selenium films Raman spectroscopy and XPS were employed.

2.3.3 Thin Film Characterization

Glancing angle X-ray diffraction (XRD) was employed to investigate the phase and crystallinity of the Se deposits. Figure S2.8 shows the XRD pattern obtained for a Se film deposited at -1.7 V for 1 hour. There is very little change observed between the Se film deposited at -1.7 V and a clean FTO electrode. No peaks corresponding to any Se phase appear in the deposit, which indicates that the Se films are amorphous. The most notable difference between the clean FTO sample and the Se film deposited at -1.7 V is the increased intensity of the peak at 23.1° and the peak at 26.7° corresponding to the (110) reflection of FTO. The change in intensity of the FTO peaks could indicate restructuring of the FTO electrode surface caused by either the deposition of Se or more likely the reduction of FTO. No peaks corresponding to crystalline SnO or Sn were observed.

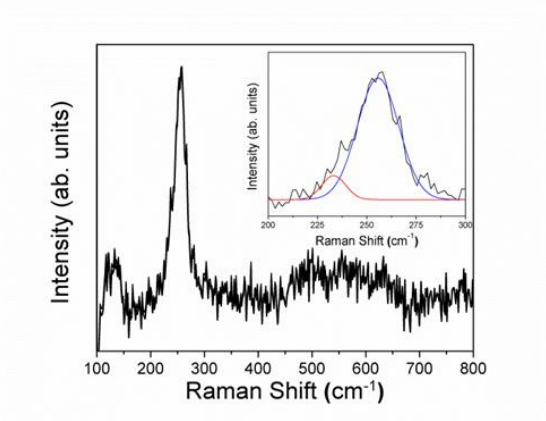

Figure 2.5: Raman spectra of deposition of selenium films on FTO electrodes immersed in 0.1 M $(CH_3CH_2O)_2Se{=}O$ in $[PP_{13}][TFSI]$/6 mol eq. CH_3CN at -1.7 V for 2 hours at room temperature. In the inset: Enlarged image of 200-300 cm^{-1} region with Gaussian curve fit.

Raman spectroscopy was used to further investigate the phase of the electrodeposited selenium. Figure 2.5 shows the Raman spectrum of a deposit obtained by poising the potential at C2 for 2 hours. A strong feature at 255 cm^{-1} (inset Fig. 2.5: blue curve) appears in the spectra, close to the E_2 vibrational mode of Se_8 rings found in monoclinic selenium (m-Se).[40] The inset of Fig. 2.6 shows a close up of the main peak fit with Gaussian functions. There is clearly a shoulder centered at 234 cm^{-1} (inset Fig. 2.5: red curve), which is attributed to the E vibrational mode of trigonal selenium chains, but could also have contribution from the A_1 vibrational mode of t-Se.[40] Amorphous selenium is thought to consist of both modifications of crystalline selenium, Se_8 rings (m-Se) and polymeric chains (t-Se), assembled in a disordered nature.[41] In amorphous selenium the width of the peaks was found to be independent of temperature, which was attributed to the disordered nature of the phase.[41] The full width at half maximum of both of the peaks are much broader than what has been reported previously for trigonal or

monoclinic phases (5 cm^{-1}) at room temperature.[41] Although others have suggested the broadness of the peak could be due to the overlap of all Raman active modes, which can be resolved by low temperature measurements.[36] A broad scattering feature below ~145 cm^{-1} is also present. This feature is likely the result of the convolution of several vibrational modes, including the E mode of polymeric Se chains at 138 cm^{-1}.[40] The A_1 mode attributed to Se_8 rings at 112 cm^{-1} was not observed due to the cut-off of optical filters at low wavenumbers. Raman scattering observed between 450 – 550 cm^{-1} is due to overtone of the peak at 255 cm^{-1}, that appears due to the resonant nature of the scattering with 514.5 nm excitation.[42] The peaks observed from 550 – 650 cm^{-1} are due to the FTO substrate.

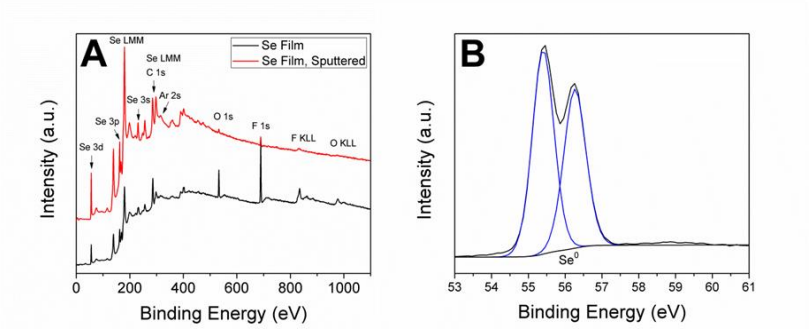

Figure 2.6: XPS analysis of electrodeposited Se films. (A) Survey of Se film as placed in the XPS analysis chamber and after sputtering. (B) XPS analysis of Se 3d region of the sputtered Se film. Black curve: Signal from Se 3d region and Shirley background. Blue curves: Se^0 fit.

The Se films were further examined using XPS. Fig. 2.6A shows a survey scan of a film deposited at the C2 peak potential. It is often challenging to completely remove ionic liquids after electrodeposition as evidenced by the oxygen 1s and fluorine 1s signals

in the as deposited Se film. Sputtering the sample with Ar ions for a short time (15 s) reduces the O 1s and F 1s signal by 83% and 81%, respectively. Residual fluorine and oxygen signals may originate from the FTO electrode. It was not possible to differentiate the C 1s peak from the Se LMM Auger peak at ~287 eV quantitatively. Although, the convoluted C 1s and Se LMM peak appears much larger in the as deposited film than the Ar^+ sputtered film, suggesting a possible decrease in the carbon content of the film. This spectral overlap also prevents the determination of any residual CH_3CN incorporated into the film.

Figure 2.6B shows a high resolution spectrum of the Se 3d region. A doublet at 55.4 eV and 56.3 eV corresponding to emission from the Se $3d^{5/2}$ and $3d^{3/2}$ orbitals, respectively, are observed as shown by the blue curves. As mentioned earlier the carbon 1s peak was unable to be deconvoluted from the Se LMM peak so the Se 3d binding energies reported are uncorrected for charging, although they agree fairly well with what is reported in the literature.[43] Additionally, a peak shifted +3.3 eV from the Se $3d^{5/2}$ peak was observed which would be caused by a selenium species in a different chemical environment. The binding energy shift of SeO_2 has been reported to be between 3.5 – 4.4 eV, which suggests the peak at 58.7 eV is not due to SeO_2.[44] It should be noted that a similar feature is present in the reference spectra of the Se 3d region for a monochromated Al Kα source, suggesting its presence in pure selenium samples.[43] It has been suggested by the Endres group that this may be due to partial oxidation of the surface of the selenium film.[18,19] Analysis of the peak areas reveal that the peak Se^0 peaks correspond to 98% of the total peak area, while the partially oxidized peak corresponds to less than 2%.

CHAPTER 2.4 CONCLUSION

We have demonstrated a facile method for the electrodeposition of amorphous selenium films from diethyl selenite in 1-propyl-1-methylpiperidinium bis(trifluoromethylsulfonyl)imide at room temperature. The electrochemistry of diethyl selenite and the deposition mechanism for elemental selenium were elucidated using *in-situ* UV-Vis spectroelectrochemistry. Three reduction peaks were observed in the cyclic voltammogram of diethyl selenite. Derivative cyclic voltabsorptometry revealed that the peaks were due to the reduction of a selenium species adsorbed on the electrode, the bulk deposition of selenium, and the further reduction of deposited selenium to Se^{2-}. Deposition at -1.7 V results in selenium depositing as nanoparticles followed by coalescence to produce a continuous film. As the potential was moved to more negative values larger particles formed, aggregation occurred, and colloidal selenium was observed. During the spectroelectrochemical measurements a photoreduction current was observed, a result of the p-type photoconductivity of the electrodeposited selenium films. Raman spectroscopy showed that the selenium films were amorphous in nature, consisting of Se_8 rings and polymeric Se chains. X-ray photoelectron spectroscopy and energy dispersive X-ray spectroscopy confirmed that films consisted of metallic Se^0 with minor surface impurities from the electrodeposition process.

CHAPTER 2.5 REFERENCES

(1) Kasap, S.; Frey, J. B.; Belev, G.; Tousignant, O.; Mani, H.; Laperriere, L.; Reznik, A.; Rowlands, J. A. *Phys. Status solidi* **2009**, *246*, 1794–1805.

(2) Tanaka, K.; Shimakawa, K. *Amorphous chalcogenide semiconductors and related materials*; Springer Science & Business Media, 2011.

(3) Chhowalla, M.; Shin, H. S.; Eda, G.; Li, L.-J.; Loh, K. P.; Zhang, H. *Nat. Chem.* **2013**, *5*, 263–275.

(4) Mikla, V. I.; Mikla, V. V. *Amorphous Chalcogenides: The Past, Present and Future*; Elsevier, 2011; Vol. 145.

(5) Bindu, K.; Lakshmi, M.; Bini, S.; Kartha, C. S.; Vijayakumar, K. P.; Abe, T.; Kashiwaba, Y. *Semicond. Sci. Technol.* **2002**, *17*.

(6) Mane, R. S.; Lokhande, C. D. *Mater. Chem. Phys.* **2000**, *65*, 1–31.

(7) Nagels, P.; Sleeckx, E.; Callaerts, R.; Tichy, L. *Solid State Commun.* **1995**, *94*, 49–52.

(8) Lazell, M.; O'Brien, P.; Otway, D. J.; Park, J.-H. *J. Chem. Soc. Dalton Trans.* **2000**, 4479–4486.

(9) Graham, A. K.; Pinkerton, H. L.; Boyd, H. J. *J. Electrochem. Soc.* **1959**, *106*, 651–654.

(10) Von Hippel, A.; Bloom, M. C. *J. Chem. Phys.* **1950**, *18*, 1243–1251.

(11) Lai, Y.; Liu, F.; Li, J.; Zhang, Z.; Liu, Y. *J. Electroanal. Chem.* **2010**, *639*, 187–192.

(12) Santos, M. C.; Machado, S. A. *J. Electroanal. Chem.* **2004**, *567*, 203–210.

(13) Cabral, M. F.; Pedrosa, V. A.; Machado, S. A. S. *Electrochimica Acta* **2010**, *55*, 1184–1192.

(14) Endres, F.; MacFarlane, D.; Abbott, A. *Electrodeposition from ionic liquids*; John Wiley & Sons, 2008.

(15) El Abedin, S. Z.; Saad, A. Y.; Farag, H. K.; Borisenko, N.; Liu, Q. X.; Endres, F. *Electrochimica Acta* **2007**, *52*, 2746–2754.

(16) Chou, L.-H.; Sun, I.-W.; Hussey, C. L. *ECS Trans.* **2010**, *33*, 575–579.

(17) Steichen, M.; Dale, P. *Electrochem. Commun.* **2011**, *13*, 865–868.

(18) Aal, A. A.; Voigts, F.; Chakarov, D.; Endres, F. *Electrochimica Acta* **2012**, *59*, 228–236.

(19) Aal, A. A.; Voigts, F.; Chakarov, D.; Endres, F. *J. Solid State Electrochem.* **2012**, *16*, 3027–3036.

(20) Kaim, W.; Fiedler, J. *Chem. Soc. Rev.* **2009**, *38*, 3373–3382.

(21) Dunsch, L. *J. Solid State Electrochem.* **2011**, *15*, 1631–1646.

(22) Lahiri, A.; Olschewski, M.; Höfft, O.; Zein El Abedin, S.; Endres, F. *J. Phys. Chem. C* **2013**, *117*, 1722–1727.

(23) Cooper, W. C.; Zingaro, R. A. *Selenium*; Van Nostrand Reinhold, 1974.

(24) Leiga, A. G. *JOSA* **1968**, *58*, 1441–1445.

(25) Mehrotra, R. C.; Mathur, S. N. *J. Indian Chem. Soc* **1964**, *41*.

(26) Saji, V. S.; Lee, C.-W. *RSC Adv.* **2013**, *3*, 10058–10077.

(27) Bougouma, M.; Van Elewyck, A.; Steichen, M.; Buess-Herman, C.; Doneux, T. *J. Solid State Electrochem.* **2013**, *17*, 527–536.

(28) Tachikawa, N.; Katayama, Y.; Miura, T. *ECS Trans.* **2009**, *16*, 589–595.

(29) Wang, Y.; Rogers, E. I.; Compton, R. G. *J. Electroanal. Chem.* **2010**, *648*, 15–19.

(30) Zhu, Y.-L.; Katayama, Y.; Miura, T. *Electrochimica Acta* **2010**, *55*, 9019–9023.

(31) Bancroft, E. E.; Sidwell, J. S.; Blount, H. N. *Anal. Chem.* **1981**, *53*, 1390–1394.

(32) Bard, A. J.; Faulkner, L. R.; Leddy, J.; Zoski, C. G. *Electrochemical methods: fundamentals and applications*; Wiley New York, 1980; Vol. 2.

(33) Hahn, B. P.; Stevenson, K. J. *J. Electroanal. Chem.* **2010**, *638*, 151–160.

(34) Lin, Z.-H.; Wang, C. C. *Mater. Chem. Phys.* **2005**, *92*, 591–594.

(35) Rajalakshmi, M.; Arora, A. K. *Solid State Commun.* **1999**, *110*, 75–80.

(36) Raevskaya, A. E.; Stroyuk, A. L.; Kuchmiy, S. Y.; Dzhagan, V. M.; Zahn, D. R.; Schulze, S. *Solid State Commun.* **2008**, *145*, 288–292.

(37) Atkin, R.; El Abedin, S. Z.; Hayes, R.; Gasparotto, L. H.; Borisenko, N.; Endres, F. *J. Phys. Chem. C* **2009**, *113*, 13266–13272.

(38) Dresner, J.; Stringfellow, G. B. *J. Phys. Chem. Solids* **1968**, *29*, 303–311.

(39) Poborchii, V. V.; Kolobov, A. V.; Tanaka, K. *Appl. Phys. Lett.* **1998**, *72*.

(40) Lucovsky, G.; Mooradian, A.; Taylor, W.; Wright, G. B.; Keezer, R. C. *Solid State Commun.* **1967**, *5*, 113–117.

(41) Mooradian, A.; Wright, G. B.; Cooper, W. C. *Pergamon Press. Oxf.* **1969**.

(42) Ohta, N.; Scheuermann, W.; Nakamoto, K. *Solid State Commun.* **1978**, *27*, 1325–1327.

(43) Chastain, J.; King, R. C.; Moulder, J. F. *Handbook of X-ray photoelectron spectroscopy: a reference book of standard spectra for identification and interpretation of XPS data*; Physical Electronics Eden Prairie, MN, 1995.

(44) Shenasa, M.; Sainkar, S.; Lichtman, D. *J. Electron Spectrosc. Relat. Phenom.* **1986**, *40*, 329–337.

Chapter 3: Electrodeposition of Amorphous Molybdenum Chalcogenides from Ionic Liquids and their Activity for the Hydrogen Evolution Reaction

3.1 Introduction

Molybdenum sulfide and molybdenum selenide are materials of interest due to their interesting physical, chemical, and electronic properties. These materials have been investigated as replacements for platinum in the electrocatalysis of hydrogen, alternatives to graphene for field effect transistors, and for energy storage applications.[1–4] These materials are commonly produced through high temperature processes, chemical or physical vapor deposition, that often require the use of highly toxic reagents.[5–9] Electrodeposition offers an alternative method to prepare these materials that has several advantages of other methods, including lower cost and scalability. Molybdenum sulfide and selenide has been electrodeposited from aqueous conditions before with mixed results. Several groups have reported the use of $[MoS_4]^{2-}$ ion to serve as a precursor for the electrodeposition of thin films of MoS_x (x = 2 – 3).[10–12] The stoichiometry of these films can be controlled depending on the regime that the electrodeposition occurs. In anodic regimes the films tend towards MoS_3, while in cathodic regimes they tend towards MoS_2, cycling between the 2 regimes ends up with an intermediate value of sulfur.[13] The presence of water in the deposition bath can be problematic leading to oxidation of the

precursors or oxidation of the deposited film. Investigation into the use of non-aqueous solvents with these materials has been minimal and ionic liquids are an excellent candidate for electrodeposition solvent-electrolyte system.[14,15]

Recently, our group has shown that ionic liquids are promising alternative electrolyte systems for the deposition of reactive metals and compounds that cannot traditionally be deposited from aqueous environments.[16–19] Ionic liquids have garnered interest due to their interesting physical and chemical properties such as large electrochemical windows, low volatility, high thermal stability, and the absence of water and lack of reactive oxygen species.[20] Murugesan et al. has developed a method for the electrodeposition of MoS_2 from 1-methyl-1-propylpiperidinium bis(trifluoromethanesulfonyl)imide (PP_{13}-TFSI) using molybdenum glycolate and 1,4-butanedithiol as precursors.[17] An analogous method for the electrodeposition of $MoSe_2$ is difficult to develop using this method as 1,4-butanediselenol due to concerns about the toxicity of the volatile chemical. A single precursor method was adopted in favor due to its simplicity and safety. Based on previous work in aqueous conditions $[MoE_4]^{2-}$ was the ideal candidate for a single site precursor.

In this work we describe a general method for the electrodeposition of MoE_x (E = S, Se) films using $[MoE_4]^{2-}$ ions as precursors in 1-ethyl-3-methylimidazolium bis(trifluoromethanesulfonyl)imide (EMIM-TFSI). Cyclic voltabsorptometry was used to investigate the electrochemistry and electrodeposition mechanism of the $[MoE_4]^{2-}$ precusors. The films were characterized using several techniques (X-ray photoelectron spectroscopy, Raman spectroscopy, scanning electron microscopy). Lastly, the activity for the hydrogen evolution reaction was investigated using linear sweep voltammetry.

3.2 EXPERIMENTAL

3.2.1 Chemicals

Ammonium tetrathiomolybdate ($[NH_4]_2[MoS_4]$, 99.97%) was obtained from Sigma-Aldrich. N-Methylpiperidine (MePip, 99%) was obtained from VWR. Anhydrous diethyl ether (ACS Grade), acetone (ACS Grade), dichloromethane (ACS Grade), and sulfuric acid (H_2SO_4, ACS Plus) were purchased from Fisher Scientific. Absolute ethanol (ACS Grade) was purchased from Pharmco-Aaper. 1-Ethyl-3-methylimidazolium bis(trifluoromethylsulfonyl)imide (EMIM-TFSI, 99%) was obtained from IoLiTec. EMIM-TFSI was dried in a vacuum oven at 100 °C for at least 24 hours prior to use and stored in an Innovative technology glovebox with concentrations of oxygen and water below 1 ppm. All water was purified to 18.2 MΩ-cm using a Barnstead E-pure purification system. All chemicals were used as received unless otherwise mentioned.

3.2.2 Synthesis of $[Ph_4P]_2[MoS_4]$

$[Ph_4P]_2[MoS_4]$ was synthesized by modifying a published procedure.[21] Briefly, $[NH_4]_2[MoS_4]$ (0.250 g, 0.960 mmol) and $[Ph_4P][Cl]$ (0.756 g, 2.02 mmol) were added to 25 mL of acetonitrile. The reaction was placed under a nitrogen atmosphere and stirred for 24 hours. The solution was filtered, the insoluble product was washed with CH_3CN, and the filtrate was collected. The solvent was evaporated using a Rotovap and the solid was dissolved in 8 mL of CH_3CN. The product remained insoluble and was then filtered and washed with ethanol and diethyl ether. This product was a red powder (Yield = 17%). UV-Vis (in CH_3CN): 268 nm, 275 nm, 322 nm, 474 nm.

3.2.3 Synthesis of $[Ph_4P]_2[MoSe_4]$

$[Ph_4P]_2[MoSe_4]$ was synthesized by following a published procedure.[22] Reaction was carried out in a N_2 glovebox. Briefly, K_2Se_3 was prepared by adding the appropriate

stoichiometric amounts of elemental potassium and selenium to a reaction flask in dry ammonia at -78 °C and stirring for 2h. The liquid ammonia was removed leaving a grey powder. Two equivalents of K_2Se_3 were added to one equivalent of $Mo(CO)_6$ in dimethylformamide (DMF) and the solution was heated to 90 °C for 1h. Following this two equivalents of $(C_6H_5)_4PBr$ were added to the solution and the solution was filtered. An equal volume of diethyl ether was added and stored at 4 °C overnight. The resulting product was bright purple crystals.

3.2.4 Electrochemical Measurements

The electrodeposition experiments were carried out on a CHI 440 potentiostat/galvanostat with a glass cup three electrode cell. Prior to experiments the cell was soaked in a 3:1 H_2SO_4:H_2O_2 Piranha solution for 24 hours followed by neutralization with $NaHCO_3$, sonication in water for 1 hour, and dried in an oven at ~100 °C overnight. All electrodeposition experiments were performed in a glovebox. Glassy carbon (GC, Alfa Aesar) slabs were employed as the working electrode for characterization of the films and a glassy carbon rotating disk electrode (Pine Research Instrumentation, d = 0.5 cm) was employed for all hydrogen evolution reaction tests. These electrodes were polished with 0.050 μm alumina slurry on microcloth (Buehler), sonicated in 18.2 MΩ-cm water to remove the residual alumina powder, and dried in an oven at ~100 °C for 24 hours prior to experiments. The counter electrode and quasi – reference electrode (QRE) used in these experiments were a platinum mesh and a platinum wire, respectively. The electrodes were placed directly in the deposition bath. Platinum was used as the QRE as an alternative to silver, which has been observed to dissolve in ionic liquids and contaminate electrodes. It should be noted that drifts in the potential up to 200 mV in platinum QRE have been observed. The potential in reference to ferrocene could not be

determined due to a reaction between ferrocene and the molybdenum chalcogenide precursors. The reaction between M^{2+} ions and MoX_4^{2-}(X = S, Se) has been known to lead to various soluble and insoluble products in aqueous and non-aqueous media alike.[23] Before use the platinum counter and quasi – reference electrode were cleaned by heating in a propane flame. After deposition experiments the working electrode was removed from the glovebox and subsequently washed with ethanol, acetone, and dichloromethane to remove residual ionic liquid present.

Hydrogen evolution reaction (HER) tests were performed on an Autolab PGSTAT30 Potentiostat interfaced with Autolab GPES software (version 4.9). A 120 mL 5-neck flask was fitted with a GC rotating disk electrode connected to a Pine Instruments AFMSRX Analytical Rotator. For the rotating disk experiments the rotation rate used was 3000 rpm. A 0.5 M H_2SO_4 solution was used as the electrolyte. All HER experiments were conducted with a graphite rod as the counter electrode and Hg/Hg_2SO_4 (sat. K_2SO_4, CH Instruments) as the reference electrode. The reference electrode was calibrated against the reversible hydrogen electrode (RHE). This was done by placing a platinum electrode in the electrolyte and bubbling hydrogen gas through it. The open circuit potential was recorded and the potential was swept at 1 mV/s starting from 10 mV below to 10 mV above the open circuit potential.

3.2.5 Characterization of Electrodeposited Films

The electrodeposited films were characterized using several techniques. Scanning electron microscopy was performed on a FEI Quanta 650 FEG ESEM. Particle sizes measured using ImageJ 1.47v. Films were coated with a thin layer of Au/Pd to ensure conductivity of the films. Raman spectroscopy was carried out on a Renishaw inVia microscope with a 514.5 nm Ar laser in the backscattering configuration. The Stoke's

Raman signal at 521 cm^{-1} of a bulk Si [110] single crystal was used to calibrate the instrument. The laser was operated at low powers (5 %, <0.5 mW) to prevent photocrystallization or degradation of the molybdenum chalcogenide films. X-ray photoelectron spectra were collected on a Kratos Axis Ultra DLD X-ray photelectron spectroscopy (XPS) system and analysed along the same methods as our previous work.[18] Survey scans were recorded with a 1 eV resolution, followed by high resolution scans (0.1 eV, 2s dwell time) of the carbon 1s, oxygen 1s, molybdenum 3d, sulfur 2p, and selenium 3d regions.

3.3 Results and Discussion

EMIM-TFSI was chosen as the solvent-electrolyte system for our deposition experiments because of its ability to solubilize the molybdenum chalcogenide precursors. We tried several different ionic liquid cations, including 1-methyl-1-propylpiperidinium and 1-methyl-1-butylpyrrolidinium, with the TFSI anion and found only EMIM showed significant solvation of our precursors. We have attributed this difference in solubility to be due to the hydrogens located at the C2, C4, and C5 positions of the imidazole ring, which have been shown to participate in hydrogen bonding

3.3.1 Electrochemsitry of $[MoS_4]^{2-}$ and $[MoSe_4]^{2-}$

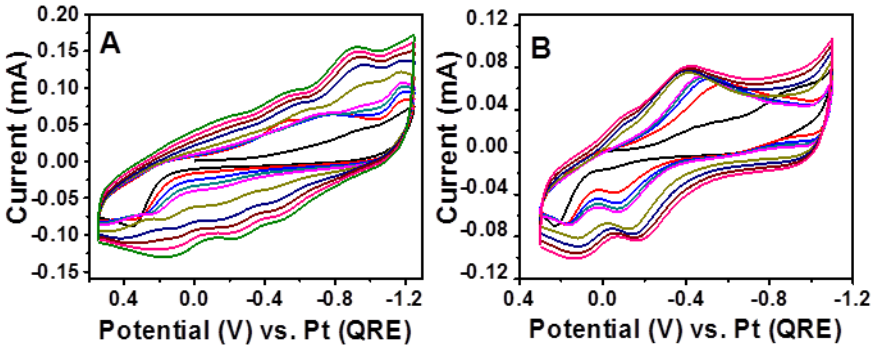

Figure 3.1: Cyclic voltammetric deposition of (a) MoS_x and (b) $MoSe_x$ from 0.005 M $[Ph_4P]_2[MoS_4]$ and 0.005 M $[Ph_4P]_2[MoSe_4]$, respectively, scans 1-10, 20, 30, 40 50. Working electrode = glassy carbon, scan rate = 50 mV/s.

Cyclic voltammetry was carried out on the $[Ph_4P]_2[MoS_4]$- and $[Ph_4P]_2[MoSe_4]$-EMIM-TFSI solutions and the resulting curves are displayed in figure 3.1a and b, respectively. Similar to what Merki et al. observed, we saw that with each subsequent scan the current increases, which suggests that the electrode area is increasing due to the deposition of MoS_x or $MoSe_x$. The deposit was visible following cycling experiments. We also observed oxidation and reduction peaks that grew in with increasing number of scans for both of the precursors. For $[MoS_4]^{2-}$ oxidation peaks were found to grow in at -0.25 and -0.5 V vs. Pt and reduction peaks at -0.55 V and -0.9 V vs. Pt. For $[MoSe_4]^{2-}$ the oxidation and reduction peaks grew in at -0.2 and -0.4 V vs. Pt, respectively. Further studies are needed to identify these processes.

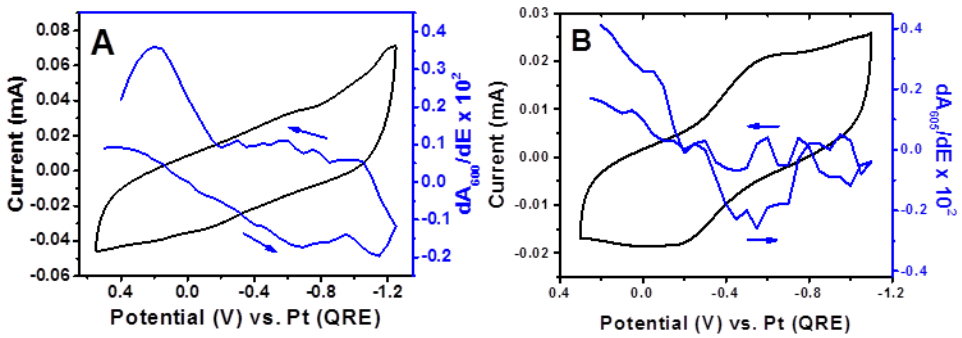

Figure 3.2: 25th scan of the cyclic voltammogram and corresponding derivative cyclic voltabsorptogram of (a) 0.005 M $[Ph_4P]_2[MoS_4]$ and (b) 0.005 M $[Ph_4P]_2[MoSe_4]$ on an FTO electrode. (a) λ = 600 nm, (b) λ = 605 nm, scan rate = 50 mV/s.

To further investigate the electrochemical processes of the molybdenum chalcogenide precursors we turned to *in-situ* ultraviolet-visible spectroelectrochemistry. In figures 3.2a and b the 25th scan of the CV deposition of $[Ph_4P]_2[MoS_4]$ and $[Ph_4P]_2[MoSe_4]$, respectively, is plotted alongside the corresponding derivative cyclic voltabsorptogram (DCVA) at a single wavelength. In figure 3.2a on the cathodic scan we see a large decreasing change in the absorbance that has a peak at approximately -0.7 V, which we have attributed to the corrosion reaction observed by Vrubel et al.[13]

$$MoS_3 + 1/8\,S_8 + 2e^- \rightarrow [MoS_4]^{2-} \quad (1)$$

There is no indication from the DCVA that the reduction of tetrathiomolybdate to MoS_2 is occurring. This reduction occurs by the following reaction:

$$[MoS_4]^{2-} + 4H^+ + 2e^- \rightarrow MoS_2 + H_2S \quad (2)$$

This is not surprising as we are working in an aprotic media. Ponomarev et al. were only able to observe the reduction of tetrathiomolybdate to MoS_2 in ethylene glycol by adding an excess concentration of NH_4Cl to act as a proton donor.[24] This is further corroborated by examining the DCVA of the first scan (Supplementary Fig S3.1), where no increase in dA_{600}/dE is observed when scanning to negative potentials. On the anodic scan we see that dA_{600}/dE becomes positive quite quickly and continues to increase until it reaches a peak at ~0.2 V, which we have attributed to the following reaction observed by Laperriere et al.[11]:

$$[MoS_4]^{2-} \rightarrow MoS_3 + 1/8\,S_8 + 2e^- \quad (3)$$

The DCVA of $[MoSe_4]^{2-}$ shows that it undergoes similar chemistry to $[MoS_4]^{2-}$. As we scan to positive potentials we see an increase in dA_{605}/dE, which we attribute to a reaction analogous to (3):

$$[MoSe_4]^{2-} \rightarrow MoSe_3 + 1/n\ Se_n + 2e^- \quad (4)$$

When the scanning to more negative potentials we see a decrease in dA_{605}/dE that has a peak, ca. -0.55 V, attributed to corrosion reactions analogous to (1):

$$MoSe_3 + 1/n\ Se_n + 2e^- \rightarrow [MoSe_4]^{2-} \quad (5)$$

As the potential is decreased to ca. -0.8 V the dA_{605}/dE becomes slightly greater than zero, which may indicate that reactions (5) may be competing with a reduction process that is creating more $MoSe_x$ on or near the surface of the electrode. The reaction creating $MoSe_x$ may be analogous to reaction (2):

$$[MoSe_4]^{2-} + 4H^+ + 2e^- \rightarrow MoSe_2 + H_2S \quad (6)$$

There are no protons in solution to facilitate this reaction, but this reaction may proceed to a very small extent in the absence of protons.

3.3.2 X-Ray Photoelectron Spectroscopy of MoS_x and $MoSe_x$ films

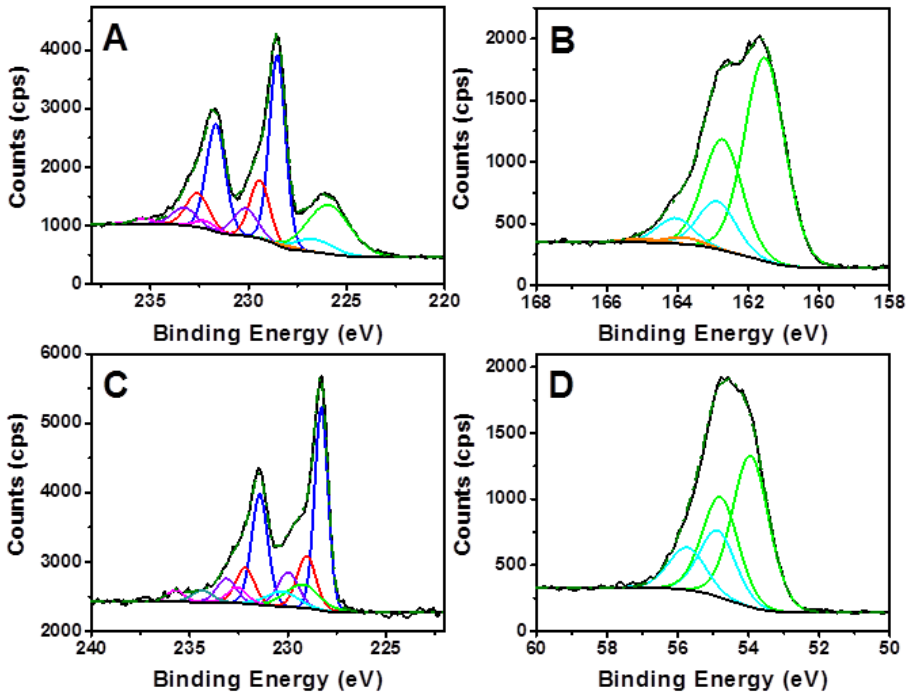

Figure 3.3: X-ray photoelectron spectra of the MoS_x film, (a) Mo 3*d* and (b) S 2*p*, and of the $MoSe_x$ film, (c) Mo 3*d* and (d) Se 3*d*.

XPS survey spectra of the film deposited from $[Ph_4P]_2[MoS_4]$ and $[Ph_4P]_2[MoSe_4]$ shows a strong presence of Mo and S or Mo and Se in the films, respectively, as well as C, O, N and F, which are from residual ionic liquid and adventitious impurities (Supplementary Fig. 3.2a and b). Figure 3.3a and b shows the high resolution Mo 3*d* and S 2*p* XPS spectra of the MoS_x film, respectively. The largest Mo $3d_{5/2}$ peak of the MoS_x film has a binding energy centred at 228.5 eV, indicating the presence of Mo^{4+} ions, which we attribute to MoS_x.[25–27] The S 2*p* spectrum shows three doublets with the $2p_{3/2}$ peak centred at 161.5, 162.9, and 163.9 eV. The first two peaks we attribute to the S^{2-} and S_2^{2-} ions, which is similar to what others have observed.[10,13,27] The ratio of these peaks

was not determined due to the possible overlap of other sulfur species.[27] The peak centred at 163.9 eV is attributed to elemental sulfur. Figure 3.3c and d show high resolution XPS spectra of the Mo 3*d* and Se 3*d* regions, respectively. The largest Mo $3d_{5/2}$ peak of the $MoSe_x$ film has a binding energy centred at 228.3 eV, which we attribute of Mo^{4+} ions of $MoSe_x$. The fit of the Se 3*d* spectrum shows two doublets with Se $3d_{5/2}$ centred at 53.9 eV and 54.9 eV. We attribute these peaks to Se^{2-} and Se_2^{2-}. Based on the fit of the Mo 3*d* spectra of the MoS_x film there are three other Mo doublets observed with Mo $3d_{5/2}$ peaks centred at 229.4, 230.1, and 232.2 eV, which account for 23, 13, and 3% of the total Mo ions, repsectively. The fit of the Mo 3*d* spectrum of $MoSe_x$ is analogous to the MoS_x film, with three Mo $3d_{5/2}$ peaks centered at 229.0, 230.0, and 232.6 eV, accounting for 18, 13, and 6%, respectively, of the total Mo ions present. During XPS analysis the electrodes are briefly exposed to air when cleaned and transferred to the XPS chamber. Amorphous molybdenum sulfide is known to form a native oxide when exposed to air.[28] Thus, the peaks centred at 229.4 and 230.1 eV are attributed to molybdenum oxysulfide species, $MoS_{n-x}O_x$ (n=1-3, x = 1-2), in the 4+ and 5+ oxidation states, respectively. It has been shown in several thermal sulfidation studies of amorphous and crystalline MoO_3 that Mo undergoes a transition from $Mo^{6+} \rightarrow Mo^{5+} \rightarrow Mo^{4+}$ in the presence of H_2S/H_2.[29,30] When amorphous MoO_3 (or MoO_2-H_2O) was exposed to H_2S/H_2 at 25 °C it was observed that a molybdenum oxysulfide species formed and the Mo was partially reduced from $Mo^{6+} \rightarrow Mo^{5+}$.[29] We propose that the oxidation of amorphous molybdenum sulfide by air undergoes a similar pathway resulting in the following transitions $Mo^{4+} \rightarrow Mo^{5+} \rightarrow Mo^{6+}$. The peak centred at 232.2 eV corresponds to Mo^{6+}, likely from MoO_3.[29,31] The XPS results for the $MoSe_x$ film suggest that it undergoes a similar oxidation process upon exposure to air. The higher concentration of MoO_3 in the $MoSe_x$ films is the result of the difference in metal-chalcogenide bond strength (Mo–S > Mo–Se).

3.3.3 Characterization of Film Structure and Morphology

Raman spectroscopy of the MoS_x and $MoSe_x$ film is presented in figure 3.4a and b. The MoS_x films shows broad peaks centered at ~320 and ~450 cm^{-1}. The peak at 320 cm^{-1} is thought to be due to ν(Mo–S) vibrational mode and to the presence of bridging S_2^{2-} ligands. Although, the stretching modes, ν(S–S), of S_2^{2-} at ~ 525 cm^{-1} is very small if present in the spectrum at all, so the peak at 320 cm^{-1} should not be attributed to a ν(Mo–S) vibrational mode of a bridging S_2^{2-} as previously thought. The broad peak centered at 450 cm^{-1} is close to the symmetric ($\nu_1(A_1)$) and anti-symmetric ($\nu_3(F_2)$) stretching mode of the $Mo{=}S_{terminal}$ of the $[MoS_4]^{2-}$ anion and likely corresponds to similar vibrational modes in MoS_x.[27] The $MoSe_x$ films shows broad peaks centered at ~250 cm^{-1}. The peak centered at 250 cm^{-1} is close to the A^1_g vibrational mode of crystalline $MoSe_2$ (~242 cm^{-1}).[32] This peak could also be in part due to ν(Se–Se) stretching mode, commonly observed in amorphous selenium[18], although the peak is much too broad to be due solely to amorphous selenium.

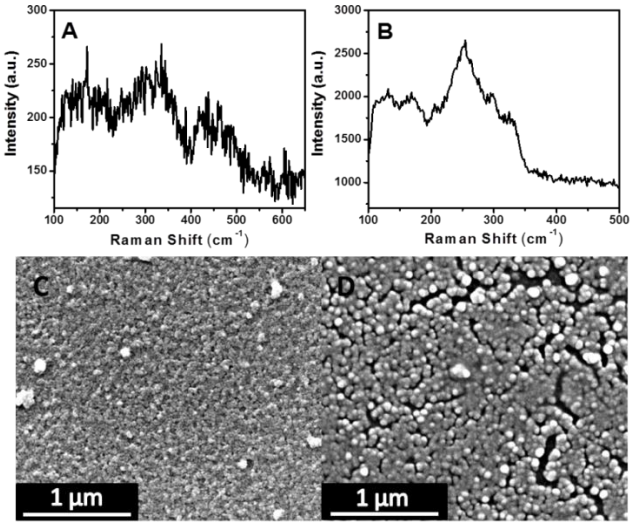

Figure 3.4: Raman spectroscopy of the (a) MoS_x film and (b) $MoSe_x$ film. Representative scanning electron microscopy images of (c) MoS_x film and (d) $MoSe_x$ film.

In figures 3.4c and d we have representative SEM images of films deposited by cycling for each of the precursors. SEM shows that the films consist of densely packed nanoparticles. The MoS_x and $MoSe_x$ films were found to have average particle sizes of 18 ± 6 and 42 ± 9 nm, respectively. In the MoS_x film it was common to find regions where clusters particles were deposited on top of the densely packed nanoparticle film (Supplementary Fig 3.3). The $MoSe_x$ film exhibited gaps in the nanoparticle film exposing the underlying surface. This is likely a result of reaction (5) occurring where $MoSe_x$ is being stripped off the surface.

3.3.4 Activity of MoS_x and $MoSe_x$ for the Hydrogen Evolution Reaction

The catalytic activity of the MoS_x and $MoSe_x$ films electrodeposited by 50 scans using cyclic voltammetry were measured by electrochemical methods. Figure 3.5a show the linear sweep voltammogram of MoS_x and $MoSe_x$ deposited on a glassy carbon rotating disk electrode in 0.5 M H_2SO_4. Both films show high activity for the hydrogen evolution reaction under these conditions. One metric of the activity is determining the potential where a particular current density is reached. For our purposes we chose 1 mA/cm^2 to be this current density as was done in our previous paper.[19] The MoS_x/GC films reaches this current density is E = -0.208 V vs. RHE and the $MoSe_x$/GC film reaches this current density at E = -0.230 V vs. RHE. These values lie only ~150 mV more negative than a platinum rotating disk electrode (E_{Pt} = -0.063V vs. RHE).

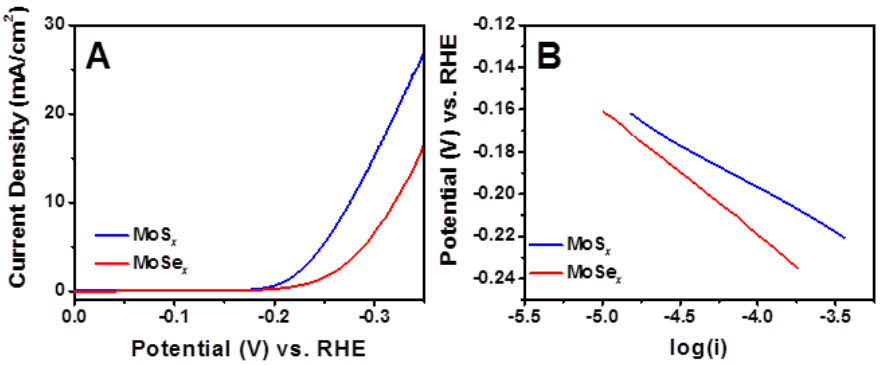

Figure 3.5: (A) Linear sweep voltammogram of the MoS_x and $MoSe_x$ films and (b) the corresponding Tafel plots. 0.5 M H_2SO_4, scan rate = 2 mV/s, ω = 3000 rpm.

The activity of these catalyst films were also examined by determining the Tafel slope. Figure 3.5b shows the Tafel plots of MoS_x and $MoSe_x$. The Tafel slope of MoS_x was 42 mV/decade and of $MoSe_x$ was 59 mV/decade. For molybdenum sulfide this is on par with what has been reported for other amorphous molybdenum sulfide (40 mV/decade),[10,28] while being much lower than MoS_2 crystals (55 to 60 mV/decade)[2] and nanoparticulate MoS_2 (120 mV/decade).[33] While the $MoSe_x$ slope is better than what has previously been reported in the literature; macroporous $MoSe_2$ (~80 mV/decade)[34] and vertically aligned $MoSe_2$ (105 to 120 mV/decade).[35] Only when coupled with reduced graphene oxide did the $MoSe_2$ nanosheets approach the Tafel slope we observed (~69 mV/decade).[36]

3.4 Conclusion

The discovery that the $[MoE_4]^{2-}$ (E = S, Se) serve as single precursors to the electrodeposition of amorphous molybdenum chalcogenides from EMIM-TFSI, which show high activity for the hydrogen evolution reaction has been reported. The

electrochemistry and the mechanism of electrodeposition of these precursors was investigated using *in-situ* UV-Vis spectroelectrochemistry, and found that both undergo an anodic deposition process and a cathodic corrosion reaction. Both films showed high activity for the hydrogen evolution reaction having Tafel slopes that were as good or exceeded previously reported values. This works brings up the question of will this deposition mechanism apply to other species of the $[ME_4]^z$ (where M = transition metal E = chalcogenide, and z = charge) type.

3.5 REFERENCES

(1) Chhowalla, M.; Shin, H. S.; Eda, G.; Li, L.-J.; Loh, K. P.; Zhang, H. *Nat. Chem.* **2013**, *5*, 263–275.

(2) Jaramillo, T. F.; Jorgensen, K. P.; Bonde, J.; Nielsen, J. H.; Horch, S.; Chorkendorff, I. *Science* **2007**, *317*, 100–102.

(3) Wang, Q. H.; Kalantar-Zadeh, K.; Kis, A.; Coleman, J. N.; Strano, M. S. *Nat. Nanotech* **2012**, *7*, 699–712.

(4) Chang, K.; Chen, W. *ACS Nano* **2011**, *5*, 4720–4728.

(5) Boscher, N. D.; Carmalt, C. J.; Palgrave, R. G.; Gil-Tomas, J. J.; Parkin, I. P. *Chem. Vap. Depos.* **2006**, *12*, 692–698.

(6) Serrao, C. R.; Diamond, A. M.; Hsu, S.-L.; You, L.; Gadgil, S.; Clarkson, J.; Carraro, C.; Maboudian, R.; Hu, C.; Salahuddin, S. *Appl. Phys. Lett.* **2015**, *106*, 052101.

(7) Lee, Y.-H.; Zhang, X.-Q.; Zhang, W.; Chang, M.-T.; Lin, C.-T.; Chang, K.-D.; Yu, Y.-C.; Wang, J. T.-W.; Chang, C.-S.; Li, L.-J.; Lin, T.-W. *Adv. Mater.* **2012**, *24*, 2320–2325.

(8) Liu, K.-K.; Zhang, W.; Lee, Y.-H.; Lin, Y.-C.; Chang, M.-T.; Su, C.-Y.; Chang, C.-S.; Li, H.; Shi, Y.; Zhang, H.; Lai, C.-S.; Li, L.-J. *Nano Lett.* **2012**, *12*, 1538–1544.

(9) Ling, Z. P.; Yang, R.; Chai, J. W.; Wang, S. J.; Leong, W. S.; Tong, Y.; Lei, D.; Zhou, Q.; Gong, X.; Chi, D. Z.; Ang, K.-W. *Opt. Express* **2015**, *23*, 13580.

(10) Merki, D.; Fierro, S.; Vrubel, H.; Hu, X. *Chem. Sci.* **2011**, *2*, 1262–1267.

(11) Bélanger, D.; Laperriére, G.; Marsan, B. *J. Electroanal. Chem.* **1993**, *347*, 165–183.

(12) Ponomarev, E. A.; Neumann-Spallart, M.; Hodes, G.; Levy-Clement, C. *Thin Solid Films* **1996**, *280*, 86–89.

(13) Vrubel, H.; Hu, X. *ACS Catal.* **2013**, *3*, 2002–2011.

(14) Albu-Yaron, A.; Levy-Clement, C.; Hutchison, J. L. *Electrochem. Solid-state Lett.* **1999**, *2*, 627–630.

(15) Albu-Yaron, A.; Levy-Clement, C.; Hutchison, J. L. *Electrochem. Solid-state Lett.* **1999**, *2*, 627–630.

(16) Murugesan, S.; Kearns, P.; Stevenson, K. J. *Langmuir* **2012**, *28*, 5513–5517.

(17) Murugesan, S.; Akkineni, A.; Chou, B. P.; Glaz, M. S.; Vanden Bout, D. A.; Stevenson, K. J. *ACS nano* **2013**, *7*, 8199–8205.

(18) Redman, D. W.; Murugesan, S.; Stevenson, K. J. *Langmuir* **2013**, *30*, 418–425.

(19) Redman, D. W.; Kim, H. J.; Stevenson, K. J.; Rose, M. J. *J. Mater. Chem.* **2016**, *4*, 7027–7035.

(20) Endres, F.; MacFarlane, D.; Abbott, A. *Electrodeposition from ionic liquids*; John Wiley & Sons, 2008.

(21) Wolff, T. E.; Berg, J. M.; Hodgson, K. O.; Frankel, R. B.; Holm, R. H. *J. Am. Chem. Soc.* **1979**, *101*, 4140–4150.

(22) O'Neal, S.; Kolis, J. W. *J. Am. Chem. Soc.* **1988**, *110*, 1971–1973.

(23) Müller, A.; Diemann, E.; Jostes, R.; Bögge, H. *Angew. Chem. Int. Ed. Engl.* **1981**, *20*, 934–955.

(24) Ponomarev, E. A.; Albu-Yaron, A.; Tenne, R.; Lévy-Clément, C. *J. Electrochem. Soc.* **1997**, *144*, L277–L279.

(25) Ganta, D.; Sinha, S.; Haasch, R. T. *Surf. Sci. Spectra* **2014**, *21*, 19–27.

(26) Grim, S. O.; Matienzo, L. J. *Inorg. Chem.* **1975**, *14*, 1014–1018.

(27) Weber, T.; Muijsers, J. C.; Niemantsverdriet, J. W. *J. Phys. Chem.* **1995**, *99*, 9194–9200.

(28) Benck, J. D.; Chen, Z.; Kuritzky, L. Y.; Forman, A. J.; Jaramillo, T. F. *Acs Catal.* **2012**, *2*, 1916–1923.

(29) Muijsers, J. C.; Weber, T.; Vanhardeveld, R. M.; Zandbergen, H. W.; Niemantsverdriet, J. W. *J. Catal.* **1995**, *157*, 698–705.

(30) Weber, T.; Muijsers, J. C.; Van Wolput, J. H. M. C.; Verhagen, C. P. J.; Niemantsverdriet, J. W. *J. Phys. Chem.* **1996**, *100*, 14144–14150.

(31) Sarma, D. D.; Rao, C. N. R. *J. Electron Spectrosc. Relat. Phenom.* **1980**, *20*, 25–45.

(32) Tonndorf, P.; Schmidt, R.; Böttger, P.; Zhang, X.; Börner, J.; Liebig, A.; Albrecht, M.; Kloc, C.; Gordan, O.; Zahn, D. R. *Opt. Express* **2013**, *21*, 4908–4916.

(33) Bonde, J.; Moses, P. G.; Jaramillo, T. F.; Nørskov, J. K.; Chorkendorff, I. *Faraday Discuss.* **2009**, *140*, 219–231.

(34) Saadi, F. H.; Carim, A. I.; Velazquez, J. M.; Baricuatro, J. H.; McCrory, C. C. L.; Soriaga, M. P.; Lewis, N. S. *ACS Catal.* **2014**, *4*, 2866–2873.

(35) Kong, D.; Wang, H.; Cha, J. J.; Pasta, M.; Koski, K. J.; Yao, J.; Cui, Y. *Nano Lett.* **2013**, *13*, 1341–1347.

(36) Tang, H.; Dou, K.; Kaun, C.-C.; Kuang, Q.; Yang, S. *J. Mater. Chem.* **2014**, *2*, 360–364.

Chapter 4: Photo-assisted Electrodeposition of MoS_x from Ionic Liquid on Organic-Functionalized Silicon Photoelectrodes for H_2 Generation [2]

CHAPTER 4.1 INTRODUCTION

There have been a considerable number of reports in the field of solar fuels using silicon photoelectrodes with surface functionalization – such as organics, microwires, nanowires[1–3], metal oxides (SiO_x, Al_2O_3, TiO_2)[4–6] and metal nanoparticles (Pt, Ni, Ni-Mo, Au)[7–10] – all to enhance photocatalytic activity. Silicon as a light-absorber is an attractive material due to its low cost and high earth abundance. One method used to enhance the electrochemical performance of silicon photoelectrodes is the modulation of energy barrier heights by surface modification using organic molecules. In the past decade, Lewis and co-workers have reported intriguing results demonstrating that different organic-modified Si(111) surfaces show different electrochemical performance, induced either by changes in the barrier height, surface dipole, or synergistic modulation of both. For example, H-terminated *p*-Si(111) showed a higher V_{OC} by 300 mV than CH_3-terminated *p*-Si(111) surface in acetonitrile solution containing diacetylcobaltocene.[11] In related work, we recently reported that the band edge modulation of a *p*-Si photocathode by surface functionalization with aromatic moieties, such as methyl, phenyl (Ph), napthyl, anthryl, and 3,5-dimethoxyphenyl (diOMe).[12] In particular, 3,5-dimethoxyphenyl-terminated Si substrate exhibited a high *p*-type energy barrier height (high V_{OC}), as well as a low series resistance due to its chemical (vis-à-vis electronic) connectivity with a TiO_2 thin film supporting platinum (Pt) nanoparticles as catalyst for hydrogen (H_2) evolution. The relatively low series resistance of 3,5-dimethoxyphenyl surface was postulated to emanate from an enhanced interaction between bulk Si and the coordinative

[2] Large parts of this chapter have been published as D.W. Redman, H.J. Kim, K.J. Stevenson, M.J. Rose, *J. Mater. Chem. A* **2016**, *4*, 7027. Reprinted with permissions from the Centre National de la Recherche Scientifique (CNRS) and The Royal Society of Chemistry.

TiO_2 layer via the oxygen moieties of $–OCH_3$ functional groups.[13–16] However, the prohibitive cost of Pt could prevent its widespread and low-cost application in solar fuels devices.

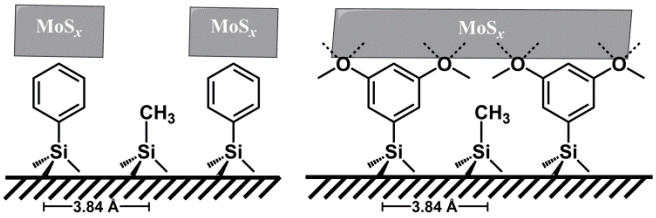

Scheme 4.1: Schematic representation of the *p*-Si(111)|R|MoS_x catalyst constructs utilized in this work (R = CH_3, Ph, 3,5-dimethoxybenzene).

The earth abundant catalyst molybdenum disulfide, MoS_2, has attracted great attention as an alternative catalyst for the hydrogen evolution reaction (HER), showing promise as a substitute for Pt. For example, Chorkendorff et al. reported results for molybdenum sulfide catalyst on metal passivated n^+p-Si photocathode; both a $MoS_x/MoS_2/n^+p$-Si heterostructure prepared by sputtering/sulfurization, and MoS_x/Ti/n^+p-Si photoelectrode prepared by electrodeposition exhibited an onset potential of 0.33 V vs. RHE in 0.1 M $HClO_4$ solution.[17,18] In related work, drop-cast Mo_3S_4 clusters on H-terminated Si(111) planar electrode displayed a shift in onset potential from -0.4 V to +0.15 V (vs. RHE) with 8 mA cm^{-2} of current density at 0 V (vs. RHE).[19] In two other cases, the research groups of Loo and Yang independently reported the integration of MoS_2 with silicon nanowire electrodes: an onset potential of +0.25 V (vs. RHE) for SiNW@MoS_2 in 1.0 M Na_2SO_4 buffer (pH 5.0); and +0.3 V (vs. RHE) for $MoS_2/TiO_2/n^+p$-Si NW in 0.5 M H_2SO_4.[20,21] Furthermore, Jin et al. investigated the catalytic activity of Si|MoS_2 with different crystal structures, based on preparation by

different deposition methods.[22] The as-grown MoS_2 (2H-MoS_2) prepared by chemical vapor deposition was converted to metallic MoS_2 (1T-MoS_2) by chemical exfoliation with *n*-BuLi. CVD 1T-MoS_2 showed a positive onset potential (+0.25 V vs. RHE), effected by a dramatic decrease in charge transfer of the catalytic reaction ($R_{ct\_CVD\ 1T}$ = 49.2 Ω-cm^2) compared to CVD 2H-MoS_2 (+0.23 V, $R_{ct\_CVD\ 2H}$ = 992.6 Ω-cm^2) and drop-casted 1T-MoS_2 (+0.23 V), $R_{ct\_DC\ 1T}$ = 212.4 Ω-cm^2). Jin and co-workers also examined the catalytic activity of amorphous MoS_xCl_y *p*-Si and found +0.27 V (vs. RHE) shift in the onset potential.[23] When this same material was interfaced with n^+p-Si micropyramids +0.41 V (vs. RHE) shift in the onset potential was observed.[24] And although MoS_2 seems to fit the requirement of HER catalyst, the deposition method such as sputtering, sulfurization, and CVD each present limitations of economy, safety and performance.

Electrodeposition offers an efficient, low cost, and scalable method to prepare thin films. It has been reported by several groups that the $[MoS_4]^{2-}$ ion serves as a precursor for the electrodeposition of amorphous MoS_x (x = 2–3).[25–27] The stoichiometry of the films can be controlled by the electrodeposition procedure; anodic deposition leads to the formation of MoS_3, while cathodic deposition leads to the formation of MoS_2. Merki and Vrubel et al. have shown that MoS_x deposited anodically, cathodically, and by cycling between the two regimes showed high activity for HER.[27,28] Much work to date has been performed in aqueous solutions, with the exception of two studies where MoS_2 was electrodeposited in ethylene glycol.[29,30] The presence of water in the deposition bath can lead to undesired oxidation of the substrate – or the deposited catalyst – thus leading to degradation in performance. Our group has shown that ionic liquids are promising alternative electrolytes for the electrodeposition of reactive metals and compounds that cannot typically be deposited in aqueous electrolytes, due to their large electrochemical windows, low volatility, and absence of water and reactive oxygen species.[31–33]

Electrodeposition on semiconductor surfaces can be enhanced by exposure to light. On *p*-type semiconductors light promotes an electron to the conduction band or a surface state that can then reduce a species in solution. Notably, light can also be used to control different aspects of the deposition. Kawamura et al. have shown that light can be used to control size and particle density for metals such as Co, Ni, and Cu.[34] In the case of Pt electrodeposition, the intensity of light has a similar effect to potential: higher intensity leads to small particles with a high particle density, while low light intensity leads to larger particles with a low particle density.[35] Platinum films on *p*-Si prepared by photo-assisted electrodeposition have been shown to outperform films prepared by electrodeposition in the dark, e-beam evaporation, or sputter deposition.[36,37]

Overall, in this work our aims were thus three-fold: (*i*) to characterize the electrochemical properties of the dimethoxyphenyl surface, (*ii*) to investigate its role in promoting or stabilizing MoS_x films during electrodeposition in ionic liquids, and (*iii*) to synergistically optimize the organic and inorganic components to maximize PEC performance for H_2 evolution. We have utilized surface characterization (contact angle, XPS, Raman) and electrochemical techniques (electrodeposition, spectroelectrochemistry, impedance spectroscopy, linear sweep voltammetry) to achieve these aims.

CHAPTER 4.2 EXPERIMENTAL

4.2.1 Preparation of Organic-Modified *p*-Si(111) Substrate

An organic-functionalized *p*-Si(111) wafer was prepared by a method analogous to our previous report.[12] A boron doped, Cz grown *p*-Si(111) wafer (single-side-polished, 450 ± 25 μm thick, Virginia Semiconductor Inc.) with 1.4-9 Ω-cm resistivity was used for organic functionalization of the surface. The *p*-Si(111) wafer washed with acetone,

ethanol, and water with sonication for 10 min in each solvent. The substrate was immersed in a Piranha solution, prepared by 3:1 volume mixture of H_2SO_4 (96.6%, Fisher Scientific) and H_2O_2 (30%, Fisher Scientific), at 90 °C for 20 min. In the following step, the Si wafer was etched in a HF(aq) solution (semiconductor grade, Transene Company, Inc.) for 20 s at room temperature. The atomically flat H-terminated Si(111) surface was then generated by immersing the wafer in a degassed NH_4F(aq) solution (semiconductor grade, Transene Company, Inc.) for 20 min. After washing with deionized water and drying under a stream of N_2 gas, it was transferred to a glove box under inert atmostphere (N_2). The H-terminated silicon surface was chlorinated PCl_5 (99.998%, Alfa Aesar) in saturated chlorobenzene (99.8%, Sigma-Aldrich) at 90 °C for 45 min. In order to initiate the chlorination, a grain of benzoyl peroxide (reagent grade, 97%, Sigma-Aldrich) was added to the PCl_5/chlorobenzene solution. After serial washing with chlorobenzene and tetrahydrofuran (THF), the wafer was reacted with the desired lithiated organic compound for attachment of phenyl or 3,5-dimethoxyphenyl. For the phenyl-terminated Si(111) surface (*p*-Si(111)|Ph), the Cl-termianted Si(111) wafer was immersed in 0.1 M phenyllithium (PhLi) solution in THF (diluted from 1.8 M PhLi in dibutyl ether, Sigma-Aldrich) at -70 °C, then the solution was allowed to warm to room temperature and stored for 1 h. Because the atop Si atoms cannot be fully covered with the aryl groups, the unreacted Si(111)-Cl sites were methylated using 1 M CH_3MgCl solution (diluted from 3.0 M in THF, Sigma-Aldrich) at 60 °C for 30 min. The wafer was removed from solution, rinsed with THF, sonicated in THF and MeOH for 10 min, dried by a stream of N_2 gas, and finally dried under vacuum. For the 3,5-dimethoxyphenyl-terminated Si(111) surface (*p*-Si(111)|diOMe), a small batch of 0.082 g (0.36 mmol) of 1-bromo-3,5-dimethoxybenzene (97%, Acros) was reacted with 0.2 mL of *n*-butyllithium (*n*BuLi) solution (0.32 mmol, 1.6 M in hexanes, Sigma-Aldrich) in 15 mL THF at -70 °C for 40

min. The Cl-terminated Si(111) wafer was immersed into the lithiated dimethoxybenzene solution at -70 °C, then the solution was allowed to warm to room temperature and stored for 1 h. The unreacted Si(111)-Cl sites were alkylated with methyl groups analogous to the phenyl-terminated Si(111).

4.2.2 Photo-Assisted Electrodeposition of MoS_x

Synthesis of $[MePipH]_2[MoS_4]$

$[MePipH]_2[MoS_4]$ was synthesized by a modification of a published procedure. $[NH_4]_2[MoS_4]$ (7.71 mmol, 99.97%, Sigma-Aldrich) was added to 115 mL distilled H_2O, followed by the addition of *N*-methylpiperidine (15.4 mmol, 99%, Sigma-Aldrich).[38,39] The solution was stirred for 1 hour under an N_2 atmosphere. The reaction was exposed to slight vacuum for 1 min every 5 min for 1 h to remove NH_3. The solution was then filtered, and a volume of 115 mL of ethanol was added to the filtrate, and it was placed in a freezer overnight. The resulting product was collected by filtration (cold), and washed with cold ethanol (ACS grade, Pharmco-Aaper) and diethyl ether (Fisher Scientific). The product consisted of metallic, bright red flakes. Yield: 35%. UV/vis (CH_3CN, λ in nm): 244, 320, 470.

Synthesis of [PipH][TFSI]

[PipH][TFSI] was synthesized by a modification of a published procedure.[40] Piperidine (8.997 mmol, 99%, Sigma-Aldrich) was dissolved in 5.0 mL of distilled H_2O, placed under an N_2 atmosphere, and cooled to ca. 0 °C in an ice bath. Excess of 80 wt% HTFSI(aq) (16.582 mmol, 99%, IoLiTec, Inc.) was diluted with 5 mL of distilled H_2O and added dropwise to the solution over 30 min. The reaction was allowed to warm to room temperature and was left stirring overnight. The product was transferred to a separatory funnel, extracted into 50 mL of CH_2Cl_2 (ACS grade, Fisher Scientific), and

washed three times with 50 mL of CH_2Cl_2. The CH_2Cl_2 was then removed with a rotary evaporator. The product was dried under vacuum at 50 °C for at least 24 h. The product was a clear liquid. Yield 76%.

Photo-Assisted Electrodeposition of MoS_x and Spectroelectrochemistry of $[MePipH]_2[MoS_4]$

The photo-assisted electrodeposition experiments were performed on a CH instruments 440 potentiostat/galvanostat with a homemade glass cup three electrode cell. All experiments were performed using 1-ethyl-3-methylimidazolium bis(triflurormethylsulfonyl)imide (EMIM-TFSI, 99%, IoLiTec, Inc.). EMIM-TFSI was dried in a vacuum oven at 100 °C for a minimum of 24 h prior to use and stored in an argon-filled glovebox. A Cree 100 W white LED bulb (color temperature = 2,700 K) in an aluminum cone was used as the light source. Prior to experiments, the cell was soaked in a Piranha solution for 24 h, followed by neutralization with $NaHCO_3$, boiling in distilled H_2O for 1 h, and drying in an oven at 100 °C overnight. All electrodeposition experiments were performed in a glovebox with an argon atmosphere with an O_2 concentration < 5 ppm and a H_2O concentration < 0.1 ppm. The *p*-Si(111) substrate functionalized with the appropriate organic group was used as the working electrode. Alternatively, glassy carbon (GC, Alfa Aesar) slabs were employed as the working electrode for additional characterization of the films; these electrodes were polished with 0.050 μm alumina slurry on microcloth (Buehler), sonicated in 18.2 MΩ-cm H_2O to remove the residual alumina powder, and dried in an oven at ca. 100 °C for 24 h prior to experiments. The counter electrode in these experiments was a Pt mesh or a graphite rod; graphite was used to avoid the possibility of platinum contaminating the working electrode. The quasi-reference electrode (QRE) was a platinum wire. The electrodes were placed directly in the deposition bath. Platinum was used as the QRE as an alternative to

silver, which has been observed to dissolve in ionic liquids and contaminate electrodes. It should be noted that drift in the potential up to 200 mV in platinum QREs have been observed. The potential in reference to ferrocene could not be determined due to a reaction between ferrocene and the MoS_4^{2-} precursor. The reaction between M^{2+} ions and MoS_4^{2-} has been known to lead to various soluble and insoluble products.[41] Before use the platinum counter and quasi-reference electrode were cleaned by heating in a propane flame, graphite rods were polished with sand paper. After the deposition experiments the working electrode was removed from the glovebox and subsequently washed with ethanol, acetone (ACS grade, Fisher Scientific), and dichloromethane to remove any residual ionic liquid.

UV/vis spectroelectrochemical measurements were performed in a homemade, air-tight Kel-F three electrode cell with a 1 cm path length. Prior to use the cell was soaked in a Piranha solution for 24 h followed by neutralization with $NaHCO_3$, boiling in H_2O for 1 h, and dried under vacuum at ca. 100 °C overnight. The cell was assembled outside the glovebox, brought into the glovebox to add the electrolyte; the cell was sealed and removed from the glovebox to perform experiments. The working electrode was transparent fluorine-doped tin oxide (FTO, Pilkington). The FTO electrodes were cleaned by sequential sonication in acetone, ethanol, and isopropanol for 10 min, heating in 30 v/v% aqueous ethanolamine solution at 80 °C for 10 min, sonication in water for 30 min, drying under N_2 and in an oven at ca. 100 °C overnight. The counter-electrode and quasi-reference electrode were a stainless steel rod and a Pt wire, respectively. The stainless steel electrode was cleaned with sand paper and the Pt wire was cleaned by heating in a propane flame. These electrodes are placed directly in the solution. A diode array UV/vis spectrometer (Agilent 8453) was used to measure several wavelengths during the experiment. Due to noise in the UV/vis spectrum, it was not possible to record absorption

data for wavelengths below 380 nm and between 410–550 nm. During spectroelectrochemical measurements, the shutter remained open to collect measurements at a rate of one per second.

4.2.3 Physical and Electrochemical Characterization of Electrodeposited Films

Hydrophilicity was determined by using a water contact angle measurement of the organic-modified Si(111) samples using a contact angle goniometer (Model 100-00-115, Rame Hart), and by measuring the contact angle values of a 10 µL water droplet. The electrodeposited films were characterized using several techniques. Scanning electron microscopy was performed on a FEI Quanta 650 FEG ESEM. Films were coated with a thin layer of Au/Pd to ensure conductivity of the films. Raman spectroscopy was carried out on a Renishaw inVia microscope with a 514.5 nm Ar laser in the backscattering configuration. The Stoke's Raman signal at 521 cm^{-1} of a bulk Si(110) single crystal was used to calibrate the instrument. The laser was operated at low powers (1%, < 0.5 mW) to prevent photocrystallization or degradation of the MoS_x films. X-ray photoelectron spectra were collected on a Kratos Axis Ultra DLD X-ray photoelectron spectroscopy system and analysed according to the same methods as our previous work.[42] Survey scans were recorded with a 1 eV resolution, followed by high resolution scans (0.1 eV, 2000 ms dwell time) of the carbon 1*s*, oxygen 1*s*, molybdenum 3*d*, and sulfur 2*p*. Semi-quantitative analysis of the XPS spectra was performed with the CasaXPS software (version 2.3.16, Casa Software Ltd.). The high resolution scans were used to compare the relative concentrations of the different species comprising the film. Non-metals, C and O, were fit with linear backgrounds and Mo and S were fit with Shirley backgrounds. The O–C=O peak from adventitious carbon in the C 1*s* spectrum was used to calibrate the binding energy. All fitted curves were the result of the summation of multiple Voight functions with 30% Lorentzian and 70% Gaussian character.

The photoelectrochemical (PEC) properties of surface-modified samples were investigated in a three-electrode configuration, consisting of a Si wafer working electrode, a Pt-wire (99.95%, Strem) counter electrode, and a saturated calomel electrode (CHI150, CH Instruments) as a reference electrode. For the HER performance measurements of the MoS_x substrates (electrodeposited with a graphite rod counter electrode instead of a Pt electrode), a glassy carbon electrode (CHI104, CH Instruments) was used as a counter electrode. A 0.5 M $H_2SO_{4(aq)}$ solution was used as the electrolyte in all PEC-HER measurements. A 150 W Xe lamp (Newport Co.) with an AM-1.5G solar filter (Newport Co.) was used to simulate sunlight at 100 mW cm^{-2}. The light active area was defined as 0.07 cm^2 from the diameter of the O-ring (0.3 cm), and the photocurrent density (mA cm^{-2}) was converted based on the light active area. The detailed experimental set-up, including PEC-cell assembly is available in our previous report. The linear sweep voltammetry (LSV) was performed using a WaveNow (Pine Research Instrumentation) potentiostat between +0.2 V and -1.3 V vs. SCE with a standard scan rate of 100 mV s^{-1}. To convert the measured potential (vs. SCE) to RHE, the following equation was used:

$$E_{RHE} = 0.241\,V + 0.059pH \quad (4)$$

Electrochemical impedance spectroscopy (EIS) measurements were carried out using an Interface 1000 (Gamry Instruments) at various applied potentials between 0 V and -0.4 V vs. SCE under illumination with an AC amplitude of 10 mV over a frequency range of 10^5–0.1 Hz. For the extraction of charge transfer resistance (R_{ct}) from the EIS results, the Randles equivalent circuit was applied using Zview software (version 2.8d, Scribner Associate Inc.).

CHAPTER 4.3 RESULTS AND DISCUSSION

4.3.1 Surface Characterization

Surfaces	Water Contact Angle, θ^{water} (°)	XPS Intensity[a]		Surface Coverage (%)[b]
		C 1*s* (C–Si)	C 1*s* (sp^2)	
p-Si(111)|diOMe	55.4 ± 1.4	0.2073	0.2340	46.80
p-Si(111)|Ph	64.1 ± 2.1	0.1872[c]	0.2753[c]	55.06[c]
p-Si(111)|OH	56.2 ± 1.7[d]			
p-Si(111)|CH_3	110.8 ± 0.8[d]			

Table 4.1: Water Contact Angle and Surface Coverage for Organic-terminated *p*-Si(111) Surfaces. [a]Relative intensity to the Si 2*p* (Si–C bonded). [b]Relative coverage of concerned molecule to the ideal value of 0.5. [c]Value from ref 12. [d]Value from ref 39.

We hypothesized that the higher charge density at the oxygen-containing surface moiety (3,5-dimethoxyphenyl) would afford enhanced electrodeposition performance in ionic liquid media due to improved conductance at the substrate|electrolyte interface. To investigate this hypothesis, we first evaluated the surface hydrophilicities of *p*-Si(111)|Ph and *p*-Si(111)|diOMe susbtrate by measuring the water contact angle (θ^{water}), a common indicator of surface hydrophilicity. As shown in Table 1, the *p*-Si(111)|diOMe surface exhibits a contact angle of 55.4 ± 1.4°, consistent with our previous report.[43] This value is similar to that observed for the super-hydrophilic (100% OH-terminated) substrate (56.2 ± 1.7°), and quite distinct from the super-hydrophobic (100% CH_3-terminated) surface

(110.8 ± 0.8°). This result indicates that the *p*-Si(111)|diOMe surface has a strong hydrophilic nature that is comparable to the super-hydrophilic OH-terminated surface. On the other hand, the hydrocarbon-only substrate *p*-Si(111)|Ph surface shows a modest increase in the contact angle (64.1 ± 2.1°), due to the absence of any oxygen group on the organic moiety. To ensure this observed difference was caused only by the identity of the organic species, their respective surface coverages were evaluated via X-ray photoelectron spectroscopy by the comparison of $I_{C\text{-}1s}/I_{Si\text{-}2p}$ ratio via. The assigned Si 2*p* and C 1*s* spectra for the *p*-Si(111)|diOMe and *p*-Si(111)|Ph are available in Supporting Information (Figure S4.2) and Ref 15, respectively. From the literature,[14] we accepted that the theoretical maximum value of $I_{C\text{-}1s}/I_{Si\text{-}2p}$ for ~100% covered alkyl monolayer (e.g. methyl) is ~0.5. However, the quantification of $I_{C\text{-}Si}/I_{Si\text{-}C}$ (caused by $–CH_3$) portion of the *p*-Si(111)|diOMe substrate is ~0.21, which is roughly half of the theoretical maximum value. The remnant value can be obtained by the sp^2 component derived from the aromatic species. The calculated coverage of sp^2 carbon on *p*-Si(111)|diOMe is ~0.23, which is in agreement with *p*-Si(111)|Ph substrate (~0.28). Moreover, the sum of the surface coverage of *p*-Si(111)|diOMe (44%), quantified by $C_{C\text{-}Si}$ and C_{sp^2}, is consistent with the benchmark value of phenyl coverage reported by established researchers (52%) and our analogous report (45%).[14,44] This result indicates that (*i*) the 3,5-dimethoxyphenyl is effectively bonded on Si atop sites, and (*ii*) the surface coverage is nearly identical to the *p*-Si(111)|Ph substrate. Thus, the hydrophilicity of the surface is likely caused by the H-bonding lone pair on the methoxy groups ($-OCH_3$), and possibly it's enhanced dipole.

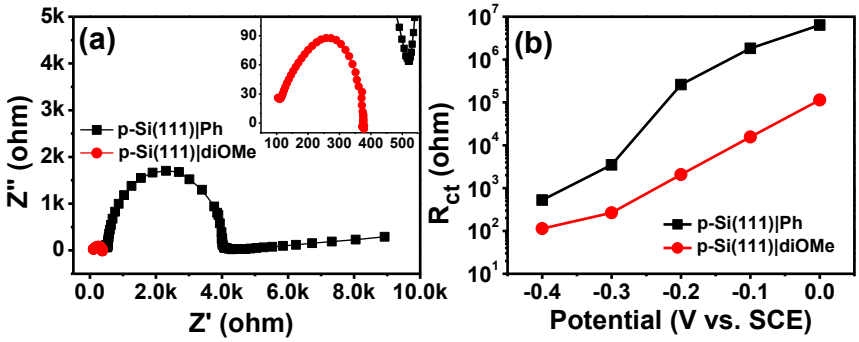

Figure 4.1: (a) Nyquist plots for *p*-Si(111)|Ph (black) and *p*-Si(111)|diOMe (red) substrates. The inset is a magnification of the *p*-Si(111)|diOMe Nyquist plot. (b) Potential dependence of the charge transfer resistance as determined by EIS. Solution 0.5 M H_2SO_4(aq), 1-sun irradiation, 10 mV AC amplitude, frequency range $10^5 < f < 0.1$ Hz.

We next hypothesized that the hydrophilicity and the increased charge density from the oxygen moieties would enhance the charge transfer reaction between the electrode surface and the electrolyte. To test this, electrochemical impedance spectroscopy (EIS) was employed. EIS measurements were performed with a frequency range of 10^5–0.1 Hz under 1-sun irradiation with various applied potentials. The obtained Nyquist plots with -0.3 V vs. SCE for *p*-Si(111)|diOMe and *p*-Si(111)|Ph substrate are shown in Figure 4.1a. The *x*-intercept of high frequency (low *x*-axis) and the diameter of the semicircle correspond to the uncompensated resistance (R_s) and the charge transfer resistance (R_{ct}), respectively. From the fitting with Randle's equivalent circuit [$R(CPE,R)$, R: resistance element, CPE: constant phase element – non-ideal capacitance], the R_{ct} of *p*-Si(111)|Ph is 3.47×10^3 Ω, while that of *p*-Si(111)|diOMe surface is 2.66×10^2 Ω. This remarkable decrease in resistance on the diOMePh surface (~10 fold) of R_{ct} was observed in all experiments (applied potentials between -0.4 and 0 V vs. SCE), as

shown in Figure 4.1b. Furthermore, the same trend of lower R_{ct} of *p*-Si(111)|diOMe than *p*-Si(111)|Ph surface was also found in non-aqueous solution (Figure S4.3 in SI). Lastly, the same experiment on a super-hydrophobic *p*-Si(111)|CH_3 substrate (Figure S4.3c and d, 0.5 M H_2SO_4) afforded a charge transfer resistance of 1.33×10^5 Ω. From these results, it evident that the hydrophilic nature of the surface and the increased charge density resulting from the oxygen moieties accelerates the charge transfer rate at the electrode|electrolyte interface. Therefore, out of the three EIS-tested electrodes, the *p*-Si(111)|diOMe substrate was pursued as the most promising substrate for the photo-assisted electrodeposition of the catalyst.

4.3.2 Photo-Assisted Electrodeposition of MoS_x

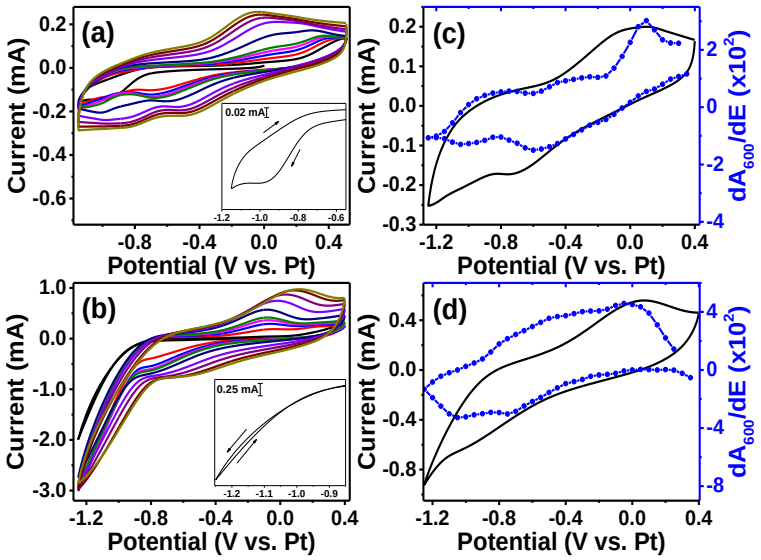

Figure 4.2: CV deposition of MoS_x on glassy carbon electrodes from 0.005 M $[MePipH]_2[MoS_4]$ in EMIM-TFSI in the (a) absence and (b) presence of 0.2 M [PipH][TFSI], scans 1-5, 10, 20, 30, 40, 50. Inset of (a) and (b) show the first scan of the depositions. 25th scan of cyclic voltammogram and corresponding

derivative cyclic voltabsorptogram of 0.005 M $[MePipH]_2[MoS_4]$ on an FTO electrode in the (c) absence and (d) presence of 0.2 M [PipH][TFSI], λ = 600 nm, Scan Rate = 50 mV/s.

The electrochemistry of $[MePipH]_2[MoS_4]$ in EMIM-TFSI was first investigated on glassy carbon electrodes using cyclic voltammetry in the absence (Figure 4.2a) and the presence (Figure 4.2b) of 0.2 M [PipH][TFSI] (a proton donor). In both cases, cycling the $[MoS_4]^{2-}$ precursor between +0.5 and -1.25 V vs. Pt leads to a progressive increase in current and the appearance of new features; this behaviour is similar to others' observations in aqueous electrolyte.[27,28] In the absence of [PipH][TFSI] an anodic peak appears at ca. -0.07 V vs. Pt and two cathodic peaks appear at ca. -0.45 and -0.85 V. In the presence of [PipH][TFSI] an anodic peak appears at ca. +0.1 V vs. Pt and one cathodic feature at ca. -0.55 V. When the potential is scanned negative of -0.8 V vs. Pt a large increase in the current is observed, which is likely in part due to the reduction of protons from [PipH][TFSI]. In the first scan of $[MoS_4]^{2-}$ in the presence of [PipH][TFSI] (inset of Figure 4.2b) a nucleation loop is observed, which is absent from the first scan in only EMIM-TFSI (no proton source). This suggests that cathodic deposition only occurs to a significant extent in the presence of excess protons, which has been found to be the case in other aprotic media.[29]

Two electrochemical reactions have been proposed for the electrodeposition of MoS_x (x = 2 or 3) from the $[MoS_4]^{2-}$ ion.[25,26]

$$[MoS_4]^{2-} + 4H^+ + 2e^- \rightarrow MoS_2 + 2H_2S \quad (1)$$

$$[MoS_4]^{2-} \rightarrow MoS_3 + 1/8\,S_8 + 2e^- \quad (2)$$

Using UV/vis spectroelectrochemistry we further investigated the differences between the absence or presence of excess protons (via [PipH][TFSI]) on the electrodeposition mechanism of $[MePipH]_2[MoS_4]$; FTO was used as a transparent working electrode as a model system to study the details of the electrodeposition mechanism (for eventual application to Si photodeposition). In Figures 4.2c and d the 25th scan of the CV deposition of $[MePipH]_2[MoS_4]$ in the absence and presence of [PipH][TFSI], respectively, is plotted alongside the corresponding derivative cyclic voltabsorptogram (DCVA) at 600 nm. In both cases, cathodic scans result in a decrease in dA_{600}/dE that results in a peak at ca. -0.6 V or -0.75 V vs. Pt, without and with [PipH][TFSI], respectively. This peak corresponds to a decrease in the concentration of the absorbing species at or near the surface of the electrode, which is attributed to corrosion of the film by the back reaction (Eq 2). Vrubel et al. have observed similar results in H_2O using electrochemical quartz crystal microbalance (EQCM).[28] As we scan further a second corrosion peak is observed in the DCVA at ca. -1.05 V vs. Pt for both cases. This peak increases as the cycling continues. Based on the findings by Vrubel at al., we propose the following reaction accounts for our observations:

$$MoS_3 + 2e^- \rightarrow MoS_2 + 1/8\, S_8 \qquad (3)$$

The larger increase in dA_{600}/dE in the presence of [PipH][TFSI] suggests that the reaction is enhanced by protons. The DCVA of the 25th scan is not a great indicator of whether reaction (1) is occurring; the increase in dA_{600}/dE from reaction (1) is drowned out by the decrease in the dA_{600}/dE at these potentials from the corrosion reaction and reaction (3). In the first scan in the absence of [PipH][TFSI] (Figure S4.4a), there is a slight increase

in dA_{600}/dE between -1.0 and -1.25 V vs. Pt, suggesting reaction (1) may occur to some extent due to the limited availability of protons from the two $[MePipH]^+$ counterions of the $[MoS_4]^{2-}$ salt. Alternatively, when an excess of proton source – [PipH][TFSI] – is added, a larger dA_{600}/dE response (Figure S4.4b) is observed between -0.8 and -1.25 V vs. Pt. This supports the claim that protons facilitate reaction (1). As the scan is reversed the dA_{600}/dE signal increases to positive values at approximately -1.0 V vs. Pt in both cases. The continuing anodic scan increases the dA_{600}/dE signal to features at about +0.1 V and -0.05 V vs. Pt without and with [PipH][TFSI], respectively; this corresponds to the peak in the CV. These results show that the concentration of the absorbing species at or near the surface of the electrode is increasing, which we attribute to reaction (2).

The electrodeposition of MoS_x on *p*-Si(111)|diOMe and *p*-Si(111)|Ph was performed in the presence of 0.005 M $[MePipH]_2[MoS_4]$, and 0.2 M [PipH][TFSI] was used to facilitate efficient cathodic deposition of MoS_x. When the silicon substrates were exposed to the LED light source, the open circuit potential increased by ca. +0.15 V vs. Pt (Figure S4.5a and b), which is similar to the observations of Tran et al.[20] Figure 4.3a shows the effect of light on the current produced by $[MoS_4]^{2-}$ at more negative potentials. The dramatic increase in the current when the substrate is illuminated demonstrates that the Si substrate transfers photo-excited electrons from its conduction band to $[MoS_4]^{2-}$. The MoS_x was electrodeposited by a similar CV deposition scheme, where the potential was cycled between +0.1 and -1.25 V vs. Pt under illumination from the LED source. Potentials more positive than +0.1 V vs. Pt were avoided due to the well-known anodic corrosion of Si substrates (Figure S4.5c). Figure 4.3b shows a representative deposition of MoS_x on *p*-Si(111)|diOMe wherein the current increases with each cycle. This is similar to the analogous observations on glassy carbon and FTO substrates. The inset of Figure 4.3b shows the first scan of the MoS_x deposition where a nucleation loop is

present indicating the cathodic deposition of MoS_x. In this potential regime, we expect that the deposition occurs mostly from reaction (1), although it is possible that reaction (2) also occurs, but to a lesser extent. The electrodeposition of MoS_x on *p*-Si(111)|Ph showed qualitatively similar results to *p*-Si(111)|diOMe (Figure S4.5d); however quantitatively the current was higher for the *p*-Si(111)|diOMe substrate, thought to be due to the lower charge transfer resistance observed by EIS.

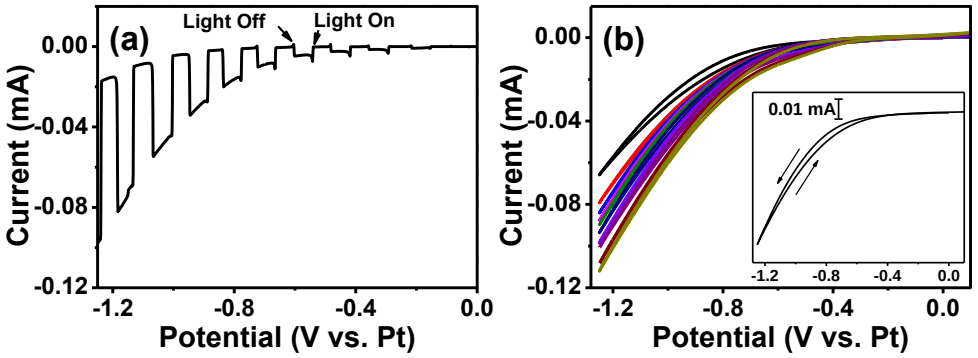

Figure 4.3: (a) First scan of the CV deposition on *p*-Si(111)|diOMe while alternating light on and off. (b) CV deposition of MoS_x on *p*-Si(111)|diOMe, scans 1-5, 10, 20, 30, 40, 50. Inset: First scans of the CV deposition showing the nucleation loop. *Experiment conditions:* 0.005 M $[MePipH]_2[MoS_4]$ + 0.2 M [PipH][TFSI] in EMIM-TFSI, 100 W LED irradiation, scan rate = 50 mV/s.

4.3.3 Characterization of *p*-Si(111)|Org|MoS_x Films

After MoS_x deposition, X-ray photoelectron spectroscopy, Raman spectroscopy and scanning electron microscopy were used to characterize the composition, structure, and morphology of the electrodeposited films on the organic modified *p*-Si substrates. The XPS spectra of the Mo 3*d* region can be fit with two doublets that have Mo $3d_{5/2}$ with binding energies centred at 228.7 and 229.9 eV. The first peak centered at 228.7 eV

is attributed to the Mo(IV) ion of MoS_x, and is in agreement with other reports.[20,27] The second peak at 229.9 eV has been suggested to emanate from a $Mo^{z+}O_yS_x$ species (where $z = 4$ or 5).[28,45,46] The fit of the S 2*p* region (Figure 4.4b) shows two doublets with S $2p_{3/2}$ binding energies centered at 161.5 and 163.0 eV, which correspond to S^{2-} and S_2^{2-}, respectively.[47] Considering the total relative areas of the S 2*p* and Mo 3*d*, the S:Mo ratio is ~2.3:1. Analysis of the Mo 3*d* and S 2*p* XPS spectra of *p*-Si(111)|Ph yields similar results (Figure S4.6c and d). The Raman spectra of *p*-Si(111)|diOMe|MoS_x, *p*-Si(111)|Ph|MoS_x, and GC|MoS_x are presented in the SI Figure S4.7a-c. The spectrum of *p*-Si(111)|diOMe|MoS_x shows two relatively broad bands centered at ~310 cm^{-1} and 430 cm^{-1}. These bands have been observed in Raman studies of amorphous MoS_3, produced by thermal decomposition of $[MoS_4]^{2-}$, which indicates that the electrodeposited films are amorphous.[47–49] However, the E_2 mode of silicon at ~520 cm^{-1} prevents the observation of the disulphide (S–S) stretching mode (510 – 550 cm^{-1}) commonly observed for MoS_3. Relatedly, the Raman spectrum of GC|MoS_x shows a small yet broad band at ~525 cm^{-1}, corresponding to the disulphide stretching mode. The relative intensity of the disulphide Raman band to the other bands is unsurprising considering the XPS results show that the S_2^{2-} ions account for only ~19% of the total sulfur content.

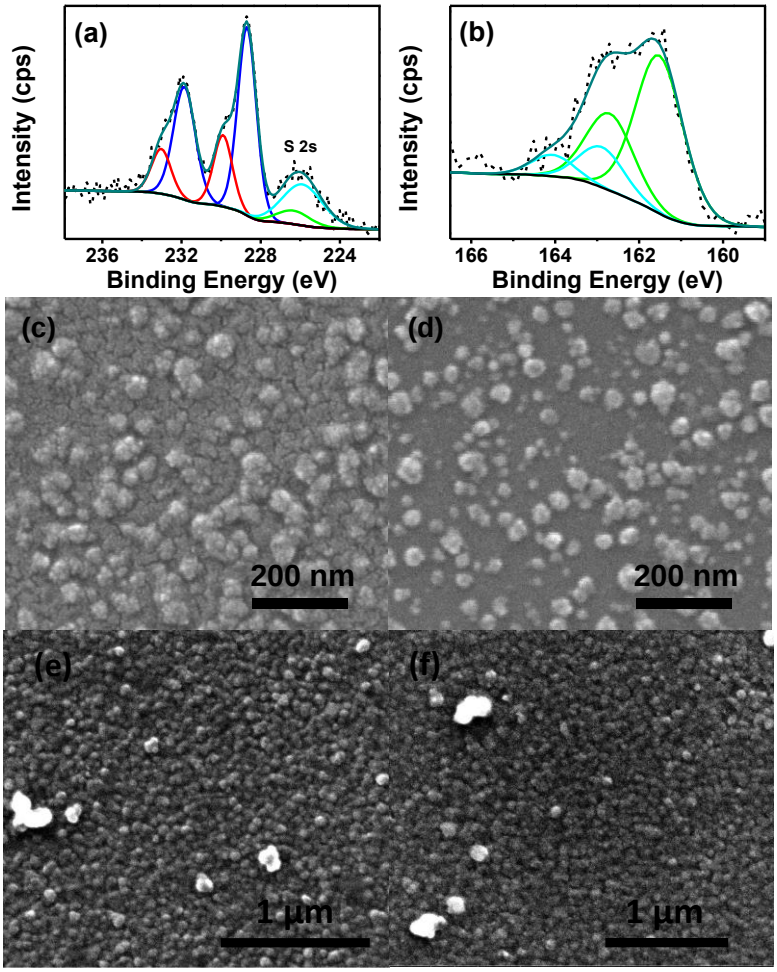

Figure 4.4: X-ray photoelectron spectra of (a) Mo 3*d* and (b) S 2*p* for *p*-Si(111)|diOMe|MoS_x; SEM images for the narrow deposition window (*E* = -0.5 – 0.3 V vs. Pt) for (c) *p*-Si(111)|diOMe|MoS_x and (d) *p*-Si(111)|Ph|MoS_x; SEM images for the full deposition window (E = -1.25 – 0.1 V vs. Pt) for (e) *p*-Si(111)|diOMe|MoS_x and (f) *p*-Si(111)|Ph|MoS_x.

Figure 4.4c,e and d,f depict SEM images of the MoS_x films electrodeposited on *p*-Si(111)|diOMe and *p*-Si(111)|Ph surfaces, respectively. To examine the effects of the organic moieties on the film morphology, a narrow potential window was employed for

electrodeposition (between -0.5 to +0.3 vs. Pt) (Figure 4.4c and d). The SEM images highlight the effect of the dimethoxy group on the surface morphology of the MoS_x film deposits on the organic-terminated *p*-Si substrates. On the 3,5-dimethoxyphenyl-terminated *p*-Si surface, MoS_x forms a continuous film across the surface, whereas the phenyl-terminated *p*-Si surface results in fewer nucleation sites, evidenced by the spacing and varying sizes of the particles. The enhanced MoS_x deposition on the 3,5-dimethoxyphenyl-terminated substrates are thus due to a combination of beneficial properties – primarily the higher charge density at the electrode surface due to the oxygen moieties and lower charge transfer resistance. If the potential window for the electrodeposition is expanded to the potentials used to electrodeposit films for PEC-HER tests (between -1.25 – +0.1 V vs. Pt) (Figure 4.4e and f) then MoS_x appears to form a densely-packed nanoparticle film over the entire surface of the *p*-Si(111)|**R** electrode, regardless of the identity of **R**. Figure S4.8a and b in the supplementary information show atomic force microscopy images of the *p*-Si(111)|diOMe|MoS_x and *p*-Si(111)|Ph|MoS_x, respectively. From these images the root mean square roughness was determined to be 10.0 nm for *p*-Si(111)|diOMe|MoS_x versus 7.4 nm for *p*-Si(111)|Ph|MoS_x, which resulted in roughness factors of 1.010 and 1.005, respectively. In addition, the thicknesses of the MoS_x films were found via AFM to be 59 nm and 29 nm for *p*-Si(111)|diOMe and *p*-Si(111)|Ph, respectively. This difference in thickness of the films is likely attributable to the favourable qualities of the -diOMe surface functionalization.

4.3.4 HER Catalytic Performance

Surfaces	V_{onset} (V)	V_{Jmax} (V)	ΔV (V_{onset} - V_{Jmax}) (V)
p-Si(111)|diOMe	-0.24	-0.61	0.37
p-Si(111)|Ph	-0.29	-0.80	0.51
p-Si(111)|diOMe|MoS_x	+0.14	-0.22	0.36
p-Si(111)|Ph|MoS_x	+0.05	-0.33	0.38

Table 4.2: Photoelectrocatalytic hydrogen evolution figures of merit for *p*-Si(111) surfaces.

The activities of the MoS_x catalyst on *p*-Si(111)|R photoelectrodes were tested for HER performance in 0.5 M H_2SO_4(aq) under 1-sun illumination. Figure 4.5a shows the linear sweep voltammograms *with* and *without* the MoS_x catalyst deposited on the organic functionalized *p*-Si(111) photoelectrodes. As shown in Figure 4.5a, the bare *p*-Si(111)|diOMe photoelectrode shows an onset potential of -0.24 V vs. RHE (V_{onset}, potential at J = -1 mA cm^{-2}), which is more positive than bare *p*-Si(111)|Ph photoelectrode (-0.29 V vs. RHE). Furthermore, ΔV ($V_{\text{onset}} - V_{J\text{max}}$) of *p*-Si(111)|diOMe photoelectrode (373 mV) was significantly smaller compared to *p*-Si(111)|Ph photoelectrode (512 mV), indicating a sharper turn-on to maximum performance. These results agree with our previous results,[12] which showed band edge modulation of *p*-Si(111) modified with various organic functional groups. The diminished ΔV is attributed to a lower resistance to charge transfer across the electrode|electrolyte interface. In the same way, the lower ΔV of *p*-Si(111)|diOMe can be attributed to the greater interaction of the lone pair electrons of the methoxy group with the electrolyte, as opposed to the phenyl case. After introduction of the MoS_x catalyst, the onset potential of diOMe-terminated substrate was positively shifted to +0.14 V vs. RHE; higher than the +0.05

V_{onset} exhibited by the Ph-terminated substrate. This difference is likely due to the band bending caused by the established surface dipole effect caused by the introduction of organic linkers onto the surface of the *p*-Si(111) electrodes.[11,12,50,51] In this work, it was reported that the greatest extent of band bending occurred on the *p*-Si(111)|H electrodes as compared with other surface moieties.

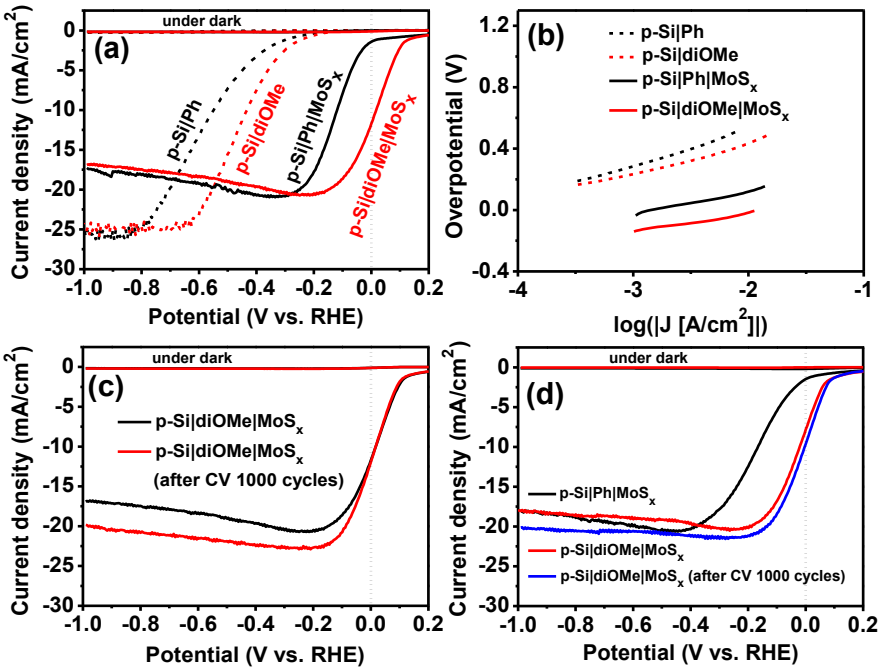

Figure 4.5: (a) *J–E* curves for the hydrogen evolution reaction and (b) Tafel plots for organic-modified *p*-Si(111) substrates *with* and *without* MoS_x catalyst. (c) Comparison of HER activity of *p*-Si(111)|diOMe|MoS_x before and after 1000 CV cycles. (d) Control: Electrodeposited MoS_x in the absence of a platinum counter-electrode, as well as PEC-tested in the absence of a platinum counter-electrode.

To demonstrate the need for organic functionalization of the Si(111) substrate, MoS_x was electrodeposited on a *p*-Si(111)|H surface (prepared by fresh HF etch) and

tested for the PEC-HER (Figure S4.9). On the first scan the onset potential for the H-terminated surface was +0.195 V vs. RHE, more positive than the diMeO-terminated surface, indicating that the surface functionalization plays a crucial role in the photoelectrocatalytic ability of the electrode system. The *p*-Si(111)|H|MoS_x system quickly degrades, and by the 6th scan the onset potential has shifted to +0.05 V vs. RHE, continuing to decrease with each additional scan. This is due to the inability of the susceptible Si–H bonds to protect the surface from hydrolysis and oxidation. To examine the turn-on to maximum performance in the stable diOMe and Ph electrodes, the *J*-*V* curves were converted to Tafel plots as shown in Figure 4.5b. The *p*-Si(111)|diOMe|MoS_x film shows the smallest Tafel slope of 116 mV per decade, which is less than the Tafel slope of *p*-Si(111)|Ph|MoS_x (149 mV per decade).

The stabilities of the films were tested by performing 1000 cycles on the electrode and comparing the 1000th cycle to the 1st. The stability test is shown in Figure 4.5c, which shows that the maximum current (J_{max}) increased, while V_{onset} remained constant. The enhancement in J_{max} can be explained by two processes: (*i*) reaction (3) and (*ii*) the corrosion reaction discussed in the spectroelectrochemical results of MoS_x deposition. Vrubel et al. observed that upon cycling amorphous MoS_3 is converted to MoS_{2+x} (close to MoS_2), which is believed to be the stable, active form of the catalyst.[28] This conversion likely occurs through reaction (3). The corrosion reaction serves to remove elemental sulfur produced from reaction (2) and (3) from the electrode. Sulfur is known to block active sites and/or decrease conductivity, both of which are deleterious to catalytic activity. The corrosion reaction also removes some of the deposited MoS_x catalyst, which could result in a higher surface area and allow more light to reach the silicon substrate. Lastly, due to the well-known complex, $[Pt(MoS_4)_2]^{2-}$,[41] we unambiguously excluded any beneficial effect Pt (from the electrochemical apparatus) could have on both the

electrodeposition and HER activity. Such control experiments were performed by exchanging the Pt counter electrode for a graphite rod or glassy carbon electrode for the electrodeposition and PEC-HER test, respectively. Figure 4.5d shows the resulting *J-V* curves, wherein the V_{onset} of Pt-free *p*-Si(111)|Ph|MoS_x and *p*-Si(111)|diOMe|MoS_x were +0.040 V and +0.125 V vs. RHE, respectively; these values are nearly identical to the original results found of Figure 4.5a.

4.4 CONCLUSION

The synergistic utility of coupling an ionic liquid-based, photo-assisted electrodeposition of MoS_x with organic-functionalized silicon photocathodes for HER has been demonstrated. The lone pair electrons of the 3,5-dimethoxyphenyl surface linker promoted favourable interaction across the electrode|electrolyte interface, resulting in an increase in conductivity. This linker provides enhanced physico-chemical properties for photo-assisted electrodeposition of MoS_x on *p*-Si(111) substrates. The electrodeposition of high-quality MoS_x in ionic liquid avoids issues associated with aqueous depositions, and it is proton-dependent. PEC-HER studies demonstrate that a hydrophilic surface linker on Si(111) – namely, 3,5-dimethoxyphenyl – beneficially modulates the band edge and facilitates the deposition of a continuous MoS_x film. Ultimately, this affords a device with 0.33% efficiency for solar hydrogen production.

4.5 REFERENCES

(1) Oh, I.; Kye, J.; Hwang, S. *Nano Lett.* **2011**, *12*, 298–302.

(2) Goodey, A. P.; Eichfeld, S. M.; Lew, K.-K.; Redwing, J. M.; Mallouk, T. E. *J. Am. Chem. Soc.* **2007**, *129*, 12344–12345.

(3) Boettcher, S. W.; Warren, E. L.; Putnam, M. C.; Santori, E. A.; Turner-Evans, D.; Kelzenberg, M. D.; Walter, M. G.; McKone, J. R.; Brunschwig, B. S.; Atwater, H. A.; Lewis, N. S. *J. Am. Chem. Soc.* **2011**, *133*, 1216–1219.

(4) Dai, P.; Xie, J.; Mayer, M. T.; Yang, X.; Zhan, J.; Wang, D. *Angew. Chem. Int. Ed.* **2013**, *52*, 11119–11123.

(5) Choi, M. J.; Jung, J.-Y.; Park, M.-J.; Song, J.-W.; Lee, J.-H.; Bang, J. H. *J. Mater. Chem.* **2014**, *2*, 2928–2933.

(6) Seger, B.; Pedersen, T.; Laursen, A. B.; Vesborg, P. C. K.; Hansen, O.; Chorkendorff, I. *J. Am. Chem. Soc.* **2013**, *135*, 1057–1064.

(7) Dasgupta, N. P.; Liu, C.; Andrews, S.; Prinz, F. B.; Yang, P. *J. Am. Chem. Soc.* **2013**, *135*, 12932–12935.

(8) McKone, J. R.; Warren, E. L.; Bierman, M. J.; Boettcher, S. W.; Brunschwig, B. S.; Lewis, N. S.; Gray, H. B. *Energy & Environ. Sci.* **2011**, *4*, 3573–3583.

(9) Warren, E. L.; McKone, J. R.; Atwater, H. A.; Gray, H. B.; Lewis, N. S. *Energy & Environ. Sci.* **2012**, *5*, 9653–9661.

(10) Kye, J.; Shin, M.; Lim, B.; Jang, J.-W.; Oh, I.; Hwang, S. *ACS Nano* **2013**, *7*, 6017–6023.

(11) Grimm, R. L.; Bierman, M. J.; O'Leary, L. E.; Strandwitz, N. C.; Brunschwig, B. S.; Lewis, N. S. *J. Phys. Chem. C* **2012**, *116*, 23569–23576.

(12) Seo, J.; Kim, H. J.; Pekarek, R. T.; Rose, M. J. *J. Am. Chem. Soc.* **2015**, *137*, 3173–3176.

(13) Nemanick, E. J.; Hurley, P. T.; Brunschwig, B. S.; Lewis, N. S. *J. Phys. Chem. B* **2006**, *110*, 14800–14808.

(14) Webb, L. J.; Lewis, N. S. *J. Phys. Chem. B* **2003**, *107*, 5404–5412.

(15) Hunger, R.; Jaegermann, W.; Merson, A.; Shapira, Y.; Pettenkofer, C.; Rappich, J. *J. Phys. Chem. B* **2006**, *110*, 15432–15441.

(16) He, T.; Ding, H.; Peor, N.; Lu, M.; Corley, D. A.; Chen, B.; Ofir, Y.; Gao, Y.; Yitzchaik, S.; Tour, J. M. *J. Am. Chem. Soc.* **2008**, *130*, 1699–1710.

(17) Laursen, A. B.; Pedersen, T.; Malacrida, P.; Seger, B.; Hansen, O.; Vesborg, P. C. K.; Chorkendorff, I. *Phys. Chem. Chem. Phys.* **2013**, *15*, 20000–20004.

(18) Seger, B.; Laursen, A. B.; Vesborg, P. C. K.; Pedersen, T.; Hansen, O.; Dahl, S.; Chorkendorff, I. *Angew. Chem.* **2012**, *51*, 9128–9131.

(19) Hou, Y.; Abrams, B. L.; Vesborg, P. C. K.; Björketun, M. E.; Herbst, K.; Bech, L.; Setti, A. M.; Damsgaard, C. D.; Pedersen, T.; Hansen, O.; Rossmeisl, J.; Dahl, S.; Nørskov, J. K.; Chorkendorff, I. *Nat. Mater.* **2011**, *10*, 434–438.

(20) Tran, P. D.; Pramana, S. S.; Kale, V. S.; Nguyen, M.; Chiam, S. Y.; Batabyal, S. K.; Wong, L. H.; Barber, J.; Loo, J. *Chem. Eur. J.* **2012**, *18*, 13994–13999.

(21) Zhang, L.; Liu, C.; Wong, A.; Resasco, J.; Yang, P. *Nano Res.* **2015**, *8*, 281–287.

(22) Ding, Q.; Meng, F.; English, C. R.; Caba?n-Acevedo, M.; Shearer, M. J.; Liang, D.; Daniel, A. S.; Hamers, R. J.; Jin, S. *J. Am. Chem. Soc.* **2014**, *136*, 8504–8507.

(23) Zhang, X.; Meng, F.; Mao, S.; Ding, Q.; Shearer, M. J.; Faber, M. S.; Chen, J.; Hamers, R. J.; Jin, S. *Energy & Environ. Sci.* **2015**, *8*, 862–868.

(24) Ding, Q.; Zhai, J.; Cabán-Acevedo, M.; Shearer, M. J.; Li, L.; Chang, H.-C.; Tsai, M.-L.; Ma, D.; Zhang, X.; Hamers, R. J. *Adv. Mater.* **2015**, *27*, 6511–6518.

(25) Bélanger, D.; Laperriére, G.; Marsan, B. *J. Electroanal. Chem.* **1993**, *347*, 165–183.

(26) Ponomarev, E. A.; Neumann-Spallart, M.; Hodes, G.; Levy-Clement, C. *Thin Solid Films* **1996**, *280*, 86–89.

(27) Merki, D.; Fierro, S.; Vrubel, H.; Hu, X. *Chem. Sci.* **2011**, *2*, 1262–1267.

(28) Vrubel, H.; Hu, X. *ACS Catal.* **2013**, *3*, 2002–2011.

(29) Ponomarev, E. A.; Albu-Yaron, A.; Tenne, R.; Lévy-Clément, C. *J. Electrochem. Soc.* **1997**, *144*, L277–L279.

(30) Albu-Yaron, A.; Levy-Clement, C.; Hutchison, J. L. *Electrochem. Solid-state Lett.* **1999**, *2*, 627–630.

(31) Endres, F.; MacFarlane, D.; Abbott, A. *Electrodeposition from ionic liquids*; John Wiley & Sons, 2008.

(32) Murugesan, S.; Kearns, P.; Stevenson, K. J. *Langmuir* **2012**, *28*, 5513–5517.

(33) Murugesan, S.; Akkineni, A.; Chou, B. P.; Glaz, M. S.; Vanden Bout, D. A.; Stevenson, K. J. *ACS nano* **2013**, *7*, 8199–8205.

(34) Kawamura, Y. L.; Sakka, T.; Ogata, Y. H. *Electrochemistry* **2008**, *76*, 121–124.

(35) Kawamura, Y. L.; Sakka, T.; Ogata, Y. H. *J. Electrochem. Soc.* **2005**, *152*, C701–C705.

(36) Maier, C. U.; Specht, M.; Bilger, G. *Int. J. Hydrog. Energy* **1996**, *21*, 859–864.

(37) Yoshihara, S.; Endo, K.; Sato, E.; Bockris, J. O. ’. M. *J. Electroanal. Chem.* **1994**, *372*, 91–94.

(38) Srinivasan, B. R.; Dhuri, S. N.; Poisot, M.; Näther, C.; Bensch, W. *Z. für Naturforsch. B* **2004**, *59*, 1083–1092.

(39) Siemeling, U.; Bretthauer, F.; Bruhn, C. *Z. für Anorg. und Allg. Chem.* **2006**, *632*, 1027–1032.

(40) Fernicola, A.; Panero, S.; Scrosati, B.; Tamada, M.; Ohno, H. *ChemPhysChem* **2007**, *8*, 1103–1107.

(41) Müller, A.; Diemann, E.; Jostes, R.; Bögge, H. *Angew. Chem. Int. Ed. Engl.* **1981**, *20*, 934–955.

(42) Redman, D. W.; Murugesan, S.; Stevenson, K. J. *Langmuir* **2013**, *30*, 418–425.

(43) Li, F.; Basile, V. M.; Pekarek, R. T.; Rose, M. J. *ACS Appl. Mater. & Interfaces* **2014**, *6*, 20557–20568.

(44) Kim, H. J.; Kearney, K. L.; Le, L. H.; Pekarek, R. T.; Rose, M. J. *ACS Appl. Mater. & Interfaces* **2015**, *7*, 8572–8584.

(45) Benoist, L.; Gonbeau, D.; Pfister-Guillouzo, G.; Schmidt, E.; Meunier, G.; Levasseur, A. *Thin Solid Films* **1995**, *258*, 110–114.

(46) Muijsers, J. C.; Weber, T.; Vanhardeveld, R. M.; Zandbergen, H. W. _.; Niemantsverdriet, J. W. *J. Catal.* **1995**, *157*, 698–705.

(47) Weber, T.; Muijsers, J. C.; Niemantsverdriet, J. W. *J. Phys. Chem.* **1995**, *99*, 9194–9200.

(48) Liang, K. S.; Cramer, S. P.; Johnston, D. C.; Chang, C. H.; Jacobson, A. J.; Chianelli, R. R. *J. Non-Crystalline Solids* **1980**, *42*, 345–356.

(49) Chang, C. H.; Chan, S. S. *J. Catal.* **1981**, *72*, 139–148.

(50) Gleason-Rohrer, D. C.; Brunschwig, B. S.; Lewis, N. S. *J. Phys. Chem. C* **2013**, *117*, 18031–18042.

(51) Hiremath, R. K.; Rabinal, M. K.; Mulimani, B. G.; Khazi, I. M. *Langmuir* **2008**, *24*, 11300–11306.

Chapter 5: Conclusions and Recommendations

5.1 Conclusions

5.1.1 Cathodic Electrodeposition of Amorphous Selenium from an Air- and Water-Stable

A facile method for the electrodeposition of amorphous elemental selenium from diethyl selenite in 1-propyl-1-methylpiperidinium bis(trifluoromethanesulfonyl)imide (PP_{13}-TFSI) using acetonitrile as co-solvent at room temperature and ambient conditions was developed. Ultraviolet – visible spectroelectrochemistry was used to determine that selenium undergoes a step wise reduction from 4^+ to 0 to 2^-. This technique also allowed us to examine characteristics of the deposition at varying times and potential. When the deposition occurred at potentials more negative than the 4^+ to 0 reduction we observed the formation of large particles at and near the surface of the electrode, likely due to the comproportionation reaction between Se^{4+} and Se^{2-} near the electrode surface. Scanning electron microscopy showed these films to be composed of particles at short times and at longer times to coalesce into a more uniform selenium film. X-ray photoelectron spectroscopy confirmed that elemental selenium with minimal oxidation was electrodeposited. X-ray diffraction and Raman spectroscopy showed that the electrodeposited films were amorphous in nature. In addition, *p*-type photoconductivity of the selenium films was observed during the *in-situ* UV-Vis experiments.

5.1.2 Electrodeposition of Amorphous Molybdenum Chalcogenides from Ionic Liquids and their Activity for the Hydrogen Evolution Reaction

A general procedure for the room temperature electrodeposition of amorphous molybdenum chalcogenides was developed using $[MoE_4]^{2-}$ (E = S, Se) ions as single site precursors from 1-ethyl-1-methylimidazolium bis(trifluoromethanesulfonyl)imide. Upon repeated cycling of the $[MoE_4]^{2-}$ ions an increase in current with each subsequent scan

was observed indicating that the area of the electrode was increasing with each scan (i.e. deposition was occurring). UV-Vis spectroelectrochemistry revealed that in the case of both $[MoS_4]^{2-}$ and $[MoSe_4]^{2-}$ both underwent an anodic deposition and a cathodic corrosion reaction. Scanning electron microscopy revealed that we had made conformal films of densely packed nanoparticles. X-ray photoelectron spectroscopy revealed that the films consisted of MoS_z and $MoSe_z$ (where $x = 2 - 3$), which is in agreement with what others have observed for $[MoS_4]^{2-}$ in aqueous environments. Raman spectroscopy showed broad peaks that correspond to the amorphous nature of the films. Both films showed high activity for the hydrogen evolution reaction. MoS_x reached 1 mA/cm^2 at -0.208 V vs. RHE and $MoSe_x$ reached 1 mA/cm^2 at -0.230 V vs. RHE. In addition, the reported Tafel slopes of the two films (MoS_x 42 mV/decade and $MoSe_x$ 59 mV/decade) were on par or lower than previously reported values, further confirming the activity of the catalyst films.

5.1.3 Photo-assisted Electrodeposition of MoS_x from Ionic Liquid on Organic-Functionalized Silicon Photoelectrodes for H_2 Generation

MoS_x films were successfully electrodeposited from 1-ethyl-3-methylimidazolium bis(trifluoromethanesulfonyl)imide onto organic-functionalized *p*-Si(111) photocathodes for the efficient generation of H_2. Two organic modifications were investigated phenyl- and dimethoxyphenyl-groups. The dimethoxyphenyl-groups showed high hydrophilicity and increased charge transfer incomparison to their phenyl counterparts. This is thought to be due to the increased charge density from the lone pairs of the oxygen moieties. For this reason the photo-assisted electrodeposition of MoS_x was investigated on these substrates. Due to limitations of *p*-Si(111) the electrodeposition procedure was adapted to include protons, which showed the cathodic deposition of MoS_x on the electrodes. UV-Vis spectroelectrochemistry revealed a small indication of cathodic deposition in the

presence of protons. Additionally, the anodic deposition and cathodic corrosion reaction were also observed with this technique. Scanning electron microscopy and atomic force microscopy showed that the dimethoxyphenyl coated *p*-Si(111) substrates were ideal for deposition creating densely packed nanoparticle films that exhibited low roughness. X-ray photoelectron spectroscopy showed the deposition of MoS_x (x = 2 – 3). Photoelectrocatalytic studies revealed the high activity of the *p*-Si(111)|diOMe|MoS_x electrodes for the hydrogen evolution reaction. The onset potential was +0.14 V vs RHE (only 60 mV more negative than platinum in the same system) and ΔV (V_{onset} - V_{max}) of 0.36 V. This activity is attributed to the established band bending caused by the change in the surface dipole from the introduction of the dimethoxyphenyl surface linkers. The electrode was also found to improve with continued cycling. This was attributed to an activation of the catalyst $MoS_x \rightarrow MoS_2$ and the corrosion reaction, removing sulfur from active sites.

5.2 RECOMMENDATIONS

5.2.1 Single-Site Precursors

Single-site precursors for electrodeposition are a great tool to electrodeposit new and exotic materials that are either difficult or impossible to deposit with current methods. The identification of single-site precursors is essential to moving this area of research forward, as well as, new methods to develop single-site precursors. Herein, we describe two potential areas of interest for the continued research of single-site precursors.

The first area would be to expand on the work done in Chapter 3 to investigate whether other tetrachalcogenometallates exhibit similar electrochemical behavior to the tetrathiomolybdate and tetraselenomolybdate. In the past many of the tetrathio- and

tetraselenometallates have been synthesized and studied in depth,[1] and there is preliminary evidence to suggest that this generalized deposition method described in Chapter 3 may apply to the entire class of tetrachalcogenometallate compounds. Figure 5.1 demonstrates that it is possible to electrodeposit WS_x and ReS_x films from EMIM-TFSI using $[WS_4]^{2-}$ and $[ReS_4]^-$, respectively. So the procedure established in chapter 3 is in fact more general than just the molybdenum species. The electrodeposition of WS_z requires higher temperatures (more thermal energy) than their molybdenum counterparts due to the stronger bonds between the tungsten and sulfur. While rhenium can be electrodeposited at room temperature in its current state is not very soluble in EMIM-TFSI. In the past we have experimented with the identity of the cation coordinating the tetrathiomolybdate and have found that the identity of the cation can play a large role in the solubility in an ionic liquid. Changing the cation to something similar to the ionic liquid (imidazolium, pyrrolidinium, piperidinium, tetraphenylphosphonium, etc…) increases the solubility of the metal chalcogen precursor. This work opens the door to a host of other transition metal chalcogenides (VS_x, TaS_x, FeS_x, RhS_x, etc…) that may have interesting properties.

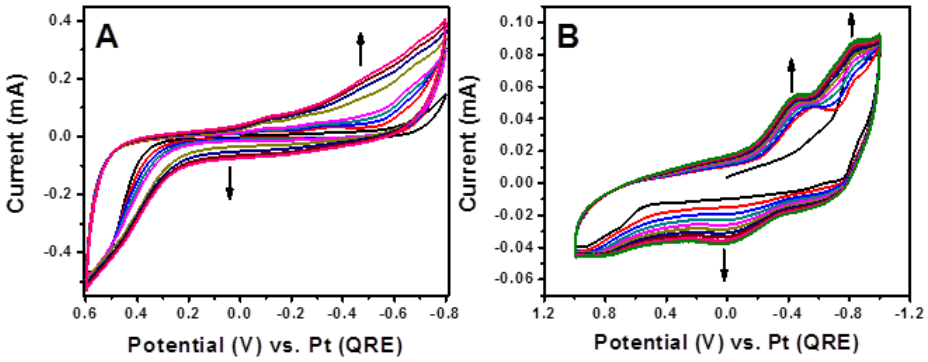

Figure 5.1: (a) CV deposition of WS_x using 0.01 M $[WS_4]^{2-}$ from EMIM-TFSI. Temperature = 100 °C, scan rate = 50 mV/s, scans 1-5, 10, 15, 20, 25. (b) CV deposition of ReS_x using saturated (< 10 mM) $[ReS_4]^-$ from EMIM-TFSI. Temperature = 25 °C, scan rate = 50 mV/s, scans 1-10. Working electrode = glassy carbon.

The second area of interest is research of metal cation-based ionic liquids, where the ionic liquid consists of a metal ion coordinated by neutral ligands with a common ionic liquid anion (e.g. TFSI), to balance the charge. Some research has been done in this synthesis of metal cation-based ionic liquids of Cu, Ag, Fe, Mn, and Zn.[2–6] Metal cation-based ionic liquids are simple to prepare and contain very high concentrations of the metals ions of interest (> 2 M), mitigating common mass transport and solubility problems of metals in ionic liquids.[2,3] Additionly, the cathodic breakdown of the ionic liquid results in the electrodeposition of the desired metal. High current densities can be achieved in these ionic liquids resulting in very fast depositions (e.g. theoretical thickness of 1 μm deposited in 5 seconds).[2] While this approach is currently only being used for metals it may be possible to expand to more complicated compounds.

5.3 REFERENCES

(1) Müller, A.; Diemann, E.; Jostes, R.; Bögge, H. *Angew. Chem. Int. Ed. Engl.* **1981**, *20*, 934–955.

(2) Brooks, N. R.; Schaltin, S.; Hecke, K. V.; Meervelt, L. V.; Binnemans, K.; Fransaer, J. *Chem. - Eur. J.* **2011**, *17*, 5054–5059.

(3) Schaltin, S.; Brooks, N. R.; Stappers, L.; Hecke, K. V.; Meervelt, L. V.; Binnemans, K.; Fransaer, J. *Phys. Chem. Chem. Phys.* **2012**, *14*, 1706–1715.

(4) Sniekers, J.; Brooks, N. R.; Schaltin, S.; Meervelt, L. V.; Fransaer, J.; Binnemans, K. *Dalton Trans.* **2014**, *43*, 1589–1598.

(5) Pratt III, H. D.; Rose, A. J.; Staiger, C. L.; Ingersoll, D.; Anderson, T. M. *Dalton Trans.* **2011**, *40*, 11396.

(6) Anderson, T. M.; Ingersoll, D.; Rose, A. J.; Staiger, C. L.; Leonard, J. C. *Dalton Trans.* **2010**, *39*, 8609.

Appendix

A2 Cathodic Electrodeposition of Amorphous Elemental Selenium from an Air- and Water-Stable

A2.1 Supporting Figures

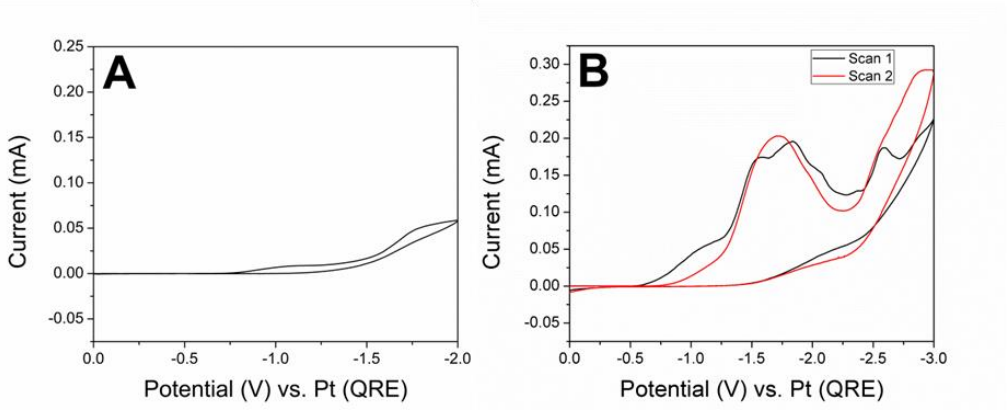

Figure A2.1: (A) Cyclic voltammogram of FTO electrode immersed in 0.6 M CH_3CN in $[PP_{13}][TFSI]$. (B) Scan 1 (Black) and scan 2 (Red) of the cyclic voltammogram of a FTO electrode immersed in 0.1 M $(CH_3CH_2O)_2Se{=}O$ in $[PP_{13}][TFSI]$/12 mol eq. CH_3CN. Scan rate = 10 mV/s.

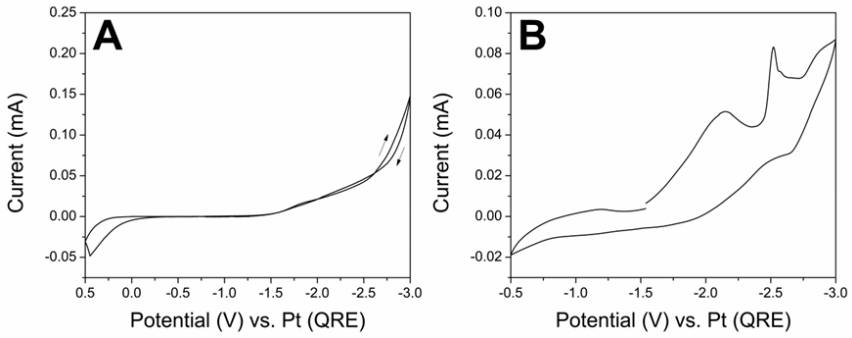

Figure A2.2: (A) Cyclic voltammogram of FTO electrode immersed in $[PP_{13}][TFSI]$. (B) Cyclic voltammogram of Sn disk electrode immersed in 0.1 M $(CH_3CH_2O)_2Se{=}O$ in $[PP_{13}][TFSI]$/6 mol eq. CH_3CN. Scan rate = 10 mV/s.

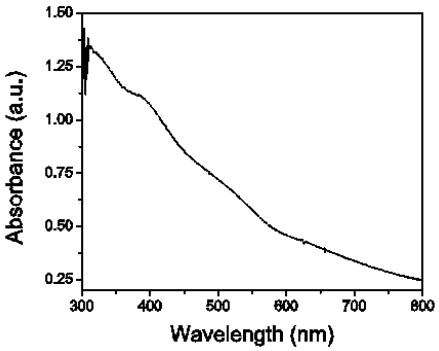

Figure A2.3: UV-Vis absorbance spectra of washed and dried a-Se film deposited at E = -1.7 V for 30 min.

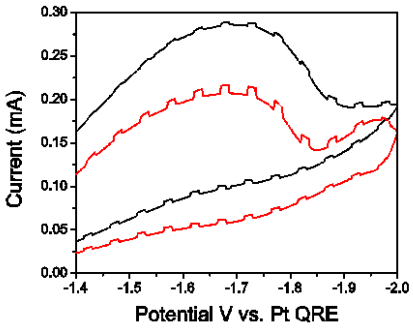

Figure A2.4: Cyclic voltammogram exemplifying the photocurrent generated during UV-Vis measurements. The CV is of the first (black curve) and second (red curve) scan of a FTO electrode immersed in 0.1 M $(CH_3CH_2O)_2Se{=}O$ in $[PP_{13}][TFSI]$/6 mol eq. CH_3CN. Scan rate = 10 mV/s.

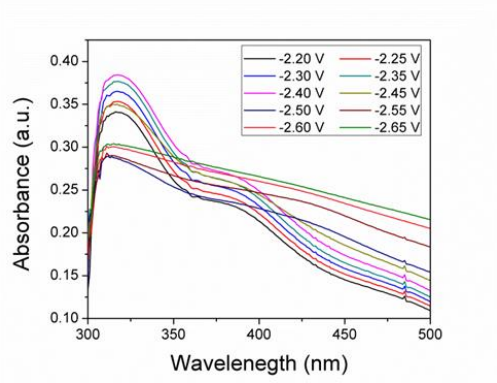

Figure A2.5: Absorbance spectra recorded during the cyclic voltabsorptometry experiments shown in Fig 2A and B. Absorbance spectra between -2.20 V and -2.65 V for the first scan of the cyclic voltabsorptometry experiments of FTO immersed in 0.1 M $(CH_3CH_2O)_2Se{=}O$ in $[PP_{13}][TFSI]$/6 mol eq. CH_3CN are shown. Scan rate = 10 mV/s.

Fig S2.5 shows how the absorbance spectra recorded during the cyclic voltabsorptometry experiments changes between -2.20 V and -2.65 V. From the figure we see that between -2.40 and -2.50 V there is a considerable decrease in the absorbance intensity at 350 nm, which is believed to be due to the cathodic stripping of Se^0 adsorbed on the electrode. From -2.50 V to -2.65 V the absorbance begins to increase again. The absorbance feature that grows in is identical to the feature that grows in during the deposition at -2.5 V, which as explained later in the paper is thought to be due to the increase in Se particle size and the formation of colloidal selenium near the electrode surface by the comproportionation reaction between $(CH_3CH_2O)_2Se{=}O$ and Se^{2-}. The sharp increase in dA_{350}/dE between -2.50 V and -2.55 V is due to the increase in particle size and the formation of colloidal selenium near the electrode surface.

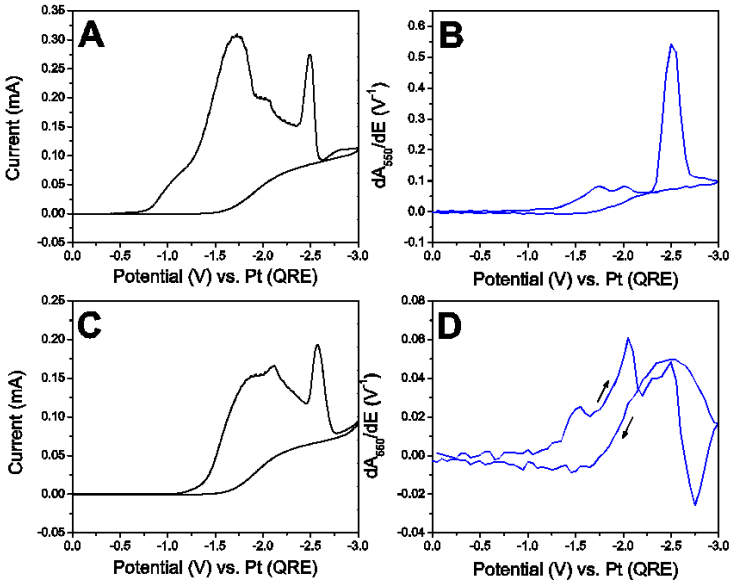

Figure A2.6: First scan of (A) cyclic voltammogram and (B) derivative cyclic voltabsorptogram for a FTO electrode immersed in 0.1 M $(CH_3CH_2O)_2Se{=}O$ in $[PP_{13}][TFSI]$/6 mol eq. CH_3CN. (C) CV and (D) DCVA of the second scan. Scan rate = 10 mV/s and λ=550 nm.

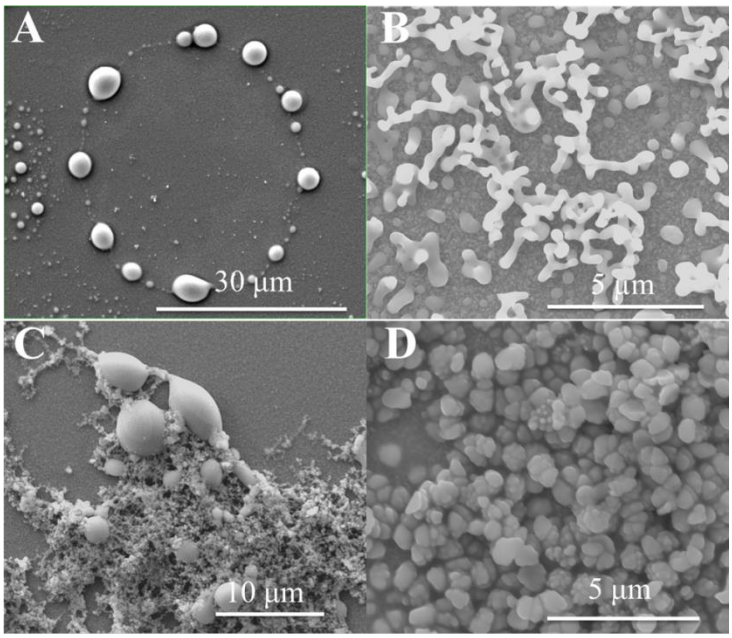

Figure A2.7: Representative SEM images of selenium deposits obtained at a FTO electrode immersed in 0.1 M $(CH_3CH_2O)_2Se{=}O$ in $[PP_{13}][TFSI]$/6 mol eq. CH_3CN at potentials of (A,B) -2.0 V and (C,D) -2.5 V for 30 minutes.

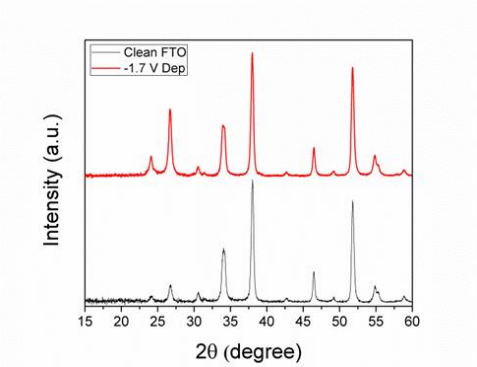

Figure A2.8: Glancing angle X-ray diffraction pattern of a clean FTO substrate (black) and Se electrodeposited on FTO at -1.7 V for 1 hour from 0.1 M $(CH_3CH_2O)_2Se{=}O$ in $[PP_{13}][TFSI]$/6 mol eq. CH_3CN solution (red).

A3 Cathodic Electrodeposition of Amorphous Elemental Selenium from an Air- and Water-Stable

A 3.1 Supporting Figures

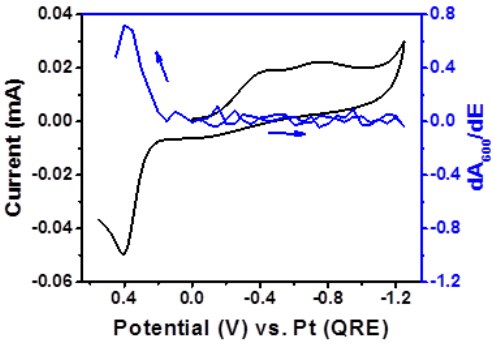

Figure A3.1: First scan of the cyclic voltammogram and corresponding derivative cyclic voltabsorptogram for 0.002 M $[Ph_4P]_2[MoS_4]$ in EMIM-TFSI.

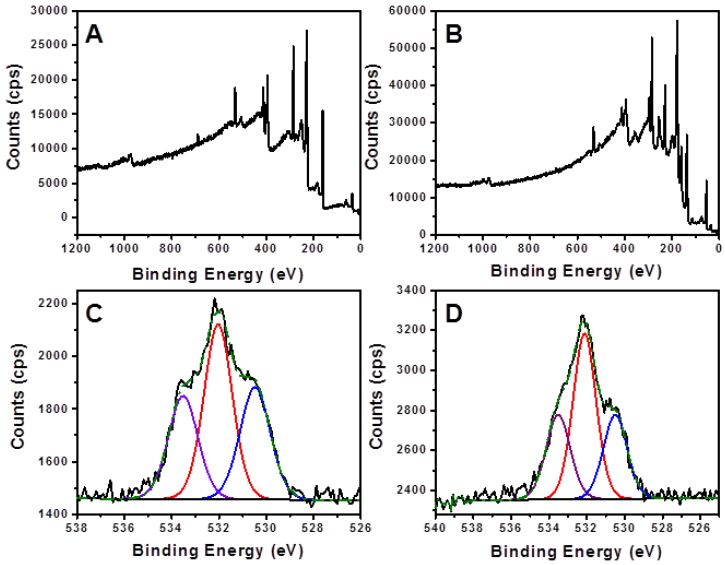

Figure A3.2: Survey spectra of the (a) MoS_x film and (b) $MoSe_x$ film deposited on a glassy carbon electrode. O 1*s* spectra of the (c) MoS_x film and (d) $MoSe_x$ film.

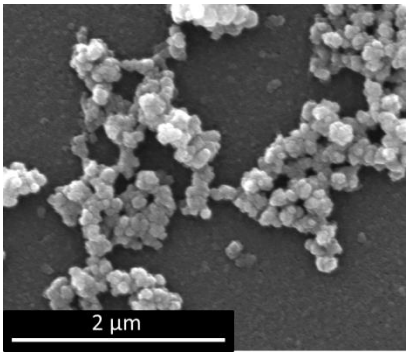

Figure A3.3: Representative SEM of clusters of particles on the surface of the CV deposited MoS_x films.

A4 Cathodic Electrodeposition of Amorphous Elemental Selenium from an Air- and Water-Stable

A 4.1 Supporting Figures

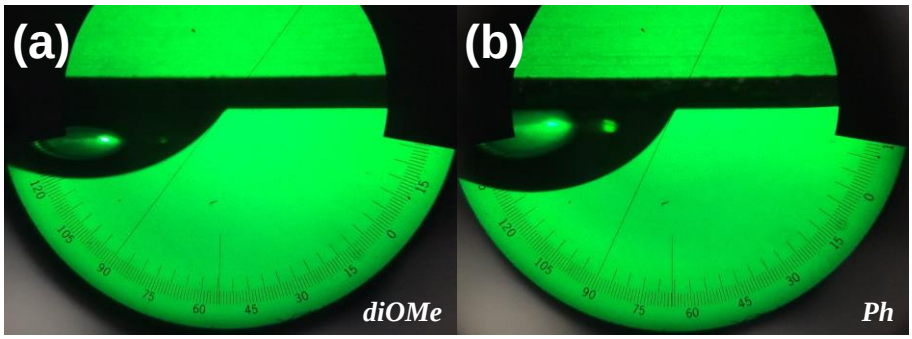

Figure A4.1: Water contact angle of (a) *p*-Si(111)|diOMe and (b) *p*-Si(111)|Ph surfaces with a 10 μL water drop.

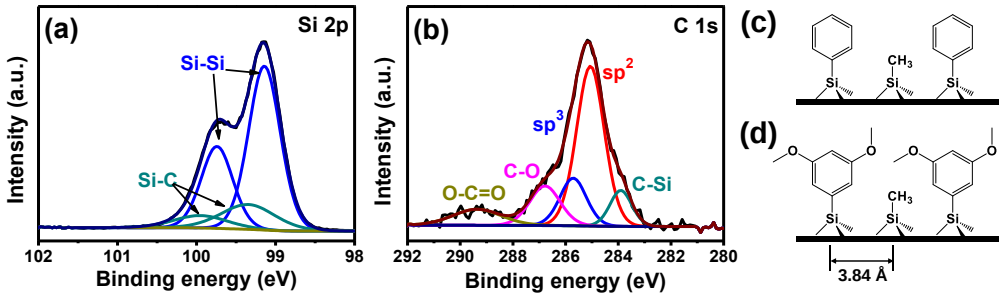

Figure A4.2: X-ray photoelectron spectrum of (a) Si 2*p* and (b) C 1*s* for *p*-Si(111)|diOMe surface, and depiction of organic molecules attached to Si(111) for (c) *p*-Si(111)|Ph and (d) *p*-Si(111)|diOMe

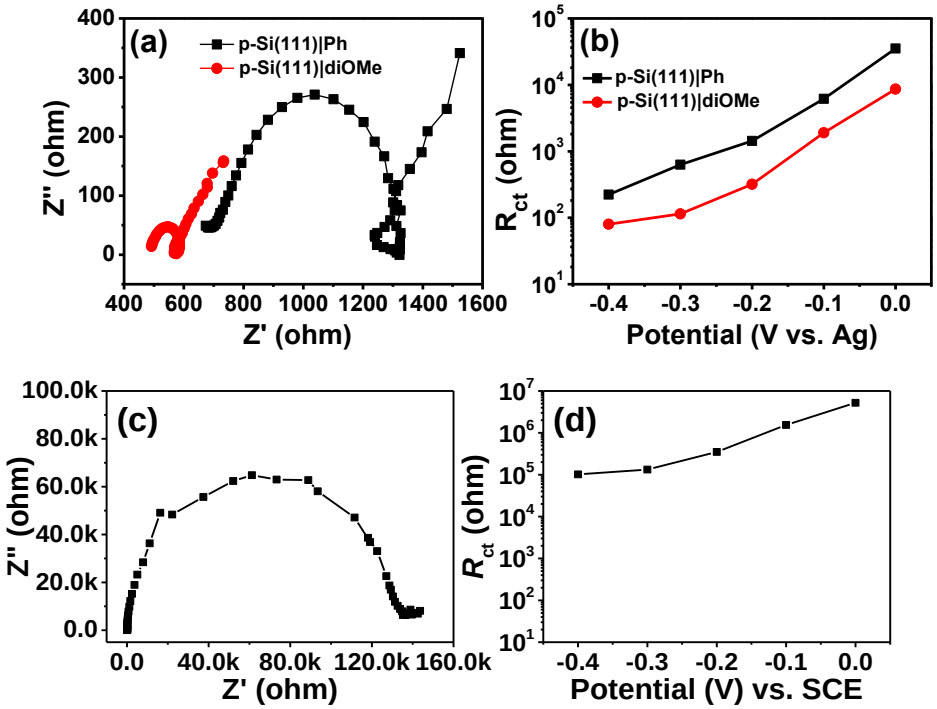

Figure A4.3: (a) Nyquist plots for *p*-Si(111)|Ph (black) and *p*-Si(111)|diOMe (red) surfaces. (b) Representation of the different resistances determined by EIS and plotted versus the applied potential. Conditions: Ag-wire reference electrode, 5 mM ethyl viologen in 0.1 M $LiClO_4$/MeCN, 1-sun irradiation, 10 mV AC amplitude, $10^5 < f < 0.1$ Hz. (c) Nyquist Plot for *p*-Si(111)|CH_3 at E = -0.3 V vs. SCE. (d) Potential dependence of charge transfer resistance of *p*-Si(111)|CH_3 as determined by EIS. Conditions: 0.5 M H_2SO_4, 1-sun irradiation, 10 mV AC amplitude, frequency range $10^5 < f < 0.1$ Hz.

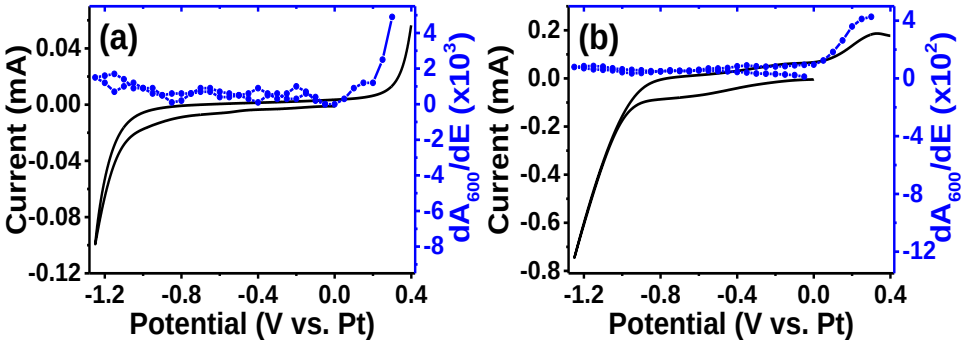

Figure A4.4: First scan of cyclic voltammogram and derivative cyclic voltabsorptometry of 0.005 M $[MePipH]_2[MoS_4]$ in the (a) absence and (b) presence of 0.2 M [PipH][TFSI], λ = 600 nm, scan rate = 50 mV/s.

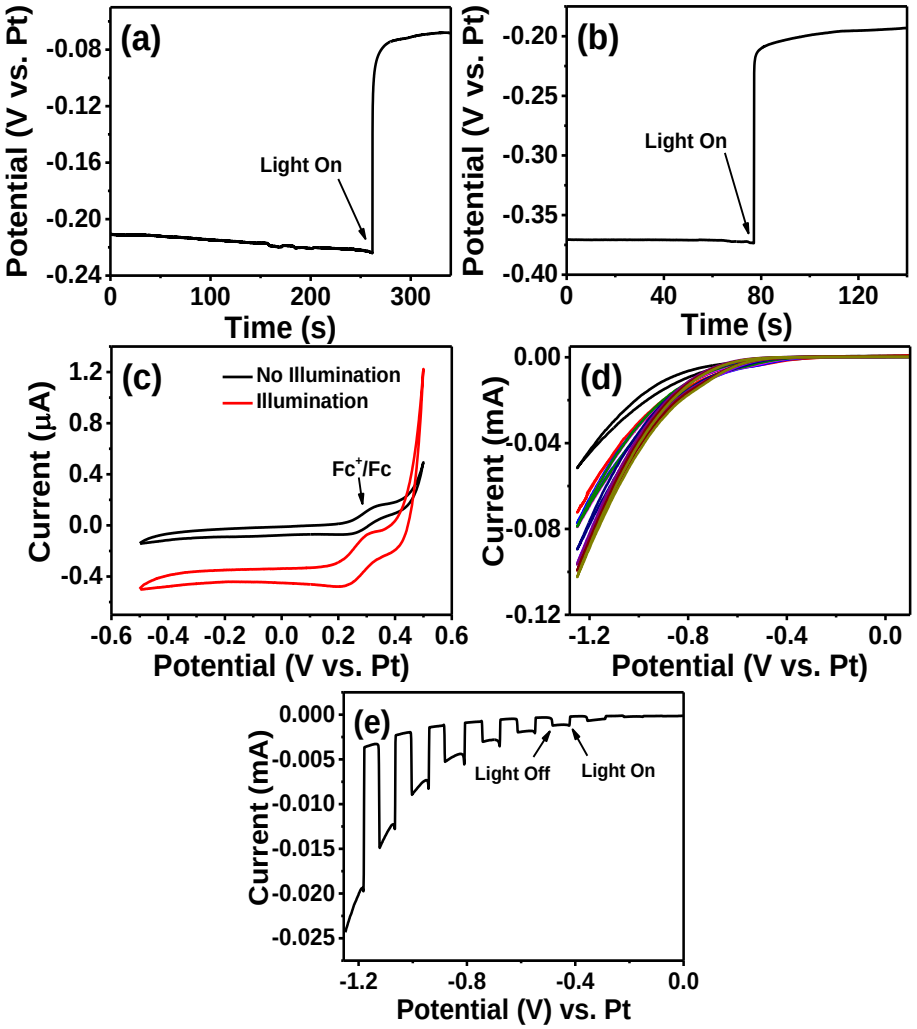

Figure A4.5: Effect of LED light on the open circuit potential of (a) *p*-Si|diOMe and (b) *p*-Si(111)|Ph with 0.005 M $[MePipH]_2[MoS_4]$ and 0.2 M [PipH][TFSI] in EMIM-TFSI. (c) Cyclic voltammogram depicting anodic stability of bare *p*-Si(111) in 0.002 M ferrocene in EMIM-TFSI. (d) CV deposition of MoS_x on *p*-Si(111)|Ph and (e) first scan of the CV deposition on *p*-Si(111)|Ph turning the light on and off with 0.005 M $[MePipH]_2[MoS_4]$ and 0.2 M [PipH][TFSI] in EMIM-TFSI, scans 1-5, 10, 20, 30, 40, 50. Scan rate = 50 mV/s.

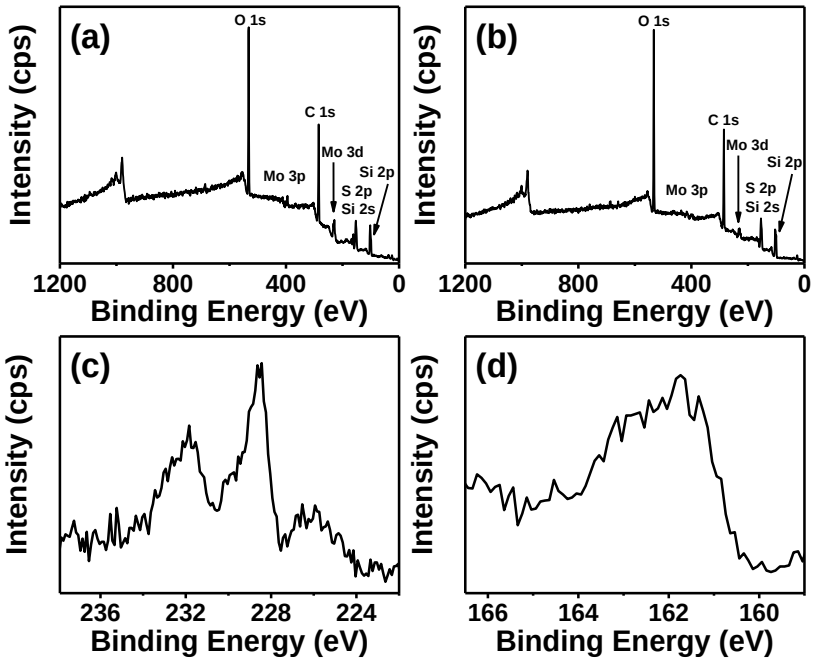

Figure A4.6: XPS survey spectra of (a) *p*-Si(111)|diOMe|MoS_x and (b) *p*-Si(111)|Ph|MoS_x. High resolution XPS spectrum of (c) Mo 3*d* and (d) S 2*p* regions of *p*-Si(111)|Ph|MoS_x.

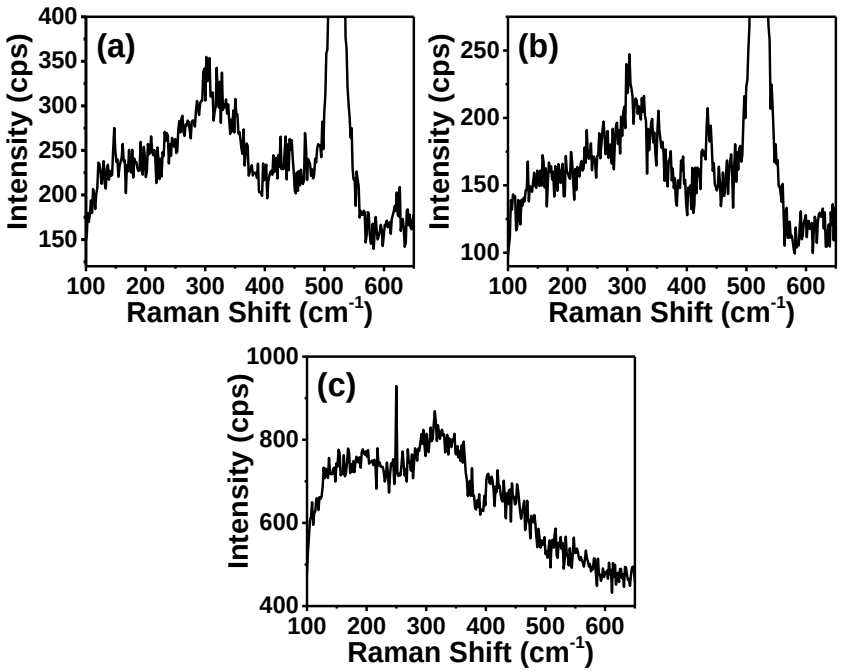

Figure A4.7: Raman spectra of (a) *p*-Si(111)|diOMe|MoS_x, (b) *p*-Si(111)|Ph|MoS_x, and (c) GC|MoS_x.

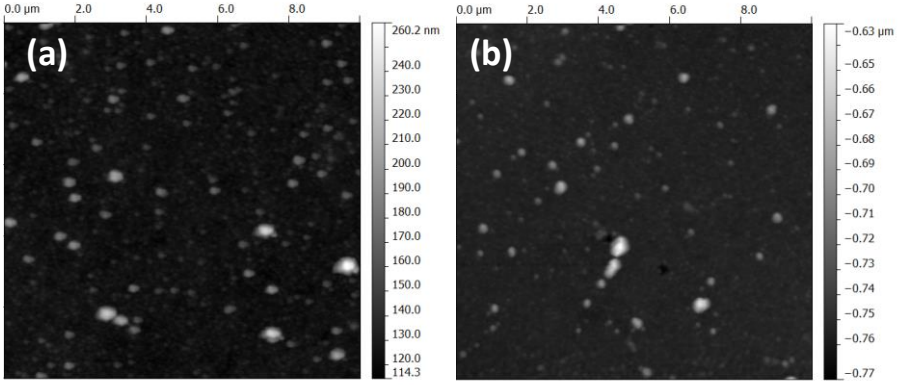

Figure A4.8: Atomic force microscopy height retraces of (a) *p*-Si(111)|diOMe|MoS_x and (b) *p*-Si(111)|Ph|MoS_x.

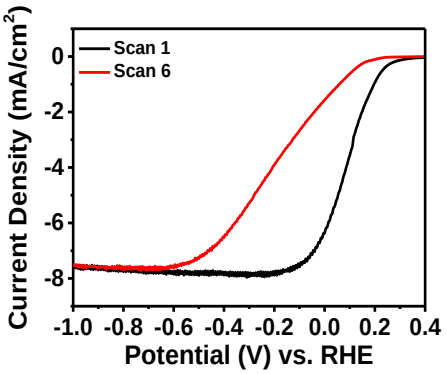

Figure A4.9: PEC-HER test of *p*-Si(111)|H|MoS_x in 0.5 M H_2SO_4, 1-sun irradiation, scan rate = 100 mV/s.

References

The references are ordered in alphabetical order by the last name of the first author on the paper

(1) Aal, A. A.; Voigts, F.; Chakarov, D.; Endres, F. *Electrochimica Acta* **2012**, *59*, 228-236.

(2) Aal, A. A.; Voigts, F.; Chakarov, D.; Endres, F. *J. Solid State Electrochem*. **2012**, *16*, 3027-3036.

(3) Abedin, S. Z. E.; Moustafa, E. M.; Hempelmann, R.; Natter, H.; Endres, F. *ChemPhysChem* **2006**, *7*, 1535-1543.

Abo-Hamad, A.; AlSaadi, M. A.; Hayyan, M.; Juneidi, I.; Hashim, M. A. *Electrochimica Acta* **2016**, *193*, 321-343.

(4) Albu-Yaron, A.; Levy-Clement, C.; Hutchison, J. L. *Electrochem. Solid-state Lett*. **1999**, *2*, 627-630.

(5) Anderson, P,C.; Romankiw, L.T. *Advances in Electrochemical Science and Engineering*, VCH New York, **1994**, *Vol. 3*.

(6) Anderson, T. M.; Ingersoll, D.; Rose, A. J.; Staiger, C. L.; Leonard, J. C. *Dalton Trans*. **2010**, *39*, 8609.

(7) Atkin, R.; El Abedin, S. Z.; Hayes, R.; Gasparotto, L. H.; Borisenko, N.; Endres, F. *J. Phys. Chem. C* **2009**, *113*, 13266-13272.

(8) Bakkar, A.; Neubert, V. *Electrochimica Acta* **2013**, *103*, 211-218.

(9) Bancroft, E. E.; Sidwell, J. S.; Blount, H. N. *Anal. Chem*. **1981**, *53*, 1390-1394.

(10) Bard, A. J.; Faulkner, L. R.; Leddy, J.; Zoski, C. G. *Electrochemical methods: fundamentals and applications*; Wiley New York, **1980**; *Vol. 2*.

(11) Barisci, J. *Electrochem. Commun*. **2004**, *6*, 22-27.

(12) Bélanger, D.; Laperriére, G.; Marsan, B. *J. Electroanal. Chem*. **1993**, *347*, 165-183.

(13) Benck, J. D.; Chen, Z.; Kuritzky, L. Y.; Forman, A. J.; Jaramillo, T. F. *ACS Catal*. **2012**, *2*, 1916-1923.

(14) Benoist, L.; Gonbeau, D.; Pfister-Guillouzo, G.; Schmidt, E.; Meunier, G.; Levasseur, A. *Thin Solid Films* **1995**, *258*, 110-114.

(15) Bindu, K.; Lakshmi, M.; Bini, S.; Kartha, C. S.; Vijayakumar, K. P.; Abe, T.; Kashiwaba, Y. *Semicond. Sci. Technol*. **2002**, 17.

(16) Boettcher, S. W.; Warren, E. L.; Putnam, M. C.; Santori, E. A.; Turner-Evans, D.; Kelzenberg, M. D.; Walter, M. G.; McKone, J. R.; Brunschwig, B. S.; Atwater, H. A.; Lewis, N. S. *J. Am. Chem. Soc*. **2011**, *133*, 1216-1219.

(17) Bonde, J.; Moses, P. G.; Jaramillo, T. F.; Nørskov, J. K.; Chorkendorff, I. *Faraday Discuss*. **2009**, *140*, 219-231.

(18) Bonhôte, P.; Dias, A.-P.; Papageorgiou, N.; Kalyanasundaram, K.; Grätzel, M. *Inorg. Chem*. **1996**, *35*, 1168-1178.

(19) Borisenko, N.; Ispas, A.; Zschippang, E.; Liu, Q.; Abedin, S. Z. E.; Bund, A.; Endres, F. *Electrochimica Acta* **2009**, *54*, 1519-1528.

(20) Boscher, N. D.; Carmalt, C. J.; Palgrave, R. G.; Gil-Tomas, J. J.; Parkin, I. P. *Chem. Vap. Depos*. **2006**, *12*, 692-698.

(21) Bougouma, M.; Van Elewyck, A.; Steichen, M.; Buess-Herman, C.; Doneux, T. *J. Solid State Electrochem*. **2013**, *17*, 527-536.

(22) Brenner, A. *Electrodeposition of Alloys: PRINCIPLES and PRACTICE*; Academic Press, **1963**.

(23) Brooks, N. R.; Schaltin, S.; Hecke, K. V.; Meervelt, L. V.; Binnemans, K.; Fransaer, *J. Chem. - Eur. J*. **2011**, *17*, 5054-5059.

(24) Bubalo, M. C.; Vidovi, S.; Redovnikovi, I. R.; Joki, S. *J. Chem. Technol. Biotechnol*. **2015**, *90*, 1631-1639.

(25) Cabral, M. F.; Pedrosa, V. A.; Machado, S. A. S. *Electrochimica Acta* **2010**, *55*, 1184-1192.

(26) Chang, C. H.; Chan, S. S. *J. Catal*. **1981**, *72*, 139-148.

(27) Chang, K.; Chen, W. *ACS Nano* **2011**, *5*, 4720-4728.

(28) Chastain, J.; King, R. C.; Moulder, J. F. *Handbook of X-ray photoelectron spectroscopy: a reference book of standard spectra for identification and interpretation of XPS data*; Physical Electronics Eden Prairie, MN, **1995**.

(29) Chhowalla, M.; Shin, H. S.; Eda, G.; Li, L.-J.; Loh, K. P.; Zhang, H. *Nat. Chem*. **2013**, *5*, 263-275.

(30) Choi, M. J.; Jung, J.-Y.; Park, M.-J.; Song, J.-W.; Lee, J.-H.; Bang, J. H. *J. Mater. Chem*. **2014**, *2*, 2928-2933.

(31) Chou, L.-H.; Sun, I.-W.; Hussey, C. L. *ECS Trans*. **2010**, *33*, 575-579.

(32) Cooper, W. C.; Zingaro, R. A. *Selenium*; Van Nostrand Reinhold, **1974**.

(33) Dai, P.; Xie, J.; Mayer, M. T.; Yang, X.; Zhan, J.; Wang, D. *Angew. Chem. Int. Ed*. **2013**, *52*, 11119-11123.

(34) Damjanovic, A.; Paunovic, M.; Bockris, J. O. *J. Electroanal. Chem*. **1965**, *9*, 93-111.

(35) Dasgupta, N. P.; Liu, C.; Andrews, S.; Prinz, F. B.; Yang, P. *J. Am. Chem. Soc*. **2013**, *135*, 12932-12935.

(36) Ding, Q.; Meng, F.; English, C. R.; Caban-Acevedo, M.; Shearer, M. J.; Liang, D.; Daniel, A. S.; Hamers, R. J.; Jin, S. *J. Am. Chem. Soc*. **2014**, *136*, 8504-8507.

(37) Ding, Q.; Zhai, J.; Cabán-Acevedo, M.; Shearer, M. J.; Li, L.; Chang, H.-C.; Tsai, M.-L.; Ma, D.; Zhang, X.; Hamers, R. *J. Adv. Mater*. **2015**, *27*, 6511-6518.

(38) Dresner, J.; Stringfellow, G. B. *J. Phys. Chem. Solids* **1968**, *29*, 303-311.

(39) Dunsch, L. *J. Solid State Electrochem*. **2011**, *15*, 1631-1646.

(40) El Abedin, S. Z.; Saad, A. Y.; Farag, H. K.; Borisenko, N.; Liu, Q. X.; Endres, F. *Electrochimica Acta* **2007**, *52*, 2746-2754.

(41) Endres, F. *Phys. Chem. Chem. Phys*. **2001**, *3*, 3165-3174.

(42) Endres, F.; MacFarlane, D.; Abbott, A. *Electrodeposition from ionic liquids*; John Wiley & Sons, **2008**.

(43) Fernicola, A.; Panero, S.; Scrosati, B.; Tamada, M.; Ohno, H. *ChemPhysChem* **2007**, *8*, 1103-1107.

(44) Fitchett, B. D.; Knepp, T. N.; Conboy, J. C. *J. Electrochem. Soc*. **2004**, *151*, 219.

(45) Galinski, M.; Lewandowski, A.; Stkepniak, I. *Electrochimica Acta* **2006**, *51*, 5567-5580.

(46) Ganta, D.; Sinha, S.; Haasch, R. T. *Surf. Sci. Spectra* **2014**, *21*, 19-27.

(47) Gilleo, M. A. *J. Chem. Phys*. **1951**, *19*, 1291.

(48) Gleason-Rohrer, D. C.; Brunschwig, B. S.; Lewis, N. S. *J. Phys. Chem. C* **2013**, *117*, 18031-18042.

(49) Goodey, A. P.; Eichfeld, S. M.; Lew, K.-K.; Redwing, J. M.; Mallouk, T. E. *J. Am. Chem. Soc*. **2007**, *129*, 12344-12345.

(50) Graham, A. K.; Pinkerton, H. L.; Boyd, H. J. *J. Electrochem. Soc*. **1959**, *106*, 651-654.

(51) Grim, S. O.; Matienzo, L. J. *Inorg. Chem*. **1975**, *14*, 1014-1018.

(52) Grimm, R. L.; Bierman, M. J.; O'Leary, L. E.; Strandwitz, N. C.; Brunschwig, B. S.; Lewis, N. S. *J. Phys. Chem. C* **2012**, *116*, 23569-23576.

(53) Hahn, B. P.; Stevenson, K. J. *J. Electroanal. Chem*. **2010**, *638*, 151-160.

(54) Hapiot, P.; Lagrost, C. *Chem. Rev*. **2008**, *108*, 2238-2264.

(55) He, T.; Ding, H.; Peor, N.; Lu, M.; Corley, D. A.; Chen, B.; Ofir, Y.; Gao, Y.; Yitzchaik, S.; Tour, J. M. *J. Am. Chem. Soc*. **2008**, *130*, 1699-1710.

(56) Heo, P.; Ichino, R.; Okido, M. *Electrochimica Acta* **2006**, *51*, 6325-6330.

(57) Hibble, S. J.; Wood, G. B. *J. Am. Chem. Soc*. **2004**, *126*, 959-965.

(58) Hiremath, R. K.; Rabinal, M. K.; Mulimani, B. G.; Khazi, I. M. *Langmuir* **2008**, *24*, 11300-11306.

(59) Hou, Y.; Abrams, B. L.; Vesborg, P. C. K.; Björketun, M. E.; Herbst, K.; Bech, L.; Setti, A. M.; Damsgaard, C. D.; Pedersen, T.; Hansen, O.; Rossmeisl, J.; Dahl, S.; Nørskov, J. K.; Chorkendorff, I. *Nat. Mater*. **2011**, *10*, 434-438.

(60) Hsiu, S.-I.; Sun, I.-W. *J. Appl. Electrochem*. **2004**, *34*, 1057-1063.

(61) Hu, C.-K.; Harper, J. M. E. *Mater. Chem. Phys*. **1998**, *52*, 5-16.

(62) Huddleston, J. G.; Visser, A. E.; Reichert, W. M.; Willauer, H. D.; Broker, G. A.; Rogers, R. D. *Green Chem*. **2001**, *3*, 156-164.

(63) Hunger, R.; Jaegermann, W.; Merson, A.; Shapira, Y.; Pettenkofer, C.; Rappich, J. *J. Phys. Chem. B* **2006**, *110*, 15432-15441.

(64) Ispas, A.; Adolphi, B.; Bund, A.; Endres, F. *Phys. Chem. Chem. Phys*. **2010**, *12*, 1793.

(65) Jafarian, M.; Mahjani, M. G.; Gobal, F.; Danaee, I. *J Appl Electrochem*. **2006**, *36*, 1169-1173.

(66) Jaramillo, T. F.; Jorgensen, K. P.; Bonde, J.; Nielsen, J. H.; Horch, S.; Chorkendorff, I. *Science* **2007**, *317*, 100-102.

(67) Jiqin, Z.; Jian, C.; Chengyue, L.; Weiyang, F. *J. Chem. & Eng. Data* **2007**, *52*, 812-816.

(68) Kaim, W.; Fiedler, *J. Chem. Soc. Rev*. **2009**, *38*, 3373-3382.

(69) Kasap, S.; Frey, J. B.; Belev, G.; Tousignant, O.; Mani, H.; Laperriere, L.; Reznik, A.; Rowlands, J. A. *Phys. Status solidi* **2009**, *246*, 1794-1805.

(70) Kawamura, Y. L.; Sakka, T.; Ogata, Y. H. *Electrochemistry* **2008**, *76*, 121-124.

(71) Kawamura, Y. L.; Sakka, T.; Ogata, Y. H. *J. Electrochem. Soc*. **2005**, *152*, C701-C705.

(72) Kim, H. J.; Kearney, K. L.; Le, L. H.; Pekarek, R. T.; Rose, M. J. *ACS Appl. Mater. & Interfaces* **2015**, *7*, 8572-8584.

(73) Komadina, J.; Akiyoshi, T.; Ishibashi, Y.; Fukunaka, Y.; Homma, T. *Electrochimica Acta* **2013**, *100*, 236-241.

(74) Kong, D.; Wang, H.; Cha, J. J.; Pasta, M.; Koski, K. J.; Yao, J.; Cui, Y. *Nano Lett*. **2013**, *13*, 1341-1347.

(75) Kye, J.; Shin, M.; Lim, B.; Jang, J.-W.; Oh, I.; Hwang, S. *ACS Nano* **2013**, *7*, 6017-6023.

(76) Lahiri, A.; Olschewski, M.; Ho?fft, O.; Zein El Abedin, S.; Endres, F. *J. Phys. Chem. C* **2013**, *117*, 1722-1727.

(77) Lai, Y.; Liu, F.; Li, J.; Zhang, Z.; Liu, Y. *J. Electroanal. Chem*. **2010**, *639*, 187-192.

(78) Laursen, A. B.; Pedersen, T.; Malacrida, P.; Seger, B.; Hansen, O.; Vesborg, P. C. K.; Chorkendorff, I. *Phys. Chem. Chem. Phys*. **2013**, *15*, 20000-20004.

(79) Lazell, M.; O'Brien, P.; Otway, D. J.; Park, J.-H. *J. Chem. Soc. Dalton Trans*. **2000**, 4479-4486.

(80) Lee, Y.-H.; Zhang, X.-Q.; Zhang, W.; Chang, M.-T.; Lin, C.-T.; Chang, K.-D.; Yu, Y.-C.; Wang, J. T.-W.; Chang, C.-S.; Li, L.-J.; Lin, T.-W. *Adv. Mater*. **2012**, *24*, 2320-2325.

(81) Leiga, A. G. *JOSA* **1968**, *58*, 1441-1445.

(82) Li, F.; Basile, V. M.; Pekarek, R. T.; Rose, M. J. *ACS Appl. Mater. & Interfaces* **2014**, *6*, 20557-20568.

(83) Li, G.; Tong, Y.; Liu, G. *J. Electroanal. Chem*. **2004**, *562*, 223-229.

(84) Liang, K. S.; Cramer, S. P.; Johnston, D. C.; Chang, C. H.; Jacobson, A. J.; Chianelli, R. R. *J. Non-Crystalline Solids* **1980**, *42*, 345-356.

(85) Lin, Z.-H.; Wang, C. C. *Mater. Chem. Phys*. **2005**, *92*, 591-594.

(86) Ling, Z. P.; Yang, R.; Chai, J. W.; Wang, S. J.; Leong, W. S.; Tong, Y.; Lei, D.; Zhou, Q.; Gong, X.; Chi, D. Z.; Ang, K.-W. *Opt. Express* **2015**, *23*, 13580.

(87) Liu, K.-K.; Zhang, W.; Lee, Y.-H.; Lin, Y.-C.; Chang, M.-T.; Su, C.-Y.; Chang, C.-S.; Li, H.; Shi, Y.; Zhang, H.; Lai, C.-S.; Li, L.-J. *Nano Lett*. **2012**, *12*, 1538-1544.

(88) Lucovsky, G.; Mooradian, A.; Taylor, W.; Wright, G. B.; Keezer, R. C. *Solid State Commun*. **1967**, *5*, 113-117.

(89) Maier, C. U.; Specht, M.; Bilger, G. *Int. J. Hydrog. Energy* **1996**, *21*, 859-864.

(90) Mane, R. S.; Lokhande, C. D. *Mater. Chem. Phys*. **2000**, *65*, 1-31.

(91) McFarlane, D. R.; Sun, J.; Golding, J.; Meakin, P.; Forsyth, M. *Electrochimica Acta* **2000**, *45*, 1271-1278.

(92) McKone, J. R.; Warren, E. L.; Bierman, M. J.; Boettcher, S. W.; Brunschwig, B. S.; Lewis, N. S.; Gray, H. B. *Energy & Environ. Sci*. **2011**, *4*, 3573-3583.

(93) Mehrotra, R. C.; Mathur, S. N. *J. Indian Chem. Soc.* **1964**, 41.

(94) Merki, D.; Fierro, S.; Vrubel, H.; Hu, X. *Chem. Sci*. **2011**, *2*, 1262-1267.

(95) Mikla, V. I.; Mikla, V. V. *Amorphous Chalcogenides: The Past, Present and Future*; Elsevier, **2011**; *Vol. 145*.

(96) Mooradian, A.; Wright, G. B.; Cooper, W. C. Pergamon Press. Oxf. **1969**.

(97) Muijsers, J. C.; Weber, T.; Vanhardeveld, R. M.; Zandbergen, H. W. _.; Niemantsverdriet, J. W. *J. Catal*. **1995**, *157*, 698-705.

(98) Müller, A.; Diemann, E.; Jostes, R.; Bögge, H. *Angew. Chem. Int. Ed. Engl*. **1981**, *20*, 934-955.

(99) Murugesan, S.; Akkineni, A.; Chou, B. P.; Glaz, M. S.; Vanden Bout, D. A.; Stevenson, K. J. *ACS Nano* **2013**, *7*, 8199-8205.

(100) Murugesan, S.; Kearns, P.; Stevenson, K. J. *Langmuir* **2012**, *28*, 5513-5517.

(101) Murugesan, S.; Quintero, O. A.; Chou, B. P.; Xiao, P.; Park, K.; Hall, J. W.; Jones, R. A.; Henkelman, G.; Goodenough, J. B.; Stevenson, K. J. *J. Mater. Chem*. **2014**, *2*, 2194-2201.

(102) Nagels, P.; Sleeckx, E.; Callaerts, R.; Tichy, L. *Solid State Commun*. **1995**, *94*, 49-52.

(103) Nakajima, H.; Nohira, T.; Hagiwara, R. *Electrochimica Acta* **2006**, *51*, 3776-3780.

(104) Nemanick, E. J.; Hurley, P. T.; Brunschwig, B. S.; Lewis, N. S. *J. Phys. Chem. B* **2006**, *110*, 14800-14808.

(105) Oh, I.; Kye, J.; Hwang, S. *Nano Lett*. **2011**, *12*, 298-302.

(106) Ohta, N.; Scheuermann, W.; Nakamoto, K. *Solid State Commun*. **1978**, *27*, 1325-1327.

(107) O'Neal, S.; Kolis, J. W. *J. Am. Chem. Soc*. **1988**, *110*, 1971-1973.

(108) Ong, S. P.; Andreussi, O.; Wu, Y.; Marzari, N.; Ceder, G. *Chem. Mater*. **2011**, *23*, 2979-2986.

(109) Poborchii, V. V.; Kolobov, A. V.; Tanaka, K. *Appl. Phys. Lett*. **1998**, 72.

(110) Ponomarev, E. A.; Albu-Yaron, A.; Tenne, R.; Lévy-Clément, C. *J. Electrochem. Soc*. **1997**, *144*, L277-L279.

(111) Ponomarev, E. A.; Neumann-Spallart, M.; Hodes, G.; Levy-Clement, C. *Thin Solid Films* **1996**, *280*, 86-89.

(112) Pratt III, H. D.; Rose, A. J.; Staiger, C. L.; Ingersoll, D.; Anderson, T. M. *Dalton Trans*. **2011**, *40*, 11396.

(113) Pulletikurthi, G.; Lahiri, A.; Carstens, T.; Borisenko, N.; Abedin, S. Z. E.; Endres, F. *J Solid State Electrochem*. **2013**, *17*, 2823-2832.

(114) Raevskaya, A. E.; Stroyuk, A. L.; Kuchmiy, S. Y.; Dzhagan, V. M.; Zahn, D. R.; Schulze, S. *Solid State Commun*. **2008**, *145*, 288-292.

(115) Rajalakshmi, M.; Arora, A. K. *Solid State Commun*. **1999**, *110*, 75-80.

(116) Redman, D. W.; Kim, H. J.; Stevenson, K. J.; Rose, M. J. *J. Mater. Chem*. **2016**, *4*, 7027-7035.

(117) Redman, D. W.; Murugesan, S.; Stevenson, K. J. *Langmuir* **2013**, *30*, 418-425.

(118) Saadi, F. H.; Carim, A. I.; Velazquez, J. M.; Baricuatro, J. H.; McCrory, C. C. L.; Soriaga, M. P.; Lewis, N. S. *ACS Catal*. **2014**, *4*, 2866-2873.

(119) Saji, V. S.; Lee, C.-W. *RSC Adv*. **2013**, *3*, 10058-10077.

(120) Santos, M. C.; Machado, S. A. *J. Electroanal. Chem*. **2004**, *567*, 203-210.

(121) Sarma, D. D.; Rao, C. N. R. *J. Electron Spectrosc. Relat. Phenom*. **1980**, *20*, 25-45.

(122) Schaltin, S.; Brooks, N. R.; Stappers, L.; Hecke, K. V.; Meervelt, L. V.; Binnemans, K.; Fransaer, J. *Phys. Chem. Chem. Phys*. **2012**, *14*, 1706-1715.

(123) Schwarzacher, W.; Lashmore, D. S. *IEEE Trans. Magn*. **1996**, *32*, 3133-3153.

(124) Seger, B.; Laursen, A. B.; Vesborg, P. C. K.; Pedersen, T.; Hansen, O.; Dahl, S.; Chorkendorff, I. *Angew. Chem*. **2012**, *51*, 9128-9131.

(125) Seger, B.; Pedersen, T.; Laursen, A. B.; Vesborg, P. C. K.; Hansen, O.; Chorkendorff, I. *J. Am. Chem. Soc*. **2013**, *135*, 1057-1064.

(126) Seo, J.; Kim, H. J.; Pekarek, R. T.; Rose, M. J. *J. Am. Chem. Soc*. **2015**, *137*, 3173-3176.

(127) Serrao, C. R.; Diamond, A. M.; Hsu, S.-L.; You, L.; Gadgil, S.; Clarkson, J.; Carraro, C.; Maboudian, R.; Hu, C.; Salahuddin, S. *Appl. Phys. Lett*. **2015**, *106*, 052101.

(128) Shenasa, M.; Sainkar, S.; Lichtman, D. *J. Electron Spectrosc. Relat. Phenom*. **1986**, *40*, 329-337.

(129) Siemeling, U.; Bretthauer, F.; Bruhn, C. *Z. für Anorg. und Allg. Chem*. **2006**, *632*, 1027-1032.

(130) Sniekers, J.; Brooks, N. R.; Schaltin, S.; Meervelt, L. V.; Fransaer, J.; Binnemans, K. *Dalton Trans*. **2014**, *43*, 1589-1598.

(131) Srinivasan, B. R.; Dhuri, S. N.; Poisot, M.; Näther, C.; Bensch, W. *Z. für Naturforsch. B* **2004**, *59*, 1083-1092.

(132) Steichen, M.; Dale, P. *Electrochem. Commun*. **2011**, *13*, 865-868.

(133) Tachikawa, N.; Katayama, Y.; Miura, T. *ECS Trans*. **2009**, *16*, 589-595.

(134) Tanaka, K.; Shimakawa, K. *Amorphous chalcogenide semiconductors and related materials*; Springer Science & Business Media, **2011**.

(135) Tang, H.; Dou, K.; Kaun, C.-C.; Kuang, Q.; Yang, S. *J. Mater. Chem*. **2014**, *2*, 360-364.

(136) Thomas, P. A.; Marvey, B. B. *Molecules* **2016**, *21*, 184.

(137) Tokuda, H.; Hayamizu, K.; Ishii, K.; Susan, M. A. B. H.; Watanabe, M. *J. Phys. Chem. B* **2004**, *108*, 16593-16600.

(138) Tonndorf, P.; Schmidt, R.; Böttger, P.; Zhang, X.; Börner, J.; Liebig, A.; Albrecht, M.; Kloc, C.; Gordan, O.; Zahn, D. R. *Opt. Express* **2013**, *21*, 4908-4916.

(139) Tran, P. D.; Pramana, S. S.; Kale, V. S.; Nguyen, M.; Chiam, S. Y.; Batabyal, S. K.; Wong, L. H.; Barber, J.; Loo, *J. Chem. Eur. J*. **2012**, *18*, 13994-13999.

(140) Tsai, C.; Chan, K.; Abild-Pedersen, F.; Nørskov, J. K. *Phys. Chem. Chem. Phys*. **2014**, *16*, 13156.

(141) Von Hippel, A.; Bloom, M. C. *J. Chem. Phys*. **1950**, *18*, 1243-1251.

(142) Vrubel, H.; Hu, X. *ACS Catal*. **2013**, *3*, 2002-2011.

(143) Wang, H.; Zhang, Q.; Yao, H.; Liang, Z.; Lee, H.-W.; Hsu, P.-C.; Zheng, G.; Cui, Y. *Nano Lett*. **2014**, *14*, 7138-7144.

(144) Wang, Q. H.; Kalantar-Zadeh, K.; Kis, A.; Coleman, J. N.; Strano, M. S. *Nat. Nanotech* **2012**, *7*, 699-712.

(145) Wang, Y.; Rogers, E. I.; Compton, R. G. *J. Electroanal. Chem*. **2010**, *648*, 15-19.

(146) Warren, E. L.; McKone, J. R.; Atwater, H. A.; Gray, H. B.; Lewis, N. S. *Energy & Environ. Sci*. **2012**, *5*, 9653-9661.

(147) Webb, L. J.; Lewis, N. S. *J. Phys. Chem. B* **2003**, *107*, 5404-5412.

(148) Weber, T.; Muijsers, J. C.; Niemantsverdriet, J. W. *J. Phys. Chem*. **1995**, *99*, 9194-9200.

(149) Weber, T.; Muijsers, J. C.; Van Wolput, J. H. M. C.; Verhagen, C. P. J.; Niemantsverdriet, J. W. *J. Phys. Chem*. **1996**, *100*, 14144-14150.

(150) Wilkes, J. S.; Zaworotko, M. J. *J. Chem. Soc. Chem. Commun*. **1992**, 965.

(151) Wolff, T. E.; Berg, J. M.; Hodgson, K. O.; Frankel, R. B.; Holm, R. H. *J. Am. Chem. Soc*. **1979**, *101*, 4140-4150.

(152) Wu, M.; Vanhoutte, G.; Brooks, N. R.; Binnemans, K.; Fransaer, J. *Phys. Chem. Chem. Phys*. **2015**, *17*, 12080-12089.

(153) Yoshihara, S.; Endo, K.; Sato, E.; Bockris, J. O. '. M. *J. Electroanal. Chem*. **1994**, *372*, 91-94.

(154) Zhang, L.; Liu, C.; Wong, A.; Resasco, J.; Yang, P. *Nano Res*. **2015**, *8*, 281-287.

(155) Zhang, S.; Sun, N.; He, X.; Lu, X.; Zhang, X. *J. Phys. Chem. Ref. Data* **2006**, *35*, 1475.

(156) Zhang, X.; Meng, F.; Mao, S.; Ding, Q.; Shearer, M. J.; Faber, M. S.; Chen, J.; Hamers, R. J.; Jin, S. *Energy & Environ. Sci*. **2015**, *8*, 862-868.

(157) Zhu, Y.-L.; Katayama, Y.; Miura, T. *Electrochimica Acta* **2010**, *55*, 9019-9023.